



Durham E-Theses

Astrophysical Fluxes as Windows into the Nature of Neutrinos

FRANKLIN, JACK,DENNIS

How to cite:

FRANKLIN, JACK,DENNIS (2025) *Astrophysical Fluxes as Windows into the Nature of Neutrinos*, Durham theses, Durham University. Available at Durham E-Theses Online:
<http://etheses.dur.ac.uk/16084/>

Use policy

The full-text may be used and/or reproduced, and given to third parties in any format or medium, without prior permission or charge, for personal research or study, educational, or not-for-profit purposes provided that:

- a full bibliographic reference is made to the original source
- a [link](#) is made to the metadata record in Durham E-Theses
- the full-text is not changed in any way

The full-text must not be sold in any format or medium without the formal permission of the copyright holders.

Please consult the [full Durham E-Theses policy](#) for further details.

Astrophysical Fluxes as Windows into the Nature of Neutrinos

Looking For Answers From Up Above

Jack Dennis Franklin

A Thesis presented for the degree of
Doctor of Philosophy



Institute for Particle Physics Phenomenology
Department of Physics
Durham University
United Kingdom

May 2025

Astrophysical Fluxes as Windows into the Nature of Neutrinos

Looking For Answers From Up Above

Jack Dennis Franklin

Submitted for the degree of Doctor of Philosophy

May 2025

Abstract: Neutrinos permeate the Universe, possessing energies from the meV scale all the way up to EeVs, and potentially beyond. The abundance and variety of these neutrino fluxes makes them excellent candidates for experimentally probing the fundamental nature and behaviour of neutrinos.

In this thesis, we will assess how neutrinos produced in two very different astrophysical environments can be used for this purpose.

We will begin by looking at how the pseudo-Dirac scenario for neutrino masses would impact the observations of Solar neutrinos at the future JUNO experiment. It will be shown that these effects can be sizeable, and used to constrain the parameter space of this scenario.

Our focus will then shift to point sources of neutrinos at the IceCube experiment. We will model the effects of interactions between these high energy neutrinos, and the relic neutrinos left over from the early Universe. Using public experimental data, we will then place constraints on both the density of relic neutrinos, and the parameters of a new, scalar mediated, interaction between neutrinos.

Contents

Abstract	iii
List of Figures	ix
List of Tables	xv
Declaration	xvii
Acknowledgements	xix
Epigraph	xxi
Dedication	xxiii
Preface	xxv
1 Neutrinos in the Standard Model	1
1.1 Fermions	2
1.1.1 Neutral Fermions	4
1.1.2 Fermions With Global Symmetries	4
1.1.3 Fermions with Local Symmetries	8
1.2 Gauge Bosons	9

1.3	The Standard Model Lagrangian	10
1.4	Electroweak Spontaneous Symmetry Breaking	13
1.5	Lepton Interactions	16
2	Massive Neutrinos	19
2.1	Dirac neutrinos	20
2.2	Mixed Majorana and Dirac Mass Terms with One Generation	22
2.2.1	See-Saw limit	23
2.2.2	Pseudo-Dirac limit	24
2.3	Majorana Neutrinos	25
2.3.1	Majorana vs Dirac Neutrinos	26
2.4	Oscillations	27
2.4.1	Wave Packets and Decoherence	31
2.5	Neutrino Oscillations in Matter	32
2.6	Solar Neutrinos	34
2.6.1	Low Energy Regime	39
2.6.2	Three Generation Solar Neutrinos	40
3	Probing the pseudo-Dirac scenario using Solar neutrinos at JUNO	45
3.1	Solar Neutrinos at JUNO	46
3.2	The Three Generation Pseudo-Dirac Scenario	49
3.3	Pseudo-Dirac Neutrino Oscillations	53
3.3.1	MSW Regime	55
3.3.2	Quasi-Vacuum Oscillations	56
3.3.3	Vacuum Oscillation Regime	57

3.3.4	Higher Energy ${}^7\text{Be}$ Neutrinos	57
3.4	Analysis	61
3.5	Constraints on the Possible Pseudo-Dirac Nature of Neutrinos from JUNO	64
4	Constraining Neutrino Self-Interactions with Point-Source Fluxes at IceCube	69
4.1	Cosmic Neutrino Background	71
4.1.1	Neutrino Degrees of Freedom	72
4.2	Propagation of Neutrino Fluxes	74
4.3	Numerically Solving The Neutrino Transport Equation	75
4.3.1	Upper And Lower Bounds On Neutrino Energy	75
4.3.2	Solving The Transport Equation Without Redshift	77
4.3.3	Solving The Transport Equation With Redshift	80
4.4	Analysis Methodology	82
4.4.1	Future Sensitivities	84
4.5	Relic Overdensity	84
4.5.1	Total cross-sections	88
4.5.2	Differential cross-sections	90
4.5.3	Results	91
4.6	Scalar mediated neutrino self-interactions	94
4.6.1	Results	96
4.7	Conclusion	101
5	Summary	103

List of Figures

1.1	The charged, left-handed 2-spinor field f , and its partners under conjugation f^\dagger , charge conjugation, $\mathcal{C}f = \hat{f}$, and parity flipping, $\mathcal{P}f = \bar{f}$	7
3.1	The neutrino mass spectrum in the three-generation pseudo-Dirac scenario. We choose, as a matter of convention, to have the standard mass squared differences, Δm_{ij}^2 , to be between the smaller of the mass pairs. These mass pairs are almost degenerate, expect for a small mass squared difference δm_{ij}^2	53
3.2	Numerical results for solar electron neutrino survival probability, P_{ee} , for the SM scenario (black solid curve) and for the 1-4 pseudo-Dirac pair scenario with maximal mixing ($\theta_{14} = \pi/4$). The coloured curves correspond to different possible values of the mass-squared splitting between the pseudo-Dirac pairs, as indicated in the legend. The light blue shaded region corresponds to the energies of pp neutrinos coming from the Sun, and the vertical red dashed line is the monochromatic energy of the high energy ${}^7\text{Be}$ neutrino line. The vertical black dashed line is the minimum neutrino energy given a cut in the recoil energy of 200 keV.	59

-
- 3.3 Expected event rates at JUNO for pp (orange) and Be^7 (green) solar neutrinos assuming a 6-year exposure time with 20 kilotonne fiducial mass. Here we show how a maximal mixing 1-4 pseudo-Dirac pair affects the event rate that JUNO will measure, for δm_{14}^2 values of $1 \times 10^{-7} \text{ eV}^2$ (dashed), $5 \times 10^{-12} \text{ eV}^2$ (dotted), $1 \times 10^{-12} \text{ eV}^2$ (dash-dotted), and the SM case (solid). The data is shown with bin widths of 25 keV, as was used in our analysis, to demonstrate how JUNO can put limits on these values. 63
- 3.4 The 2σ sensitivity on the parameter space of 1-4 pseudo-Dirac pair oscillations at JUNO (red). These are shown for three values of the recoil energy cut: 200 keV (solid line), 250 keV (dotted line), and 450 keV (dashed line). Also shown are the projected limits that can be set by DARWIN [36] (purple), as well as the current limits (collected in Ref. [42]) from Gadolinium (Gd) [43], Super-Kamiokande [44] (SK), SNO [45] and Cl [46], [47] experiments. 65
- 3.5 Marginalised χ^2 as a function of the mass splitting δm_{ij}^2 for various pseudo-Dirac scenarios at JUNO with maximal mixing $\theta_{ij} = \pi/4$. We consider here the 1-4 pair scenario (green), the 2-5 pair scenario (orange), and the full pseudo-Dirac (PD) scenario (purple) with three mass pairs, each with the same mass squared splitting. The sensitivity for each scenario is also displayed for the three recoil cuts of 200 keV (solid lines), 250 keV (dotted lines), and 450 keV (dashed lines) . . . 66
- 4.1 The t-statistic $-2\Delta \log \mathcal{L}$ for NGC 1068 as a function of the relic neutrino overabundance. The effect of the value of m_1 is also demonstrated by taking different limits for the mass scale, as explained in the text. Here we take $d_{\text{eff}} = 14 \text{ Mpc}$ for the radius of the overdense region. 85

- 4.2 Normalised muon neutrino fluxes from NGC 1068 at IceCube under different scenarios. The black line is the initial flux, taken to be a power law. The spectral index of the initial flux is the best-fit values from our TS analysis, $\gamma = 3.15$. Given this initial flux, the other lines are the solutions to the transport equation, with the relevant neutrino number density ratios indicated. The number density is assumed to be constant over the distance between NGC 1068 and Earth, and m_1 (the lightest neutrino mass) is 0.034 eV . Flux given in arbitrary units as the normalisation is a priori unknown. 86
- 4.3 Feynman diagrams for the relevant interactions between neutrinos and relic neutrinos. (a) and (b) are the t - and u -channel diagrams, respectively, for elastic scattering of incident neutrinos off of relic neutrinos. (c) is for lepton pair production where $l = \nu$ or $l = e^-$. (d) is the t -channel e^+e^- pair production diagram. (e) is the t -channel elastic scattering of neutrinos on relic antineutrinos. 87
- 4.4 The combined 90% confidence limits from all three sources on a global relic overabundance as a function of the mass of the lightest neutrino. The solid line is the constraint using current data, and the dashed(dotted) line shows the expectation of the limit with an extra 10(80) years of data taking. We assume normal ordering and take the mass splittings from NuFIT 2022 [41]. 92

-
- 4.5 Effects of NSI on the neutrino flux propagating through the CνB. We take an initial power-law flux with spectral index $\gamma = 3.86$, which matches that of PKS. The final flux at Earth is calculated for a source at the same distance as NGC 1068 - 14 Mpc - and for a source at the same redshift as TXS 0506+056 - $z = 0.45$. This highlights the difference in final flux caused by both the increased propagation distance and the redshift from the expansion of the Universe. The value of the coupling between tau-flavoured neutrinos and the scalar particle, $g_{\tau\tau}$, as well as the mass of the scalar particle, M_ϕ , are varied between figures (a)-(d) to demonstrate their effect on the final fluxes. Flux values are given in arbitrary units as the normalisation of the flux is a priori unknown. 97
- 4.6 Ratio of the final to initial muon neutrino fluxes from three toy sources at redshifts $z_0 \in \{0.5, 0.3, 0.1\}$. The lowering of the flux energy, thereby preserving the bump in flux at lower energies, can be clearly seen. To produce these fluxes an initial power-law flux was used with spectral index $\gamma = 2.7$. The scalar coupling was chosen to be $g_{\tau\tau} = 0.02$ and the scalar mediator mass was $m_\phi = 0.5$ MeV. Finally, the lightest neutrino mass m_1 was given a value such that the cosmological bound on the sum of the neutrino masses was saturated. 98
- 4.7 Pdfs of logarithms of the true neutrino energy E_{true} (left panels), and the reconstructed muon energy E_{reco} (right panels), for varying values of the coupling $g_{\tau\tau}$. For each set of NSI parameters, the full analysis was performed assuming the source was TXS 0506+056, and the best fit initial power law parameters were used. The pdfs were constructed from event samples created using SkyLLH. 99

4.8 **Scalar mediated neutrino self-interaction.** The 2σ exclusion region determined by IceCube is shown based on astrophysical sources NGC 1068, TXS 0506+056 and PKS 1424+240, and their combined result (black solid line). To produce these, we assumed normal ordering of the neutrino masses and took $\sum_i m_i = 0.1\text{eV}$ with mass splittings from [41]. Additionally, we include the projected exclusion region for an additional 80 years of operation (black dash line), equivalent to 10 years of data collection with IceCube-Gen2. We compare our results to those from [59], which includes exclusion regions from BBN (grey), Z to invisibles decay (purple), and IceCube HESE (green).100

List of Tables

1.1	Hyper-charges and representations of the SM fields under the gauge groups $U(1)_Y$, $SU(2)_L$, and $SU(3)_c$	11
3.1	Parameters for the differential fluxes of solar neutrino sources used in this work, from [27]	47
4.1	The best-fit values of the signal event normalisation (n_s) and the spectral index (γ) for each of the three sources included in the analysis, assuming SM interactions and no overdensity in the relic neutrino flux.	83

Declaration

The work in this thesis is based on research carried out in the Department of Physics at Durham University. No part of this thesis has been submitted elsewhere for any degree or qualification.

The following chapters have been published in the form of papers:

- Chapter 3 is based on:
J. Franklin, Y. F. Perez-Gonzalez and J. Turner,
JUNO as a probe of the pseudo-Dirac nature using solar neutrinos,
Phys. Rev. D **108** (2023) no.3, 035010
- Chapter 4 is based on:
J. Franklin, I. Martínez Soler, Y. F. Perez-Gonzalez and J. Turner,
Constraints on the Cosmic Neutrino Background from NGC 1068,
arXiv:2404.02202.

Copyright © 2025 Jack Dennis Franklin.

The copyright of this thesis rests with the author. No quotation from it should be published without the author's prior written consent and information derived from it should be acknowledged.

Acknowledgements

First, I would like to thank Jessica Turner for her supervision during my PhD. I would also like to mention the other members of the neutrino group who I have worked with, Yuber and Ivan, for their contributions and insights.

My PhD has been made by all of the friends I have made over the past few years. Firstly I would like to shout out all of the members of Cafe 215, as well as our honorary member Tommy, who's camaraderie got me through so much. I would also like to thank my current office mate Tom, particularly for putting up with my constant questions over the last few months. The D&D crew - Mia, Helen, Rollo, James, and Ansh - have brought me so much joy over the last few years. Tommy and Guillaume, thank you for the laughs and late night trash telly. I would also like to thank Ery, Ansh, and Joanne for their feedback on this thesis.

Thank you to my family for their continued love and support throughout my whole life. I would not be who I am today without you all.

Finally, Serena, who I could not have got to this point without. I love you so much.

What we observe is not nature itself, but nature exposed to our method of questioning.

— from *Physics and Philosophy: The Revolution in Modern Science* by Werner Heisenberg

Dedicated to

Grandad Nunn

and

Grandad Roy

Preface

Neutrinos are notoriously elusive. They interact so weakly with other particles that they are able to travel over cosmic distances, even through the Earth, without trouble. However, these unique properties also make neutrinos extremely interesting probes of the Universe. Astrophysical fluxes of neutrinos, produced in some of the most extreme conditions in the Universe, provide us with a new window into the processes from which they originate. For example Solar neutrinos, produced in the core of the Sun in thermonuclear processes, are able to propagate from their production point all the way to Earth. This is in contrast to the photons produced by the same category of processes, which interact strongly with the plasma in the Sun. Neutrinos are thus a unique probe of the interior of the Sun.

As much as neutrinos are useful for understanding astrophysics, the inverse is also true. Astrophysical neutrino fluxes have properties which would be impossible to recreate on Earth. Of particular importance to this thesis are the range of energies which they can possess, as well as the large distances they travel before being detected. This allows for scrutiny of the exact nature and behaviour of neutrinos themselves. In fact, it was the study of Solar neutrinos which eventually led to the discovery of neutrino oscillations and thus neutrino masses.

In this thesis we will discuss how two astrophysical fluxes of neutrinos can provide us with insights into the fundamental nature and behaviour of neutrinos. In Chapter 1 we will cover the Standard Model of particle physics, in particular those aspects most relevant to the study of neutrinos. We will then introduce the possible ways that neutrinos may be given masses in Chapter 2. In Chapter 3 we will investigate

how Solar neutrinos can be used to investigate the pseudo-Dirac neutrino scenario, focussing on the JUNO experiment in particular. Chapter 4 will instead look at high energy neutrinos at the IceCube experiment, originating from point sources, and determine the constraints on two scenarios - overabundance of relic neutrinos, and scalar mediated non-standard interactions between neutrinos. The thesis will then be summarised in Chapter 5, and future progress in this field discussed.

Chapter 1

Neutrinos in the Standard Model

The Standard Model (SM) of particle physics consists of fundamental particles and their transformations under chosen symmetries; in particular how they transform under the Lorentz group $SO^+(1, 3)$, which is the symmetry group of special relativity, and the gauge group $SU(2)_L \times U(1)_Y \times SU(3)_c$. The SM is an example of a *quantum field theory* (QFT), and as such all of the information that defines the theory is encoded in a Lagrangian density function \mathcal{L} (from this point on, we will just use the term "Lagrangian" to refer to a Lagrangian density function). The action of the QFT is

$$S[\{\phi_i\}] \equiv \int dx^4 \mathcal{L}(\{\phi_i\}), \quad (1.0.1)$$

where by the set $\{\phi_i\}$ we refer to the field content of the theory. Throughout this chapter, we will demand that our Lagrangian is hermitian ($\mathcal{L}^\dagger = \mathcal{L}$), as well as invariant under transformations of the symmetries of the theory. Unless otherwise stated, we will also demand the Lagrangian be renormalisable.

Since the focus of this thesis will be on neutrinos, we will begin by building a picture of spin-half particles (fermions) in the Lagrangian formulation. We will then discuss local/gauge symmetries, before finally defining the SM. The implications of the SM in relation to neutrinos, particularly of their interactions, will also be discussed.

1.1 Fermions

Fermions are constructed from anti-commuting *Weyl spinors*. These are fields which transform in either the $(1/2, 0)$ (left-handed) or $(0, 1/2)$ (right-handed) representations of the group $SL(2, \mathbb{C})$, which is the double copy of the Lorentz symmetry group $SO^+(1, 3)$. These two representations are interchanged by hermitian conjugation. As a matter of convention, we will introduce spinor fields as left-handed by default and refer to their right-handed counterparts via hermitian conjugation.

We will write left-handed spinors with lowered greek letter indices, e.g. ψ_α . A spinor that transforms in the dual of this representation will instead have raised indices ψ^α . The indices are raised or lowered by the two-index antisymmetric epsilon symbols, $\epsilon^{\alpha\beta}$ and $\epsilon_{\alpha\beta}$ respectively, [1], whose non-zero elements are

$$\epsilon^{12} = -\epsilon^{21} = \epsilon_{21} = -\epsilon_{12} = 1.$$

For right-handed spinors we instead use dotted indices, to distinguish the representations. We define

$$\psi_{\dot{\alpha}}^\dagger \equiv (\psi_\alpha)^\dagger, \quad \psi^{\dagger\dot{\alpha}} \equiv (\psi^\alpha)^\dagger \quad (1.1.1)$$

and

$$\epsilon^{\dot{\alpha}\dot{\beta}} \equiv (\epsilon^{\alpha\beta})^*, \quad \epsilon_{\dot{\alpha}\dot{\beta}} \equiv (\epsilon_{\alpha\beta})^*. \quad (1.1.2)$$

Under a general Lorentz transformation, a left-handed spinor field transforms as [1]:

$$\psi_\alpha \rightarrow M_\alpha^\beta \psi_\beta, \quad (1.1.3)$$

$$\psi^\alpha \rightarrow [(M^{-1})^T]^\alpha_\beta \psi^\beta, \quad (1.1.4)$$

where $M \in SL(2, \mathbb{C})$ is a Lorentz transformation in the left-handed representation.

We can write this matrix as

$$M = \exp \left[-\frac{1}{2} i \theta_{\mu\nu} J^{\mu\nu} \right], \quad (1.1.5)$$

where $\theta_{\mu\nu}$ are real numbers and $J^{\mu\nu}$ are the generators of the Lorentz algebra in this representation.

The transformations of the right-handed counterpart, $f_{\dot{\alpha}}^{\dagger} \equiv (f_{\alpha})^{\dagger}$, can be found from the hermitian conjugate of the transformations of f_{α} :

$$f_{\dot{\alpha}}^{\dagger} \rightarrow (M^*)_{\dot{\alpha}}^{\dot{\beta}} f_{\dot{\beta}}^{\dagger}, \quad (1.1.6)$$

$$f^{\dagger\dot{\alpha}} \rightarrow [(M^{-1})^{\dagger}]^{\dot{\alpha}}_{\dot{\beta}} f^{\dagger\dot{\beta}}. \quad (1.1.7)$$

From these transformation properties, we can see that Lorentz scalars can be constructed by contracting spinors with the same handedness. We will write these using the shorthand notation

$$\psi\chi \equiv \psi^{\alpha}\chi_{\alpha} \quad \text{and} \quad \psi^{\dagger}\chi^{\dagger} \equiv \psi^{\dagger}_{\dot{\alpha}}\chi^{\dagger\dot{\alpha}}.$$

To construct additional Lorentz scalar terms for our Lagrangian, we need to be able to combine spinors into Lorentz tensors. Lorentz vectors can be built by introducing the *sigma matrices*, σ^{μ} and $\bar{\sigma}^{\mu}$, which are given by [1], [2]:

$$\begin{aligned} (\sigma^0)_{\alpha\dot{\beta}} &= \begin{pmatrix} 1 & 0 \\ 0 & 1 \end{pmatrix} = (\bar{\sigma}^0)^{\dot{\alpha}\beta}, & (\sigma^1)_{\alpha\dot{\beta}} &= \begin{pmatrix} 0 & 1 \\ 1 & 0 \end{pmatrix} = -(\bar{\sigma}^1)^{\dot{\alpha}\beta}, \\ (\sigma^2)_{\alpha\dot{\beta}} &= \begin{pmatrix} 0 & -i \\ i & 0 \end{pmatrix} = -(\bar{\sigma}^2)^{\dot{\alpha}\beta}, & (\sigma^3)_{\alpha\dot{\beta}} &= \begin{pmatrix} 1 & 0 \\ 0 & -1 \end{pmatrix} = -(\bar{\sigma}^3)^{\dot{\alpha}\beta}. \end{aligned}$$

We can now construct the Lorentz vectors by combining spinors with undotted and dotted indices, i.e. of opposite handedness. To produce Lorentz scalars, we can contract them with other Lorentz vectors. The simplest choice of Lorentz vector is the partial derivative ∂_{μ} . Contracting this results in derivative terms that make the spinors dynamical.

Before we begin to construct a Lagrangian for the fermions, we need to specify the symmetries of the fermions beyond Lorentz invariance. The simplest case, which we will begin with, is fermions without any additional symmetries.

1.1.1 Neutral Fermions

We refer to fermions that only transform under the representations of the Lorentz group as being neutral¹. In the simple case of a theory with a single neutral fermion, the complete Lagrangian is [1][3]²

$$\mathcal{L} = i\psi^\dagger \bar{\sigma}^\mu \partial_\mu \psi - \frac{m}{2}(\psi\psi + \psi^\dagger\psi^\dagger). \quad (1.1.8)$$

From this Lagrangian, the equations of motion (eom) of ψ and ψ^\dagger are

$$i\bar{\sigma}^\mu \partial_\mu \psi - \frac{m}{2}\psi^\dagger = 0, \quad (1.1.9)$$

$$i\bar{\sigma}^\mu \partial_\mu \psi^\dagger - \frac{m}{2}\psi = 0. \quad (1.1.10)$$

Fermions that obey this set of coupled differential equations are called *Majorana fermions*. We will refer to a Lagrangian of the form Eq. (1.1.8) as a Majorana Lagrangian.

From Eq. (1.1.8) and Eq. (1.1.9), we can see that the terms which contract spinors of the same handedness result in the fermion being massive. In general, we will call these *mass terms*. We will specifically refer to mass terms of neutral fermions as Majorana mass terms, or just Majorana masses.

1.1.2 Fermions With Global Symmetries

If we impose additional global symmetries onto our fermions, the Majorana mass terms previously introduced will not be invariant under those symmetries. If we take the simplest case of an additional U(1) symmetry, we define the action of an element of this group to transform the left-handed spinor as

$$\psi_\alpha \rightarrow e^{-i\theta} \psi_\alpha, \quad (1.1.11)$$

¹Sometimes, when there are other symmetries in the theory, we will refer to neutral fermions as *singlets*.

²The integral of this Lagrangian density is hermitian only if the integral of the total derivative term $\partial_\mu (f^\dagger \bar{\sigma}^\mu \psi)$ vanishes, with appropriate boundary conditions[3].

where $\theta \in \mathbb{R}$.

The transformation of the right-handed spinor can then be found from hermitian conjugation to be

$$\psi_{\dot{\alpha}}^{\dagger} \rightarrow e^{+i\theta} \psi_{\dot{\alpha}}^{\dagger}. \quad (1.1.12)$$

The mass terms will thus transform as

$$\psi\psi \rightarrow e^{-2i\theta} \psi\psi \quad \text{and} \quad \psi^{\dagger}\psi^{\dagger} \rightarrow e^{+2i\theta} \psi^{\dagger}\psi^{\dagger}. \quad (1.1.13)$$

Since our Lagrangian must be invariant under the symmetries of the theory, we are left with just the derivative term

$$\mathcal{L} = i\psi^{\dagger}\bar{\sigma}^{\mu}\partial_{\mu}\psi, . \quad (1.1.14)$$

The eom from this Lagrangian are the Weyl equations

$$i\bar{\sigma}^{\mu}\partial_{\mu}\psi = 0, \quad (1.1.15)$$

$$i\bar{\sigma}^{\mu}\partial_{\mu}\psi^{\dagger} = 0, \quad (1.1.16)$$

which define the dynamics of charged, massless fermions. We will refer to these types of fermions as *Weyl fermions*, and the Lagrangian Eq. (1.1.14) as the Weyl Lagrangian.

A single spinor field can thus only have charge or mass, but not both at the same time. However we see in nature that charged particles, such as the electron, are massive. To reconcile this, we have to introduce an additional spinor field. This field, which we will call $\hat{\psi}$, transforms under the global symmetry in the opposite way to ψ

$$\hat{\psi} \rightarrow e^{+i\theta} \hat{\psi}. \quad (1.1.17)$$

With the addition of this new field, and its hermitian conjugate, it is now possible to construct terms which are invariant under the global transformations. The Lagrangian of this new theory is given by

$$\mathcal{L} = i\psi^{\dagger}\bar{\sigma}^{\mu}\partial_{\mu}\psi + i\hat{\psi}^{\dagger}\bar{\sigma}^{\mu}\partial_{\mu}\hat{\psi} - m\psi\hat{\psi} - m\psi^{\dagger}\hat{\psi}^{\dagger}. \quad (1.1.18)$$

The hermitian conjugate of $\hat{\psi}$ is right-handed, but transforms under the global transformations in the same way as ψ . We make this point clearer by defining $\bar{\psi} \equiv \hat{\psi}^\dagger$. The relationships between the different spinor fields are shown in Fig. 1.1.

Using this notation, we write the *Dirac Lagrangian*

$$\mathcal{L} = i\psi^\dagger \bar{\sigma}^\mu \partial_\mu \psi + i\bar{\psi} \bar{\sigma}^\mu \partial_\mu \hat{\psi} - m\psi\hat{\psi} - m\psi^\dagger\bar{\psi}, \quad (1.1.19)$$

from which the eom are found to be

$$i\bar{\sigma}^\mu \partial_\mu \psi - m\bar{\psi} = 0, \quad (1.1.20)$$

$$i\bar{\sigma}^\mu \partial_\mu \bar{\psi} - m\psi = 0, \quad (1.1.21)$$

$$i\bar{\sigma}^\mu \partial_\mu \hat{\psi} - m\psi^\dagger = 0, \quad (1.1.22)$$

$$i\bar{\sigma}^\mu \partial_\mu \psi^\dagger - m\hat{\psi} = 0. \quad (1.1.23)$$

These eom couple left- and right-handed spinors with the same charge. We can write them more compactly by introducing a bi-spinor, also known as a Dirac spinor,

$$\Psi_\alpha^{\dot{\alpha}} \equiv \begin{pmatrix} \psi_\alpha \\ \bar{\psi}^{\dot{\alpha}} \end{pmatrix}. \quad (1.1.24)$$

We can rewrite the eom in this notation to find the *Dirac equation*,

$$(-i\gamma^\mu \partial_\mu + m)\Psi = 0, \quad (1.1.25)$$

where we define the Dirac gamma matrices as

$$\gamma^\mu \equiv \begin{pmatrix} 0 & \sigma^\mu \\ \bar{\sigma}^\mu & 0 \end{pmatrix}. \quad (1.1.26)$$

Note that the upper right submatrix is σ^μ , rather than $\bar{\sigma}^\mu$, due to the order of the spinors changing compared to Eq. (1.1.19).

We can also rewrite the Dirac Lagrangian in this form

$$\mathcal{L} = \bar{\Psi}(i\gamma^\mu \partial_\mu - m)\Psi, \quad (1.1.27)$$

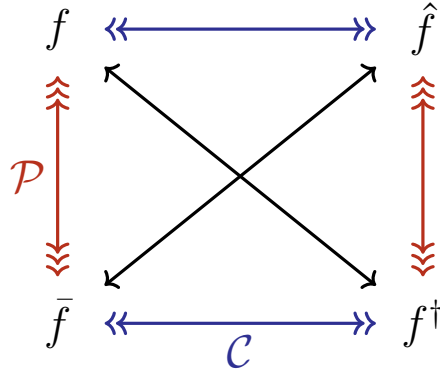


Figure 1.1: The charged, left-handed 2-spinor field f , and its partners under conjugation f^\dagger , charge conjugation, $\mathcal{C}f = \hat{f}$, and parity flipping, $\mathcal{P}f = \bar{f}$.

where the Dirac conjugate $\bar{\Psi}$ is given by $\Psi^\dagger \Delta$, and

$$\Delta \equiv \begin{pmatrix} 0 & \delta^{\dot{\alpha}}_{\dot{\beta}} \\ \delta_{\alpha}^{\beta} & 0 \end{pmatrix}. \quad (1.1.28)$$

The fact that we have to contract Ψ with the Dirac conjugate field $\bar{\Psi}$ ³, rather than just the Hermitian conjugate Ψ^\dagger , is due to the non-unitarity of the Dirac representation of the group of Lorentz transformations. Explicitly, $\Psi^\dagger = (f^\dagger \ \hat{f})$, whereas in Eq. (1.1.27) we have on the left $(\hat{f} \ f^\dagger) = \Psi^\dagger \Delta$.

We can also express the Majorana Lagrangian, Eq. (1.1.8), in the same formalism with the identification $f \equiv \hat{f} \iff f^\dagger \equiv \bar{f}$. This is also true for the Weyl Lagrangian, which is just the massless limit of Eq. (1.1.27). However writing it this way obfuscates the fact that in the massless limit the fields f and \bar{f} are completely independent from each other. In fact, there is no need for both fields to exist in a theory simultaneously, which is not true for the massive case.

³It is common to see the Dirac conjugate written as $\bar{\Psi} = \Psi^\dagger \gamma^0$. In terms of their numerical values, γ^0 and Δ are the same, however they have very different spinor index structure [1]

1.1.3 Fermions with Local Symmetries

A transformation is local if its action depends on spacetime. To achieve this for a U(1) symmetry, we promote the parameter $\theta \rightarrow \theta(x)$, where x is a point in spacetime. A fermion that is charged under this group will transform as

$$\psi \rightarrow e^{-i\theta(x)} \psi. \quad (1.1.29)$$

If a local transformation leaves the Lagrangian invariant it is a local symmetry, or a gauge symmetry, of the theory.

The mass terms $\psi\hat{\psi}$ are invariant under these transformations by construction, so it is sufficient to look at the Weyl Lagrangian only. With a fermion transforming under a U(1) gauge the Weyl Lagrangian transforms as:

$$\begin{aligned} \mathcal{L}_{\text{Weyl}} &= \psi^\dagger \bar{\sigma}^\mu \partial_\mu \psi \rightarrow e^{i\theta(x)} \psi^\dagger \bar{\sigma}^\mu \partial_\mu (e^{-i\theta(x)} \psi) \\ &= e^{i\theta(x)} \psi^\dagger \bar{\sigma}^\mu e^{-i\theta(x)} (-i(\partial_\mu \theta(x))\psi + \partial_\mu \psi) \\ &= \psi^\dagger \bar{\sigma}^\mu \partial_\mu \psi - i\psi^\dagger \bar{\sigma}^\mu (\partial_\mu \theta(x)) \psi, \end{aligned} \quad (1.1.30)$$

which is clearly not gauge invariant. To resolve this, we need to add an additional field to the Lagrangian, which transforms in the adjoint representation of the gauge symmetry in the following way:

$$A_\mu \rightarrow U(x) \left(A_\mu - \frac{1}{g} \partial_\mu \right) U^\dagger(x), \quad (1.1.31)$$

where $U(x)$ is the gauge transformation and g is the *coupling constant* of the group, which governs the overall strength of the local transformations. As indicated by the indices, this field also transforms as a Lorentz vector. If we promote the partial derivative in our Lagrangian to a *covariant derivative*, i.e.

$$\partial_\mu \rightarrow D_\mu \equiv \partial_\mu - igA_\mu, \quad (1.1.32)$$

then the Lagrangian will be gauge invariant, as the extra terms with derivatives of $\theta(x)$ will cancel out. The field A_μ is referred to as a *gauge boson*. Though we have only looked at the case of a $U(1)$ gauge symmetry, the exact same argument holds for any other local Lie group action, the difference being in the definition of A_μ . Since the transformations will be of the form $U(x) = \exp(-i\theta^a(x)T_a)$, where T_a are the generators of the Lie group, we define the gauge boson as $A_\mu = A_\mu^a T_a$. This field is clearly in the Lie algebra of the symmetry group, hence why it transforms in the adjoint representation under gauge transformations.

If we expand our gauge invariant Weyl Lagrangian, we find we also have a term which couples the spinor fields with the gauge boson fields:

$$\psi^\dagger \bar{\sigma}^\mu D_\mu \psi = \psi^\dagger \bar{\sigma}^\mu \partial_\mu \psi - ig \psi^\dagger \bar{\sigma}^\mu A_\mu \psi. \quad (1.1.33)$$

This term leads to interactions between fermions and gauge fields, which in turn allows fermions to interact with each other via an intermediate gauge boson.

1.2 Gauge Bosons

From a gauge field $A_\mu = A_\mu^a T_a$, it is possible to construct a Lorentz tensor which transforms in the adjoint representation of the symmetry, thus allowing for quadratic terms to define the dynamics of the field. This tensor is the *field strength* of the gauge field. In component form it is given by

$$F_{\mu\nu}^a \equiv \partial_\mu A_\nu^a - \partial_\nu A_\mu^a + gf^{abc} A_\mu^b A_\nu^c, \quad (1.2.1)$$

where the *structure coefficients* f^{abc} are defined by the commutation relations of the Lie group $[T^a, T^b] = if^{abc}T^c$. The component form is equivalently written as

$$F_{\mu\nu} \equiv \partial_\mu A_\nu - \partial_\nu A_\mu - ig[A_\mu, A_\nu] \quad (1.2.2)$$

$$\equiv F_{\mu\nu}^a T_a \quad (1.2.3)$$

By including this term in the Lagrangian:

$$\mathcal{L}_G = F_{\mu\nu}^a F_a^{\mu\nu} = \frac{1}{2} \text{tr} [F_{\mu\nu} F^{\mu\nu}] , \quad (1.2.4)$$

we find quadratic derivative terms of the gauge fields. This results in the gauge field becoming dynamical, with the components satisfying the Klein-Gordon equation [3]:

$$(\partial^2 + m^2) A_\mu = 0 \quad (1.2.5)$$

with $m^2 \equiv 0$ since there are no quadratic terms in Eq. (1.2.4). If we were to try and add massive terms to the Lagrangian, they would be proportional to $A_\mu A^\mu$, which would not be gauge invariant. The gauge bosons, which appear from demanding gauge invariance of the Lagrangian, must then be massless.

1.3 The Standard Model Lagrangian

The SM is made up of various fields which transform in representations of the previously mentioned symmetries. The Lorentz symmetries categorise the fields into scalar (spin 0) and vector (spin 1) bosons, and spin 1/2 fermions. The vector bosons arise from the local gauge symmetries, as described in Section 1.1.3, and transform in their adjoint representations. Fermions are the matter constituents of the SM, and transform in the fundamental representations of the gauge groups. Finally, the SM contains one scalar boson field, referred to as the Higgs field. This field couples to the chiral $SU(2)_L$ gauge field, and plays an important role in the generation of

Field	U(1) _Y	SU(2) _L	SU(3) _c
L_i	-1	2	1
\hat{e}_i	+2	1	1
Q_i	+1/3	2	3
\hat{u}_i	-4/3	1	3
\hat{d}_i	+2/3	1	3
H	+1	2	1

Table 1.1: Hyper-charges and representations of the SM fields under the gauge groups U(1)_Y, SU(2)_L, and SU(3)_c.

particle masses which is shown in Section 1.4. The representations of the fermions and the Higgs field are shown in Table 1.1.

All of this information is written in terms of a Lagrangian density formulation, which can be roughly separated into pieces pertaining to the pure gauge/Yang-Mills (\mathcal{L}_G) sector, the kinematic terms of the fermions (\mathcal{L}_K), the Yukawa interactions of the Higgs (\mathcal{L}_Y), and the Higgs Lagrangian (\mathcal{L}_H).

Fermions appear in the SM Lagrangian in two places, the first of which is the "kinetic" Lagrangian

$$\begin{aligned} \mathcal{L}_K = & L_i^\dagger \bar{\sigma}^\mu D_\mu L_i + \bar{e}_i \bar{\sigma}^\mu D_\mu \hat{e}_i \\ & + Q_i^\dagger \bar{\sigma}^\mu D_\mu Q_i + \bar{u}_i \bar{\sigma}^\mu D_\mu \hat{u}_i + \bar{d}_i \bar{\sigma}^\mu D_\mu \hat{d}_i, \end{aligned} \quad (1.3.1)$$

where the fields correspond to those in Table 1.1. The action of the covariant derivative on a field depends on the groups under which the field transforms. For example, for Q_i ,

$$D_\mu Q_i = \left(\partial_\mu - ig_1 \frac{Q_Y}{2} B_\mu - ig_2 W_\mu - ig_3 G_\mu \right) Q_i, \quad (1.3.2)$$

where B_μ , W_μ , and G_μ are the gauge boson fields of the U(1)_Y, SU(2)_L, and SU(3)_c groups, respectively. The couplings g_1 , g_2 , g_3 are assigned in the same manner.

The field strengths of the gauge bosons are denoted using the same letter as the field, but with two Lorentz indices, and have the following pure gauge/Yang-Mills Lagrangian:

$$\mathcal{L}_G = -\frac{1}{2} \text{tr} [G_{\mu\nu} G^{\mu\nu}] - \frac{1}{2} \text{tr} [W_{\mu\nu} W^{\mu\nu}] - \frac{1}{2} B_{\mu\nu} B^{\mu\nu}. \quad (1.3.3)$$

The Higgs field transforms under both $U(1)_Y$ and $SU(2)_L$ transformations. Its Lagrangian is given by:

$$\mathcal{L}_H = (D_\mu H)^\dagger (D^\mu H) + V(H), \quad (1.3.4)$$

where

$$D_\mu H = (\partial_\mu - i\frac{g_1}{2} B_\mu - ig_2 W_\mu) H,$$

and $V(H)$ is the potential of the Higgs field, which will be expanded in Section 1.4. In addition to this Lagrangian, it is also possible to create terms with fermions and the Higgs - these are Yukawa interactions and have the following form:

$$\mathcal{L}_Y = \sum_{i,j} [\lambda_{ij}^{(l)} L_i^\dagger H \bar{e}_j + \lambda_{ij}^{(u)} Q_i^\dagger \hat{H} \bar{u}_j + \lambda_{ij}^{(d)} Q_i^\dagger H \bar{d}_j] + h.c., \quad (1.3.5)$$

where the sum is over the three different families of fermion species. The coupling strengths of the interactions are given by $\lambda_{ij}^{(f)}$, which are in general complex numbers. The conjugate of the Higgs field is $\hat{H} = i\tau_2 H^*$, which transforms as a $SU(2)_L$ doublet but with opposite hypercharge. The matrices $\tau_i = \sigma_i/2$ the generators of $SU(2)_L$, such that their commutator is given by $[\tau_i, \tau_j] = i\epsilon_{ijk} \tau_k$. We refrain from using the sigma matrices in this context to make clear that the τ matrices are acting on the $SU(2)_L$ doublet representation, rather than on the spinors.

1.4 Electroweak Spontaneous Symmetry Breaking

All of the SM fermions are massless Weyl fermions, however we know from experimental observation that all electrically charged fermions (we will talk about neutrinos in the next section) have mass [4]. The SM resolves this via a process known as *Spontaneous Symmetry Breaking* (SSB).

The potential in the Higgs Lagrangian Eq. (1.3.4) is chosen to have the form

$$V(H) = -\mu^2 H^\dagger H + \frac{\lambda}{2} (H^\dagger H)^2, \quad (1.4.1)$$

where $\lambda > 0$. If we have $\mu^2 > 0$, this potential has a minimum when $H^\dagger H = \mu^2/2\lambda$. In order to reduce the potential energy of the Higgs field, the vacuum must be a particular value of H which satisfies this constraint, thus giving the field a vacuum expectation value (vev) $\langle H \rangle = \mu/\sqrt{2\lambda}$. We will choose to write the vacuum state of the Higgs field, H_0 , in the unitary gauge, such that

$$H_0 = \frac{1}{\sqrt{2}} \begin{pmatrix} 0 \\ v \end{pmatrix}. \quad (1.4.2)$$

If we then look at what happens to the interaction terms between the Higgs field and the leptonic fields:

$$\lambda_{ij} L_i^\dagger H_0 \bar{e}_j = \frac{\lambda_{ij}}{\sqrt{2}} \begin{pmatrix} \nu_i^\dagger & e_i^\dagger \end{pmatrix} \begin{pmatrix} 0 \\ v \end{pmatrix} \bar{e}_j = \frac{\lambda_{ij} v}{\sqrt{2}} e_i^\dagger \bar{e}_j \quad (1.4.3)$$

we find that they have exactly the form we expect of a mass term, where in this case $m = \lambda_{ij} v/\sqrt{2}$. However, we also see that unless $\lambda_{ij} \equiv \delta_{ij}$, which a priori we have no reason to assume, the flavour states are not mass eigenstates. This fact results in flavour mixing, which will be discussed in more detail in Chapter 2. The Higgs

vev also gives mass to the up and down type quarks. However, it does not give the neutrinos mass because there is no term in the Lagrangian which couples the neutrino to the Higgs vev. More concretely, there is no $SU(2)_L$ singlet with which to form mass terms. We will explore possible scenarios for generating neutrino masses in Chapter 2.

We know that the Higgs field transforms under the $U(1)_Y$ and $SU(2)_L$ gauge symmetries. If we look at the vacuum state we can see that it is no longer invariant under the group action of the symmetries of the Higgs field. Specifically, the generators of $SU(2)_L$ act on H_0 in the following way:

$$\tau_1 H_0 = \frac{1}{2\sqrt{2}} \begin{pmatrix} v \\ 0 \end{pmatrix}, \quad \tau_2 H_0 = \frac{1}{2\sqrt{2}} \begin{pmatrix} -iv \\ 0 \end{pmatrix}, \quad \tau_3 H_0 = \frac{1}{2\sqrt{2}} \begin{pmatrix} 0 \\ -v \end{pmatrix}.$$

Furthermore, the vacuum is also not invariant under $U(1)_Y$ transformations. The only generators that leave the Higgs vacuum unchanged are thus the identity matrix, and τ_3 up to constant factors. If we look at the combination $(I + \tau_3)/2$, the resulting matrix has only upper left components, and so will leave the vacuum Higgs field unchanged. We are then left with a Lie algebra with only one generator, which is isomorphic to $u(1)$. Hence the original gauge symmetry of the SM is broken from $SU(2)_L \times U(1)_Y$ to $U(1)_{em}$ [3][5][6]. This breaking occurs in the vacuum i.e. it is not a dynamical process, hence why it is referred to as *spontaneous* symmetry breaking. Returning to the kinetic terms of the Higgs Lagrangian, if we substitute in the vacuum field of the Higgs:

$$\begin{aligned} (D_\mu H_0)^\dagger (D^\mu H_0) &= |(\partial_\mu - ig_1 B_\mu - ig_2 W_\mu) H_0|^2 \\ &= \frac{v^2}{8} \left[g_2^2 |W_\mu^1|^2 + g_2^2 |W_\mu^2|^2 + |g_1 B_\mu - g_2 W_\mu^3|^2 \right] \end{aligned} \tag{1.4.4}$$

where $|\cdot|^2$ implies hermitian conjugation and Lorentz contraction. In the above form, it is clear that after SSB we have new vector fields which are formed from mixtures of the old gauge bosons. If we relabel them in the following way[6]:

$$W_\mu^\mp = \frac{W_\mu^1 \pm iW_\mu^2}{\sqrt{2}} \quad \text{and} \quad Z_\mu = \cos\theta_W W_\mu^3 - \sin\theta_W B_\mu, \quad (1.4.5)$$

where

$$\cos\theta_W = \frac{g_2}{\sqrt{g_1^2 + g_2^2}} \quad \text{and} \quad \sin\theta_W = \frac{g_1}{\sqrt{g_1^2 + g_2^2}}, \quad (1.4.6)$$

then Eq. (1.4.4) can be rewritten such that:

$$(D_\mu H_0)^\dagger (D^\mu H_0) = m_W^2 W_\mu^+ W^{-\mu} + \frac{m_Z^2}{2} Z_\mu Z^\mu, \quad (1.4.7)$$

where we have defined the masses

$$m_W^2 = \frac{g_2^2 v^2}{4} \quad \text{and} \quad m_Z^2 = \frac{(g_1^2 + g_2^2) v^2}{4}. \quad (1.4.8)$$

This tells us that we now have three massive vector bosons in our theory. There is one other possible combination of gauge bosons which is missing from Eq. (1.4.7), which is $A_\mu = \cos\theta_W W_\mu^3 + \sin\theta_W B_\mu$. Its exclusion from the mass generation above implies it is massless. In fact, as previously stated, we have a remnant gauge symmetry $U(1)_{\text{em}}$, and this massless boson is exactly the gauge boson of that symmetry. If we now rewrite the covariant derivative for the left-handed leptons L_i in terms of the new field definitions:

$$\begin{aligned} D_\mu L_i = & \left[\partial_\mu - i \frac{g_2}{\sqrt{2}} (W_\mu^+ \tau^+ + W_\mu^- \tau^-) - i \frac{1}{\sqrt{g_1^2 + g_2^2}} Z_\mu \left(g_2 \tau_3 - g_1 \frac{Q_Y}{2} \right) \right. \\ & \left. - i \frac{g_1 g_2}{\sqrt{g_1^2 + g_2^2}} A_\mu \left(\tau_3 + \frac{Q_Y}{2} \right) \right] L_i \end{aligned} \quad (1.4.9)$$

If we identify the new $U(1)_{\text{em}}$ charge and gauge coupling as

$$Q_{\text{em}} = \tau_3 + \frac{Q_Y}{2} \quad \text{and} \quad e = \frac{g_1 g_2}{\sqrt{g_1^2 + g_2^2}}, \quad (1.4.10)$$

respectively, then the interaction terms become:

$$-i \frac{g_2}{\sqrt{2}} (W_\mu^+ \tau^+ + W_\mu^- \tau^-) - i \frac{g_2}{\cos \theta_W} Z_\mu (\tau_3 - \sin^2 \theta_W Q_{\text{em}}) - ie A_\mu Q_{\text{em}}. \quad (1.4.11)$$

1.5 Lepton Interactions

If we apply the EM charge operator to the left-handed weak doublet, we find that:

$$Q_{\text{em}} L_i = \begin{pmatrix} 0 & 0 \\ 0 & -1 \end{pmatrix} L_i \quad (1.5.1)$$

from which we identify the upper component, which is neutral, with a neutrino, and the lower component, which has charge -1 , with the electron. By expanding the kinetic terms in Eq. (1.3.1) in terms of the components, we find non-gauged interaction terms. We denote interactions involving the W^\pm fields as Charged Current (CC) interactions, as the W bosons carry EM charge, and those involving the Z field as Neutral Current (NC) interactions. The interaction terms are as follows:

$$\mathcal{L}_{\text{CC}} = \frac{ie}{\sqrt{2} \sin \theta_W} (W_\mu^+ \nu_l^\dagger \bar{\sigma}^\mu e_l + W_\mu^- e_l^\dagger \bar{\sigma}^\mu \nu_l) \quad (1.5.2)$$

$$\mathcal{L}_{\text{NC}} = \frac{ieZ^\mu}{\cos \theta_W \sin \theta_W} \left(\frac{1}{2} \nu_l^\dagger \bar{\sigma}^\mu \nu_l - \frac{1}{2} e_l^\dagger \bar{\sigma}^\mu e_l + \sin^2 \theta_W (e_l^\dagger \bar{\sigma}^\mu e_l + \bar{e}_l \bar{\sigma}^\mu \hat{e}_l) \right) \quad (1.5.3)$$

where the subscript l denotes the flavour eigenstates of the CC interactions. From these Lagrangians, and those governing the kinematics of the fields, we can derive the usual Feynman rules and calculate scattering amplitudes.

For interactions with energies much less than the mass of the W and Z bosons, it is possible to integrate out these fields (see, for example, [3] Chapters 29 and 88). This reduces the fields from being dynamic to static, which is valid in the regime where their energies are much lower than their masses. The effective Lagrangian that results from this process is given by [3]:

$$\mathcal{L}_{\text{eff}} = 2\sqrt{2}G_F \left(J_+^\mu J_{-\mu} + J_Z^\mu J_{Z\mu} \right), \quad (1.5.4)$$

where we have defined for brevity the currents:

$$J_+^\mu \equiv e_l^\dagger \bar{\sigma}^\mu \nu_l \quad (1.5.5)$$

$$J_-^\mu \equiv \nu_l^\dagger \bar{\sigma}^\mu e_l \quad (1.5.6)$$

$$J_Z^\mu \equiv J_3^\mu + \sin^2 \theta_W J_{\text{em}}^\mu \quad (1.5.7)$$

$$J_3^\mu \equiv \frac{1}{2} \left(\nu_l^\dagger \bar{\sigma}^\mu \nu_l - e_l^\dagger \bar{\sigma}^\mu e_l \right) \quad (1.5.8)$$

$$J_{\text{em}}^\mu \equiv \sin^2 \theta_W \left(e_l^\dagger \bar{\sigma}^\mu e_l + \bar{e}_l \bar{\sigma}^\mu \hat{e}_l \right). \quad (1.5.9)$$

The coupling constant of the effective interaction is the *Fermi constant*, G_F , and is defined as:

$$G_F \equiv \frac{e^2}{4\sqrt{2} \sin^2 \theta_W M_W^2}. \quad (1.5.10)$$

The effective interaction Lagrangian is an example of an *effective field theory* (EFT). It is non-renormalisable, as can be deduced from the fact that the Fermi constant has mass dimension $[G_F] = -2$. We can use this Lagrangian to evaluate the tree level Feynman diagrams of low energy interactions which are of interest to us.

Chapter 2

Massive Neutrinos

In the SM treatment, neutrinos are massless particles. We may be tempted to couple the neutrinos to the Higgs field as we did with the other fermions. However this requires the introduction of a new particle which does not transform under $SU(2)_L$, for each flavour of neutrino that we wish to give mass. The Lagrangian term for this coupling is identical to that of the up quarks:

$$\mathcal{L}_y^\nu = \sum_{i,j} \lambda_{ij}^\nu L_i^\dagger \hat{H} \bar{\nu}_j + \text{h.c.} \quad (2.0.1)$$

the new fields are $\hat{\nu}_i$, and its hermitian conjugate $\bar{\nu}_i$. These new fields are singlets under the gauge symmetries of the SM, as they do not transform under $SU(2)_L$ and have $Q_Y = 0$, so they do not interact with the gauge fields. This means that we can also add a Majorana mass term for $\bar{\nu}$ in our Lagrangian. The relevant terms are now[7]:

$$\mathcal{L}_{\text{mass}}^\nu = - \sum_{i,j} \lambda_{ij}^\nu L_i^\dagger \hat{H} \bar{\nu}_j - \frac{1}{2} \sum_i m_{ij} \bar{\nu}_i \bar{\nu}_j + \text{h.c.} , \quad (2.0.2)$$

after EWSSB, Eq. (2.0.2) becomes:

$$\mathcal{L}_{\text{mass}}^\nu = - \sum_{i,j} \frac{\lambda_{ij}^\nu v}{\sqrt{2}} \nu_i^\dagger \bar{\nu}_j - \frac{1}{2} \sum_i m_{ij} \bar{\nu}_i \bar{\nu}_j + \text{h.c.} \quad (2.0.3)$$

we can identify from the first term of this equation a mass matrix in flavour space $(M_D)_{ij} = (\lambda_{ij}^\nu v) / \sqrt{2}$. Looking at the structure of the Lagrangian in Eq. (2.0.3), we find both Dirac mass terms $(\nu_i^\dagger \bar{\nu}_i)$ and Majorana terms $(\bar{\nu}_i \bar{\nu}_j)$. If we use the fact that $\nu_i^\dagger \bar{\nu}_j = \bar{\nu}_j \nu_i^\dagger$ we can write Eq. (2.0.3) in a clearer form:

$$\mathcal{L}_{\text{mass}}^\nu = -\frac{1}{2} \begin{pmatrix} \boldsymbol{\nu}^\dagger & \bar{\boldsymbol{\nu}} \end{pmatrix} \begin{pmatrix} \mathbf{0} & \mathbf{M}_D \\ (\mathbf{M}_D)^T & \mathbf{m} \end{pmatrix} \begin{pmatrix} \boldsymbol{\nu}^\dagger \\ \bar{\boldsymbol{\nu}} \end{pmatrix} + \text{h.c.}, \quad (2.0.4)$$

where the fields into vectors such that $(\boldsymbol{\nu}^\dagger)_i = \nu_i^\dagger$, and similarly for $\bar{\boldsymbol{\nu}}$. We can use the fact that $\bar{\nu}_i \bar{\nu}_j = \bar{\nu}_j \bar{\nu}_i$ to constrain \mathbf{m} to be a symmetric complex matrix. As a matrix equation, the fact that the Lagrangian contains mixed Dirac and Majorana mass terms is clearer. In order to find the physical states of the fields, i.e. the mass eigenstates, we need to diagonalise the matrix in the above equation. In order to do so, and to understand the implications of the mixed mass terms, we will take certain limits of the scale of the different mass matrices.

2.1 Dirac neutrinos

In the limit of $|\mathbf{m}| = 0$, the neutrino mass terms are identical to those of Dirac neutrinos (see Eq. (1.1.19)). The full neutrino Lagrangian is then:

$$\begin{aligned} \mathcal{L}^\nu &= \nu_i^\dagger \bar{\sigma}^\mu \partial_\mu \nu_i + \bar{\nu}_i \bar{\sigma}^\mu \partial_\mu \hat{\nu}_i - M_i \nu_i^\dagger \bar{\nu}_i - M_i \nu_i \hat{\nu}_i \\ &+ \frac{ie}{\sqrt{2} \sin \theta_W} \left(W_\mu^+ \nu_l^\dagger \bar{\sigma}^\mu e_l + W_\mu^- e_l^\dagger \bar{\sigma}^\mu \nu_l \right) + \frac{ie}{2 \cos \theta_W \sin \theta_W} Z_\mu \nu_l^\dagger \bar{\sigma}^\mu \nu_l, \end{aligned} \quad (2.1.1)$$

where e_l are the charged leptons, and sums over indices (and flavour states) are implicit. We differentiate between the neutrino mass eigenstates and interaction (flavour) eigenstates by their indices, which are i for the former and l for the latter.

The masses M_i are taken to be the real, positive square roots of the eigenvalues of $M_D^\dagger M_D$. We find these by diagonalising the mass matrix using a bi-unitary transformation.

For a general $N \times N$ complex matrix \tilde{M} , we can construct two hermitian positive semi-definite matrices by multiplying it with its hermitian conjugate from the left and right:

$$(\tilde{M}\tilde{M}^\dagger)^\dagger = \tilde{M}\tilde{M}^\dagger \quad \text{and} \quad (\tilde{M}^\dagger\tilde{M})^\dagger = \tilde{M}^\dagger\tilde{M}. \quad (2.1.2)$$

These matrices will thus have real and positive eigenvalues. With unitary matrices U and V defined by the following:

$$U^\dagger\tilde{M}\tilde{M}^\dagger U = M^2 \quad \text{and} \quad V^\dagger\tilde{M}^\dagger\tilde{M}V = M^2 \quad (2.1.3)$$

from which we can see that

$$M = U^\dagger\tilde{M}V \quad \text{or equivalently} \quad \tilde{M} = U M V^\dagger, \quad (2.1.4)$$

where $M_{ij} = M_i\delta_{ij}$. We can then rewrite the Dirac mass term in the following way (focussing on the right handed spinors in order to match convention):

$$\tilde{M}_{l'l}\nu_l^\dagger\bar{\nu}_{l'} = U_{li}M_{ij}(V^\dagger)_{j'l'}\nu_l^\dagger\bar{\nu}_{l'} = M_{ij}\nu_i^\dagger\bar{\nu}_j. \quad (2.1.5)$$

Since the $\bar{\nu}$ fields do not participate in weak interactions, we are free to redefine them such that $V_{li}\bar{\nu}_i \rightarrow \bar{\nu}_i$, thus removing V from the theory. We can also identify from the above that $\nu_l = (U)_{li}\nu_i$ and after applying the same procedure to the charged leptons, the charged current interaction term becomes:

$$W_\mu^- e_l^\dagger \bar{\sigma}^\mu \nu_l = \left(U_e^\dagger \right)_{il} (U_\nu)_{lj} W_\mu^- e_i^\dagger \bar{\sigma}^\mu \nu_j, \quad (2.1.6)$$

where we have differentiated between the mixing matrices for neutrinos and charged leptons, U_ν and U_e respectively. We identify the mass eigenstates of the charged leptons with those observed experimentally, i.e. $\{e_i \mid i \in \{1, 2, 3\}\} \equiv \{e, \mu, \tau\}$. From the above, we can identify the mixing matrix between neutrino and charged lepton mass states - the Pontecorvo-Maki-Nakagawa-Sakata (PMNS) matrix:

$$U_{\text{PMNS}} = U_e^\dagger U_\nu. \quad (2.1.7)$$

It is customary to construct flavour eigenstates for the neutrinos using U_{PMNS} . Often, the charged lepton mass states are indexed by Greek letters, e.g. $\alpha \in \{e, \mu, \tau\}$, thus:

$$\nu_\alpha = (U_{\text{PMNS}})_{\alpha i} \nu_i. \quad (2.1.8)$$

Since the neutral current (Z -exchange) interactions term contains both ν^\dagger and ν , the choice of field definition is not important as the matrices are all unitary, and so no mass state mixing occurs.

2.2 Mixed Majorana and Dirac Mass Terms with One Generation

In order to build a qualitative picture of the effect of mixed mass terms, it is useful to simplify the problem further. If we have only one species of fermion, the flavour vectors - ν^\dagger , $\bar{\nu}$, and so on - return to being two-component spinors, and the mass matrices - \mathbf{m} and \mathbf{M}_D - become real and complex numbers respectively. Investigating this scenario allows for analytical expressions which highlight the qualitative

properties of the physics with different mass limits.

The mass term in this case becomes:

$$\mathcal{L}_{\text{mass}}^\nu = -\frac{1}{2} \begin{pmatrix} \nu^\dagger & \bar{\nu} \end{pmatrix} \begin{pmatrix} 0 & M_D \\ M_D & m \end{pmatrix} \begin{pmatrix} \nu^\dagger \\ \bar{\nu} \end{pmatrix} + \text{h.c.} . \quad (2.2.1)$$

Since the mass matrix is complex symmetric, Takagi diagonalisation can be used to produce real and positive diagonal elements [8][1]. This results in the following:

$$\mathbf{M} = \begin{pmatrix} 0 & M_D \\ M_D & m \end{pmatrix} = \mathbf{U} \begin{pmatrix} m_1 & 0 \\ 0 & m_2 \end{pmatrix} \mathbf{U}^T , \quad (2.2.2)$$

where U is a unitary matrix and $m_1, m_2 > 0$.

There are two interesting limits of the values of m which produce drastically different physics. These are the See-Saw and Pseudo-Dirac limits, the latter of which will be discussed in further detail in Chapter 3.

2.2.1 See-Saw limit

The first simplifying limit we will look at is the case where $m \gg |M_D|$. If we rewrite $M_D = e^{i\theta} \epsilon m$, with real parameters θ and ϵ , then for small ϵ we have the following:

$$m_1 = m\epsilon^2 + O(\epsilon^3) \quad \text{and} \quad m_2 = m(1 + \epsilon^2) + O(\epsilon^3) . \quad (2.2.3)$$

Truncating these to linear order in the mass ratio ϵ , we find that

$$m_1 = \frac{|M_D|^2}{m} \quad \text{and} \quad m_2 = m . \quad (2.2.4)$$

This limit thus results in two mass states, one heavy and one light. This See-Saw

scenario is often seen as a possible explanation for the extremely small neutrino masses observed experimentally [9], [10].

2.2.2 Pseudo-Dirac limit

It is also interesting to look at the inverse limit, where $|M_D| \gg m$. This is the pseudo-Dirac scenario [10]–[15]. In this case, the values of the masses are [9]

$$m_{1,2} = |M_D| \mp \frac{m}{2} = |M_D| \left(1 \mp \frac{1}{2} \frac{m}{|M_D|} \right). \quad (2.2.5)$$

To linear order in $\varepsilon \equiv m/|M_D|$, the unitary diagonalisation matrix is found to have the form

$$U = \begin{pmatrix} \cos \theta & \sin \theta \\ -\sin \theta & \cos \theta \end{pmatrix} \begin{pmatrix} e^{i\phi} & 0 \\ 0 & 1 \end{pmatrix}, \quad (2.2.6)$$

where ϕ is a real phase and the mixing angle θ is given by

$$\tan \theta = \frac{1 - 4\varepsilon}{1 + 4\varepsilon}. \quad (2.2.7)$$

Clearly, as $\varepsilon \rightarrow 0$, the mixing of the neutrinos become maximal ($\theta = \pi/4$).

Since the difference in the masses between pseudo-Dirac pairs are so small, it can be extremely difficult to distinguish experimentally between true Dirac and pseudo-Dirac scenarios. In Chapter 3, we will investigate a possible experimental analysis for probing this scenario.

2.3 Majorana Neutrinos

There is an alternative possibility where active neutrinos can have mass, but no Yukawa coupling. If we view the low energy regime of the SM, after EWSSB, as a theory in its own right, we can view the neutrino as a Majorana particle since it is neutral under both of the remaining gauge symmetries. From this perspective, we could expect the neutrino to have a Majorana mass term,

$$\mathcal{L} \supset -\frac{M_L}{2} \nu_i \nu_i + \text{h.c.} . \quad (2.3.1)$$

However, there is no way to introduce this term in the SM Lagrangian before EWSSB without breaking either gauge invariance or renormalisability. The SM has been tested to an excellent degree of precision in experiments, and so we can be confident that is a good theory to explain the phenomenology available at, for example, collider experiments. On the other hand, all particle physics experiments have some upper limit on the energy scale at which they can probe the theory. As such, the SM is often viewed as an EFT which emerges from some higher scale theory. This is the same idea as with the low energy SM theory that arises after EWSSB. This means we can add non-renormalisable terms to our Lagrangian, so long as they obey the gauge invariance of the SM. This is identical to the four-Fermi interaction theory outlined in Section 1.5, which was proposed to explain leptonic interactions before the SM as we know it was identified.

Returning to the neutrino mass, we introduce the following non-renormalisable term to our Lagrangian[16]

$$\mathcal{L}_5 = -\frac{\mathcal{C}_5^{ij}}{\Lambda} \left(\epsilon^{ab} H_a L_{ib} \right) \left(\epsilon^{cd} H_c L_{jd} \right) + \text{h.c.} , \quad (2.3.2)$$

where we have reintroduced the $SU(2)_L$ indices a, b, c, d to form an inner product between the Higgs and leptonic fields using ϵ^{ab} . Λ is the scale of the new physics where the SM is no longer a valid EFT, and \mathcal{C}_5^{ij} are the *Wilson coefficients* for these

terms. The subscript refers to the fact that the combination of H and L_i has mass dimension five. The scale Λ reduces the mass scale of the whole term to four which we expect for our Lagrangian density.

After EWSSB, this term reduces to

$$\mathcal{L}_5 = -\frac{\mathcal{C}_5 v^2}{\Lambda} \nu_i \nu_i + \text{h.c.}, \quad (2.3.3)$$

where we have neglected terms containing the Higgs boson as we are interested only on the neutrino mass term. Since the Higgs vev $v/\sqrt{2}$ is $\mathcal{O}(100 \text{ GeV})$, and $\Lambda \gg \mathcal{O}(1 \text{ TeV})$ to ensure the SM is a good EFT at collider experiments, we can expect the Majorana mass

$$M_L = \frac{\mathcal{C}_5 v^2}{2\Lambda}, \quad (2.3.4)$$

to be very small, which aligns with experimental observations. This EFT treatment allows us to remain agnostic of the true UV theory of the Universe and instead parametrise the observable effect at lower energies.

In the previous sections which focussed on mixed Dirac-Majorana mass terms, we could have also included this effective Majorana mass to be more general. However, the qualitative outcomes of the different limits remain the same when M_L is chosen appropriately and so we will not revisit these scenarios.

2.3.1 Majorana vs Dirac Neutrinos

It is important to compare between neutrinos which gain mass through Yukawa couplings (Dirac neutrinos) and those which gain their mass from the dimension five operator (Majorana neutrinos). In particular, we may be interested in how the nature of neutrinos could be elucidated in experiments. If we perform diagonalisation of the Majorana neutrino masses we can find the mixing matrix which maps between

the interaction and mass bases. The mixing matrix in the Majorana scenario differs from the Dirac one only by a diagonal matrix containing arbitrary phases[17]:

$$U_{\text{Majorana}} = U_{\text{Dirac}} \text{diag}(1, e^{i\phi_1}, e^{i\phi_2}). \quad (2.3.5)$$

In general, these phases are difficult to measure. Oscillation experiments are not sensitive to these phases, as the observables depend only on the magnitude of the mixing matrix elements. As such, we will safely ignore them in the next section.

Perhaps the most evident difference between these two scenarios is their respective degrees of freedom. Recall that in the Dirac scenario it was necessary to introduce a new field $\hat{\nu}$, in order to form Dirac mass terms. This is not so in the Majorana scenario, and in fact we can make the identifications $\nu \equiv \hat{\nu}$ and $\bar{\nu} \equiv \nu^\dagger$ as Majorana fields are charge neutral by definition. So, in the Dirac scenario each generation of neutrino has four degrees of freedom, corresponding to left and right-handed states of the neutrino and anti-neutrino, whereas in the Majorana scenario there are only two degrees of freedom. One potentially measurable effect of this is in the detection of the relic neutrinos left over from the early Universe. This will be expanded upon in Chapter 4.

There is currently a large experimental effort to determine whether neutrinos are Majorana or Dirac fermions, by observing the presence or lack of neutrinoless double beta decay[18]–[22]. This process, where two nuclei undergo beta decay simultaneously but producing only electrons, is only possible if neutrinos behave as Majorana fields at low energies [23]. We will not focus on these experiments in the rest of this work, and only highlight the efforts here.

2.4 Oscillations

A well known, and experimentally observed [24], consequence of flavour mixing in the neutrino sector is *neutrino oscillations*. In this section we will analyse the pure Dirac

case, where there are only three non-degenerate masses. The standard derivation begins with a neutrino with flavour α and three momentum \mathbf{p} , which is created in a charged current weak interaction involving a charged lepton e_α . As explained in Section 2.1, we can relate the flavour states to the mass states using the PMNS matrix:

$$|\nu_\alpha\rangle = \sum_k (U_{\text{PMNS}})_{\alpha k}^* |\nu_k\rangle . \quad (2.4.1)$$

The mass states are eigenstates of the Hamiltonian of the free neutrinos, i.e. neutrinos in a vacuum will evolve in term in their mass states. The states are thus defined by:

$$\mathcal{H} |\nu_k\rangle = E_k |\nu_k\rangle , \quad (2.4.2)$$

where $E_k = \sqrt{|\mathbf{p}|^2 + m_k^2}$. The Schrödinger equation,

$$i \frac{d}{dt} |\nu_k(t)\rangle = \mathcal{H} |\nu_k(t)\rangle , \quad (2.4.3)$$

is solved by plane-wave solutions:

$$|\nu_k(t)\rangle = e^{-iE_k t} |\nu_k\rangle . \quad (2.4.4)$$

Thus, the flavour states evolve as:

$$|\nu_\alpha(t)\rangle = \sum_k U_{\alpha k}^* e^{-iE_k t} |\nu_k\rangle , \quad (2.4.5)$$

such that $|\nu_\alpha(0)\rangle = |\nu_\alpha\rangle$, where we have switched to $U \equiv U_{\text{PMNS}}$ for brevity. Using the fact that U_{PMNS} is a unitary matrix, we can also express mass states as linear

combinations of flavour states, i.e.

$$|\nu_k\rangle = \sum_{\alpha} U_{\alpha k} |\nu_{\alpha}\rangle. \quad (2.4.6)$$

Substituting this into Eq. (2.4.5), we find that for $t > 0$ the neutrino is actually a superposition of flavour states:

$$|\nu_{\alpha}(t)\rangle = \sum_{\beta} \sum_k U_{\alpha k}^* e^{-iE_k t} U_{\beta k} |\nu_{\beta}\rangle. \quad (2.4.7)$$

We can then define the transition amplitude between the initial flavour state α and another flavour state β at some time t :

$$\mathcal{A}_{\alpha\beta}(t) \equiv \langle \nu_{\beta} | \nu_{\alpha}(t) \rangle = \sum_k U_{\alpha k}^* U_{\beta k} e^{-iE_k t}, \quad (2.4.8)$$

where we have used the orthonormal condition on the flavour states $\langle \nu_{\alpha} | \nu_{\beta} \rangle = \delta_{\alpha\beta}$. From this amplitude we can find the probability of measuring a neutrino in the β flavour state (by observing a charged e_{β} lepton) after time t :

$$P_{\alpha\beta}(t) = |\mathcal{A}_{\alpha\beta}(t)|^2 = \sum_{k,j} U_{\alpha k}^* U_{\beta k} U_{\alpha j} U_{\beta j}^* \exp(-i(E_k - E_j)t). \quad (2.4.9)$$

For ultrarelativistic neutrinos, the dispersion relation can be approximated by

$$E_k \approx E + \frac{m_k^2}{2E}, \quad (2.4.10)$$

where $E \equiv |\mathbf{p}|$. Thus the energy difference in the probability is approximately

$$E_k - E_j \approx \frac{m_k^2 - m_j^2}{2E} \equiv \frac{\Delta m_{kj}^2}{2E}. \quad (2.4.11)$$

Since ultrarelativistic neutrinos propagate at (close to) the speed of light we can make another approximation, which is to equate time and propagation distance $t = L$. This is more convenient as often in oscillation experiments the distance of propagation is known well. The final, most general form of the oscillation probability is:

$$P_{\alpha\beta}(L) = \left| \mathcal{A}_{\alpha\beta}(L) \right|^2 = \sum_{k,j} U_{\alpha k}^* U_{\beta k} U_{\alpha j} U_{\beta j}^* \exp\left(-i \frac{\Delta m_{kj}^2 L}{2E}\right). \quad (2.4.12)$$

From this, we can find the *survival probability*, P_s , defined as the probability of detecting a neutrino in the same flavour state as it was originally produced in. This has a fairly simple form[17]:

$$P_s \equiv P_{\alpha\alpha}(L) = 1 - 4 \sum_{k>j} |U_{\alpha k}|^2 |U_{\alpha j}|^2 \sin^2\left(\frac{\Delta m_{kj}^2 L}{4E}\right). \quad (2.4.13)$$

This also defines a *disappearance probability*, $P_d \equiv 1 - P_s \equiv \sum_{\beta \neq \alpha} P_{\alpha\beta}$.

Three flavour oscillations have been confirmed experimentally, and measured over a range of sources and energies. The PMNS matrix is parametrised by four real numbers - the mixing angles, θ_{12}, θ_{13} , and θ_{23} , as well as one phase (assuming neutrinos are Dirac) δ_{CP} :

$$U_{\text{PMNS}} = \begin{pmatrix} c_{12}c_{13} & s_{12}c_{13} & s_{13}e^{-i\delta_{\text{CP}}} \\ -s_{12}c_{23} - c_{12}s_{23}s_{13}e^{i\delta_{\text{CP}}} & -c_{12}c_{23} - s_{12}s_{23}s_{13}e^{i\delta_{\text{CP}}} & s_{23}c_{13} \\ s_{12}s_{23} - c_{12}c_{23}s_{13}e^{i\delta_{\text{CP}}} & -c_{12}s_{23} - s_{12}c_{23}s_{13}e^{i\delta_{\text{CP}}} & c_{23}c_{13} \end{pmatrix} \quad (2.4.14)$$

where $s_{ab} \equiv \sin \theta_{ab}$ and $c_{ab} \equiv \cos \theta_{ab}$.

A useful quantity when studying neutrino oscillations is the *oscillation length*, defined as [17]

$$L_{\text{osc}}(E, \Delta m^2) \equiv \frac{4\pi E}{\Delta m^2}. \quad (2.4.15)$$

This is the distance at which the phase generated by Δm^2 is equal to 2π . It can be used to calculate the scale over which the oscillations occur.

2.4.1 Wave Packets and Decoherence

Whilst the previous, quantum mechanical, treatment is not the most rigorous, it has been shown to agree with more complicated QFT calculations [17]. However, there is one qualitative feature of a more formal treatment which is not present in the previous treatment. This is the phenomenon of decoherence.

In the previous calculations, the neutrino wave-functions were treated as plane waves. However this treatment cannot account for the fact that the production and detection of a neutrino are localised events. The solution to this problem is to introduce wave packets [17], which are constructed from superpositions of plane waves. They are usually treated as Gaussian envelopes with uncertainties in energy, position, time, and momentum. Oscillations only occur if the wave packets for the different mass states overlap.

Since the mass states have distinct mass, their wave packets will have different group velocities. If the distance between the production and detection of these neutrinos is large enough, the wave packets for each mass state will separate until they have exponentially small overlap. At this point, the neutrino oscillations no longer occur and the measured flavour ratio will be given purely by the mixing matrix [17][25]. This effect is what we will refer to as decoherence.

Decoherence will be important when we focus on Solar neutrinos, particularly in Chapter 3. We will not specify the value of the uncertainties of the wave packet, due to the difficulty in their calculation and measurement, and instead rely only on the qualitative effects of decoherence.

2.5 Neutrino Oscillations in Matter

Due to their weak interactions, neutrinos are able to travel through matter backgrounds over large distances without deflections. However, coherent forward elastic interactions, which leave the background and neutrino unchanged (i.e. no flavour changing or change in momentum) cannot be ignored. These interactions induce potentials in the Hamiltonian of the propagating neutrinos, affecting their evolution. We will focus on low temperature matter such that the only background fermions we need to consider are electrons, protons, and neutrons. The only charged current interaction which would have identical initial and final states would be between neutrinos and electrons. The effective Hamiltonian for this process is[17]:

$$\mathcal{H}_{\text{eff}}^{\text{CC}}(x) = 4\sqrt{2}G_F \left[\nu_e^\dagger(x) \bar{\sigma}^\mu e(x) \right] \left[e^\dagger(x) \bar{\sigma}_\mu \nu_e(x) \right]. \quad (2.5.1)$$

Anticommuting spinors obey the following Fierz identity[1]:

$$\left(z_1^\dagger \bar{\sigma}^\mu z_2 \right) \left(z_3^\dagger \bar{\sigma}_\mu z_4 \right) = 2 \left(z_1^\dagger z_3^\dagger \right) \left(z_2 z_4 \right) = \left(z_1^\dagger \bar{\sigma}^\mu z_4 \right) \left(z_3^\dagger \bar{\sigma}_\mu z_1 \right), \quad (2.5.2)$$

where the final equality is derived from the fact that $z_2 z_4 = z_4 z_2$. Performing the Fierz transformation on the CC interaction allows us to separate the neutrino and electron currents:

$$\mathcal{H}_{\text{eff}}^{\text{CC}}(x) = 4\sqrt{2}G_F \left[\nu_e^\dagger(x) \bar{\sigma}^\mu \nu_e(x) \right] \left[e^\dagger(x) \bar{\sigma}_\mu e(x) \right]. \quad (2.5.3)$$

After averaging over the momentum distribution of the background electron field and averaging over electron chiralities (assuming equal probabilities for left and right-handed), the final effective Hamiltonian becomes [17]:

$$\overline{\mathcal{H}}_{\text{eff}}^{\text{CC}}(x) = V_{\text{CC}} \nu_e^\dagger \bar{\sigma}^0 \nu_e, \quad (2.5.4)$$

where the potential is proportional to the local electron number density, N_e

$$V_{\text{CC}} = \sqrt{2}G_F N_e(x). \quad (2.5.5)$$

On the other hand, all background fermions can participate in neutral current interactions with the neutrinos. The Hamiltonian is derived from the Lagrangian to be:

$$\mathcal{H}_{\text{eff}}^{\text{NC}}(x) = 4\sqrt{2}G_F \sum_{\alpha} \left[\nu_{\alpha}^{\dagger} \bar{\sigma}^{\mu} \nu_{\alpha} \right] \sum_f \left[g_R^f \hat{f} \sigma_{\mu} \bar{f} + g_L^f f^{\dagger} \bar{\sigma}_{\mu} f \right] \quad (2.5.6)$$

where

$$\begin{aligned} g_L^e &= -\frac{1}{2} + \sin^2 \theta_W, & g_R^e &= \sin^2 \theta_W, \\ g_L^p &= \frac{1}{2} - \sin^2 \theta_W, & g_R^p &= -\sin^2 \theta_W, \\ g_L^n &= -\frac{1}{2}, & g_R^n &= 0. \end{aligned} \quad (2.5.7)$$

The effective Hamiltonian, after the averaging procedure performed on the CC potential, is then

$$\overline{\mathcal{H}}_{\text{eff}}^{\text{NC}} = \sum_{\alpha} \sum_f V_{\text{NC}}^f \nu_{\alpha}^{\dagger} \bar{\sigma}^0 \nu_{\alpha} \quad (2.5.8)$$

where the potential for fermion species f is

$$V_{\text{NC}}^f = \sqrt{2}G_F N_f g_V^f \quad (2.5.9)$$

for the "vector" coupling $g_V^f \equiv g_L^f + g_R^f$. In an electrically neutral background (at least on average), such as the plasma of the Sun or in the Earth, the number density of

electrons and protons is equal. As $g_V^e = -g_V^p$, the potentials are equal and opposite and so cancel. Thus only the neutron potential contributes and so:

$$V_{\text{NC}} \equiv \sum_{f \in \{e, p, n\}} V_{\text{NC}}^f = -\frac{G_F N_n}{\sqrt{2}}. \quad (2.5.10)$$

For neutrinos propagating through a medium with the properties under consideration, the Hamiltonian is a combination of the free Hamiltonian \mathcal{H}_0 , and the interaction Hamiltonians \mathcal{H}_I :

$$\mathcal{H} = \mathcal{H}_0 + \mathcal{H}_I \quad (2.5.11)$$

such that

$$\mathcal{H}_I |\nu_\alpha\rangle = (V_{\text{CC}} \delta_{\alpha e} + V_{\text{NC}}) |\nu_\alpha\rangle, \quad (2.5.12)$$

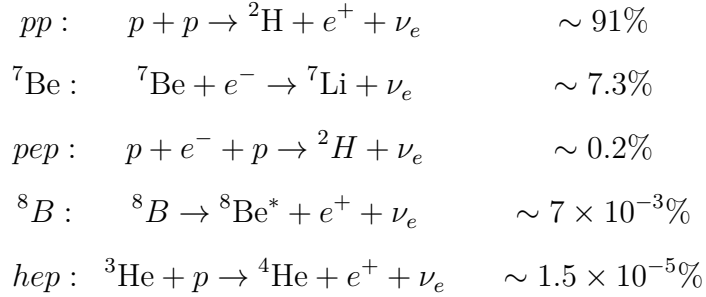
The implication here is that the eigenstates of the free Hamiltonian (the mass states) are not the same as the eigenstates of the interaction Hamiltonian (the flavour states). The neutrinos will thus propagate in the eigenstates of the total Hamiltonian.

2.6 Solar Neutrinos

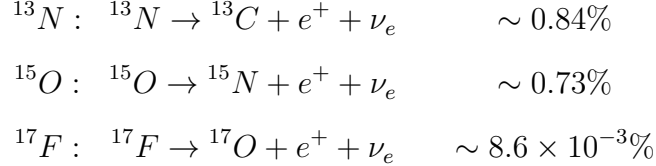
The results of the previous section are valid when the density profile is constant over the propagation length of the neutrinos. It turns out that the propagation of neutrinos through non-uniform density profiles can have drastically different features compared to vacuum or uniform matter propagation. We will focus on neutrinos produced in and propagating through the Sun, both because of the historical significance of Solar neutrinos to improving our understanding of fundamental neutrino properties, and also because of the relevance to Chapter 4.

Neutrinos are produced in the Sun by thermonuclear reactions. These reactions

form two distinct groups, known as the pp chain and the CNO cycle. The pp chain produces the vast majority of the total neutrino flux, with five distinct reactions that produce neutrinos. These reactions are labelled by their initial particles. In order of their contribution to the total neutrino flux, they are [17][7][26]:



The CNO cycle contributes a total of $\sim 1.5\%$ of the total neutrino flux from the Sun, however the exact value is dependent on the concentration of heavier elements in the Sun. The relevant processes are:



As shown in the reaction equations, the thermonuclear processes in the Sun produce only pure electron-neutrinos. These neutrinos are created with a range of energies, depending on the process of origin. Due to the kinematics of the process, the neutrinos produced in the ${}^7\text{Be}$ and pep processes are monochromatic in energy. The other pp -chain processes produce neutrinos with a β -form spectra given by [27]

$$\frac{d\phi}{dE_\nu} = \Phi A(x - E_\nu) \sqrt{(x - E_\nu)^2 - m_e^2} E_\nu^2 \quad (2.6.1)$$

where Φ is the total flux, A is the integral normalisation, and $x = Q + m_e$ with the characteristic energy of the process given by Q and m_e is the electron mass.

Solar neutrinos are also produced in large regions of the Sun, with radial distances of the order of $10\%R_\odot$. At the detector of a given experiment, there is no way to distinguish between a neutrino produced at, say, $r = 0.05R_\odot$, and one produced at $r = 0.1R_\odot$. To account for this, we need to average over the production region to produce an incoherently summed flux. If the production region is much larger than the typical oscillation length of the neutrinos, the oscillations will be *averaged out*, and lose all dependence on the mass splitting or energy

$$\bar{P}_{ee} = 1 - 2 \sum_{k>j} |U_{ek}|^2 |U_{ej}|^2. \quad (2.6.2)$$

As neutrinos are produced inside of the Sun, they are of course not travelling through a vacuum. In fact, they are actually propagating through a matter background with a density that varies over the propagation distance of the neutrino. To produce analytical results for the oscillation probabilities in this scenario, it is useful to look at the two-flavour oscillation scenario. This will prove useful in Chapter 3, but is also of interest for Solar neutrinos. This is because ν_μ and ν_τ both experience the same matter potential, and also because the energies of Solar neutrinos are too low to produce their respective charge muons in the detection process, meaning they are only detectable via NC interactions. We will thus combine the two flavours into one, which we label as a , such that $P_{ea} = P_{e\mu} + P_{e\tau}$.

In the two flavour case, the Hamiltonian in the flavour basis after removing constant factors (m_1^2 and V_{NC}) is given by

$$\mathcal{H}_F = \frac{1}{2E} U \Delta M^2 U^\dagger + V, \quad (2.6.3)$$

where

$$U = \begin{pmatrix} \cos \theta & \sin \theta \\ -\sin \theta & \cos \theta \end{pmatrix}, \quad \Delta M^2 = \begin{pmatrix} 0 & 0 \\ 0 & \Delta m^2 \end{pmatrix}, \quad V = \begin{pmatrix} V_{CC} & 0 \\ 0 & 0 \end{pmatrix}. \quad (2.6.4)$$

It is convenient to introduce the term $A_{CC} = 2EV_{CC}$ for the sake of algebra. The Hamiltonian can be combined into a single 2×2 matrix. After removing additional constant factors by a global rephasing, the Hamiltonian of interest is

$$\mathcal{H}_F = \frac{1}{4E} \begin{pmatrix} -\Delta m^2 \cos 2\theta + A_{CC} & \Delta m^2 \sin 2\theta \\ \Delta m^2 \sin 2\theta & \Delta m^2 \cos 2\theta - A_{CC} \end{pmatrix}. \quad (2.6.5)$$

As mentioned in the previous section, the neutrino fields will propagate in the basis which diagonalises this matrix, found by orthogonal transformations

$$\begin{aligned} \mathcal{H}_M &= U_M^T \mathcal{H}_F U_M \\ &= \frac{1}{4E} \begin{pmatrix} -\Delta m_M^2 & 0 \\ 0 & \Delta m_M^2 \end{pmatrix}, \end{aligned} \quad (2.6.6)$$

where the eigenvalue Δm_M^2 is

$$\Delta m_M^2 = \sqrt{(\Delta m^2 \cos 2\theta - A_{CC})^2 + (\Delta m^2 \sin 2\theta)^2}, \quad (2.6.7)$$

and the rotation matrix U_M is parametrised with a mixing angle θ_M such that

$$\tan 2\theta_M = \tan 2\theta \frac{\Delta m^2 \cos 2\theta}{\Delta m^2 \cos 2\theta - A_{CC}}. \quad (2.6.8)$$

To generalise these results to the case of a non-uniform matter density profile, we reintroduce the x dependence of the potential which arises from the matter density. This then promotes the mass splittings and mixing angles to also be functions. We

can express a differential equation of the flavour transition amplitudes in the matter background in matrix form as

$$i \frac{d}{dx} \begin{pmatrix} \mathcal{A}_{ee} \\ \mathcal{A}_{ea} \end{pmatrix} = \frac{1}{4E} \begin{pmatrix} -\Delta m_M^2 \cos 2\theta_M & \Delta m_M^2 \sin 2\theta_M \\ \Delta m_M^2 \sin 2\theta_M & \Delta m_M^2 \cos 2\theta_M \end{pmatrix}. \quad (2.6.9)$$

Taking the amplitude between an electron state and eigenstate of the Hamiltonian,

$$\tilde{\mathcal{A}}_{ei} = \langle \nu_e(0) | \nu_i(x) \rangle = \sum_{\alpha} (U_M)_{\alpha i} \langle \nu_e(0) | \nu_{\alpha}(x) \rangle, \quad (2.6.10)$$

which we can express as a vector of amplitudes

$$\mathcal{A} = U_M \tilde{\mathcal{A}}, \quad (2.6.11)$$

we can derive from Eq. (2.6.9) the differential equation for $\tilde{\mathcal{A}}$

$$i \frac{d\tilde{\mathcal{A}}}{dx} = \frac{1}{4E} \begin{pmatrix} -\Delta m_M^2 & -4E i d_x \theta_M \\ 4E i d_x \theta_M & \Delta m_M^2 \end{pmatrix}. \quad (2.6.12)$$

We have introduced the shorthand notation of $d_x \theta_M$ for the spatial derivative of the mixing angle θ_M . If the derivative is small, then the eigenstates of the Hamiltonian will remain the same, though the eigenvalues may change. The derivative can be readily calculated as

$$\frac{d\theta_M}{dx} = \frac{1}{2} \frac{\sin 2\theta_M}{\Delta m_M^2} \frac{dA_{CC}}{dx} \quad (2.6.13)$$

There are a number of cases in which this can take a small value. The most trivial of these is when the matter density is constant, or very slowly varying. To find the more general cases, it is often useful to consider the adiabaticity parameter

$$\gamma = \frac{\Delta m_M^2}{4E |d_x \theta_M|} = \frac{(\Delta m_M^2)^2}{2E \sin \theta_M |d_x A_{CC}|}. \quad (2.6.14)$$

When $\gamma \gg 1$, throughout the entire propagation length, the evolution of the neutrino states is *adiabatic*. The transitions between mass states are negligible, and the solution to Eq. (2.6.13) is given simply by [17]

$$\tilde{\mathcal{A}}_{e1}(x) = \exp\left(i \int_0^x dx' \frac{\Delta m_M^2(x')}{4E}\right) \tilde{\mathcal{A}}_{e1}(0), \quad (2.6.15)$$

$$\tilde{\mathcal{A}}_{e2}(x) = \exp\left(-i \int_0^x dx' \frac{\Delta m_M^2(x')}{4E}\right) \tilde{\mathcal{A}}_{e2}(0), \quad (2.6.16)$$

which can be calculated given a known matter density profile. The survival probability in this scenario, taking into account the initial and final mixings ($\theta_M^{(i)}$ and $\theta_M^{(f)}$ respectively), are then found to be:

$$P_{ee} = \frac{1}{2} - \frac{1}{2} \cos 2\theta_M^{(i)} \cos 2\theta_M^{(f)} + \frac{1}{2} \sin 2\theta_M^{(i)} \sin 2\theta_M^{(f)} \cos\left(\int_0^L \frac{\Delta m_M^2(x)}{2E} dx\right). \quad (2.6.17)$$

The final mixing angle is usually taken to be the vacuum one, as neutrino detectors are often placed relatively close to the vacuum of space (the distance through the overburden travelled by a neutrino is too small to induce different mixing).

2.6.1 Low Energy Regime

When the neutrino energy is sufficiently small, we can successfully treat matter effects as a perturbation to the Hamiltonian. Choosing our perturbation parameter to be

$$\alpha \equiv \frac{A_{CC}}{\Delta m^2 \cos 2\theta} \equiv \frac{2\sqrt{2}G_F N_e E}{\Delta m^2 \cos 2\theta}, \quad (2.6.18)$$

we can readily create perturbative expansions of Δm_M^2 and $\tan 2\theta$:

$$\Delta m_M^2 = \Delta m^2 \left(1 - \alpha \cos^2 2\theta + \frac{\alpha^2}{8} \sin^2 4\theta + \mathcal{O}(\alpha^3) \right), \quad (2.6.19)$$

$$\tan 2\theta_M = \tan 2\theta \left(1 + \alpha + \alpha^2 + \mathcal{O}(\alpha^3) \right). \quad (2.6.20)$$

From this last equation, we can also find corrections to the mixing angle explicitly

$$\theta_M = \theta + \frac{\sin 4\theta}{4} \alpha + \frac{\cos^3 2\theta \sin 2\theta}{2} \alpha^2 + \mathcal{O}(\alpha^3) \quad (2.6.21)$$

If we are in the small α limit, either because the neutrino energy or the background density are small, we can approximately ignore matter effects altogether. Combining this with the adiabatic evolution limit, the averaged oscillation probabilities reduce to the vacuum mixing with no dependence on the propagation length:

$$\bar{P}_{ee} = \frac{1 + \cos^2 2\theta}{2}, \quad (2.6.22)$$

$$\bar{P}_{ea} = \frac{1 - \cos^2 2\theta}{2}. \quad (2.6.23)$$

2.6.2 Three Generation Solar Neutrinos

Experiments have confirmed that there are three distinct flavours of charged leptons. In the SM, this would mean we would have three flavours of neutrino. We will assume that any modifications to the SM would be to add particles, rather than remove them. As such there should be at least three flavours of neutrino.

On top of this, there is overwhelming evidence from neutrino oscillation experiments that there are at least two neutrino states which have non-zero mass. We will now examine how applicable the results for two-flavour Solar neutrinos are to probabilities

in the three neutrino generation scheme.

As we have seen previously, the existence of three generations of neutrino requires three independent mixing angles θ_{12} , θ_{13} , and θ_{23} . There are also two independent mass-squared splittings, Δm_{21}^2 and Δm_{31}^2 , from which we can construct a third - $\Delta m_{32}^2 = \Delta m_{31}^2 - \Delta m_{21}^2$. Note that we have assumed NO of the masses, however the results for IO can be found by swapping $\Delta m_{31}^2 \leftrightarrow -\Delta m_{32}^2$, and the estimates will generally remain true.

We will first look for the regimes in which matter effects can be ignored by defining a critical energy E_m , below which the perturbative expansion is valid. This value will be the energy at which $\alpha = 1$. If we use the two-flavour definition of α , and treat each combination of $\theta_{ij}, \Delta m_{ij}^2$ as the parameters for the two-flavour oscillations, we find

$$E_m \approx \begin{cases} 540 \text{ keV}, & \theta_{12} = 33.41^\circ \text{ and } \Delta m_{21}^2 = 7.41 \times 10^{-5} \text{ eV}^2 \\ 45 \text{ MeV}, & \theta_{13} = 8.58^\circ \text{ and } \Delta m_{31}^2 = 2.51 \times 10^{-3} \text{ eV}^2 \\ 4.4 \text{ MeV}, & \theta_{23} = 42.4^\circ \text{ and } \Delta m_{32}^2 = 2.44 \times 10^{-3} \text{ eV}^2 \end{cases} \quad (2.6.24)$$

where we have taken the electron density to be $N_e = 245 N_A \text{ cm}^{-3}$, which is greater than that predicted from models of the core of the Sun, thus ensuring the validity of the above results. If we restrict ourselves to neutrinos with $E \lesssim 1 \text{ MeV}$, we need only consider the matter effects on the oscillations produced by Δm_{12}^2 . Furthermore, the typical oscillation lengths for the other two mass-squared differences for these energies will be small compared to the size of the production region:

$$L_{\text{osc}} \lesssim 300 \text{ m} \ll \Delta R, \quad (2.6.25)$$

where ΔR is the approximate width of the production region which is typically $\mathcal{O}(10\%)R_\odot$. We can thus safely assume that oscillations produced by the larger mass splittings are incoherently averaged out. This motivates the use of the two-

flavour results, with $\Delta m^2 \equiv \Delta m_{21}^2$. In fact, the Δm_{21}^2 mass-squared splitting is often referred to as the "solar" mass-squared splitting, due to its dominant effect on Solar neutrinos.

The only process in the Sun which produces neutrinos which all have energy below 500 keV is the pp process. This has a maximum energy threshold of $Q \approx 420$ keV. At these energies, $\alpha \approx 0.78$ which, while smaller than 1, is still large (naively, we would need to go to 10th order in the expansion to get a less than 10% error). Instead, we can perform an expansion in $\sin \theta_{13}$ which from experimental measurements we know to be small. To first order in this expansion, the survival probability can be shown to be [28]:

$$P_{ee} \approx 1 - \frac{\sin^2 2\theta_{12}}{C_{12}^2} \sin^2 \left(\frac{\Delta m_{21}^2 C_{12} L}{4E} \right), \quad (2.6.26)$$

where

$$C_{12} \equiv \sqrt{\sin^2 2\theta_{12} + \left(\cos 2\theta_{12} - \frac{2EV_{CC}}{\Delta m_{21}^2} \right)^2}. \quad (2.6.27)$$

We can write out the oscillation length for this probability directly from this form, which we find to be

$$L_{12} \equiv \frac{4\pi E}{\Delta m_{21}^2 C_{12}} \lesssim 15 \text{ km}, \quad (2.6.28)$$

where the numerical result is for a neutrino with energy 420 keV. Once again, this is much smaller than the production region of pp neutrinos, and so all oscillation effects are averaged out. Thus, the survival probability for pp neutrinos is just proportional to the mixing from the PMNS matrix:

$$\bar{P}_{ee} \approx \sum_i |(U_{\text{PMNS}})_{ei}|^4. \quad (2.6.29)$$

We will make use of this in Chapter 3 when studying oscillations in pp neutrinos under the pseudo-Dirac scenario.

Chapter 3

Probing the pseudo-Dirac scenario using Solar neutrinos at JUNO

It was shown in Section 2.2.2 that the pseudo-Dirac scenario of neutrino mass generation is characterised by small mass-squared splittings between almost degenerate pairs of Majorana neutrinos, with close to maximal mixing. As the oscillation length for pairs of neutrinos is given by

$$L_{\text{osc}} \equiv \frac{4\pi E}{\delta m^2}, \quad (3.0.1)$$

we would expect oscillations to occur over longer distances compared to those due to the currently known mass splittings Δm_{21}^2 and Δm_{31}^2 . To observe these oscillations we are interested in sources of neutrinos which propagate over long distances before being detected, and also ideally have low energies. This motivates Solar neutrinos as ideal candidates for this purpose, as the Earth-Sun distance is $\sim 150 \times 10^6$ km and have energies typically in the range $\mathcal{O}(100 \text{ keV}) - \mathcal{O}(1 \text{ MeV})$. From these values, we would expect to be sensitive to mass splittings $\gtrsim 10^{-12} \text{ eV}^2$, however this depends on the capability of the experiment to measure lower energy neutrinos among other things.

For this work, we will look at the capabilities of the near-future Jiangmen Underground Neutrino Observatory (JUNO) experiment.

3.1 Solar Neutrinos at JUNO

JUNO is a multi-purpose neutrino experiment proposed in 2008, with a primary objective to determine the neutrino mass ordering [29]. JUNO will constrain this parameter by measuring reactor Antineutrinos' survival probability from the Yangji-ang and Taishan nuclear power plants (NPPs). The neutrino detector is a liquid scintillator with a 20-kilotonne fiducial mass 53 km from the two NPPs. While primarily designed to detect reactor antineutrinos via inverse beta decay, JUNO can also detect solar neutrinos through elastic neutrino electron scattering,

$$\nu_\alpha + e^- \longrightarrow \nu_\alpha + e^-,$$

where α is the flavour of the incident neutrino. The differential cross-section of this process, to first order in the effective weak interaction, is

$$\frac{d\sigma^{(\alpha)}}{dE_r} = \frac{2G_F^2 m_e}{\pi} \left[g_L^{(\alpha)2} + g_R^2 \left(1 - \frac{E_r}{E_\nu} \right)^2 - g_L^{(\alpha)} g_R \frac{m_e E_r}{E_\nu^2} \right], \quad (3.1.1)$$

where G_F is the Fermi constant, E_r is the recoil energy of the outgoing electron, m_e is the electron mass, E_ν is the energy of the incident neutrino and $g_L^{(\alpha)}$, g_R , are the (flavour dependent) coupling constants, which are related to the weak mixing angle θ_W via

$$g_L^{(\alpha)} = \sin^2 \theta_W - \frac{1}{2} + \delta_{\alpha,e}, \quad (3.1.2)$$

$$g_R = \sin^2 \theta_W. \quad (3.1.3)$$

The delta function in flavour space arises from the enhancement of $e^- - \nu_e$ scattering due to the additional charged-current interaction. The differential event rate of measured electrons in the detector can be expressed as [27]

$$\frac{dR^{i,a}}{dE_r} = N_e \sum_\alpha \frac{d\sigma^{(\alpha)}}{dE_r} \int dE_\nu P_{e\alpha}(E_\nu) \frac{d\phi^a}{dE_\nu}, \quad (3.1.4)$$

Source	Φ (cm ⁻² s ⁻¹)	Q (keV)	A (keV ⁻⁵)
pp	5.98×10^{10}	420	1.9232×10^{-13}
${}^7\text{Be}$	4.93×10^9	862, 384	N/A

Table 3.1: Parameters for the differential fluxes of solar neutrino sources used in this work, from [27]

where N_e is the number of electrons per kilotonne in the target medium, $d\sigma^{(\alpha)}/dE_r$ is the differential cross section for neutrino-electron scattering as shown in Eq. (3.1.1), and $P_{e\alpha}$ is the probability for a neutrino with flavour α arriving at the detector from the Sun. The index a runs over the solar neutrino sources, pp and ${}^7\text{Be}$. Their differential spectra $d\phi^a/dE_\nu$ can either be monochromatic in energy as is the case for ${}^7\text{Be}$ neutrinos or have a continuous β form such as the pp neutrino source:

$$\frac{d\phi}{dE_\nu} = \Phi A(x - E_\nu) \left[(x - E_\nu)^2 - m_e^2 \right]^{\frac{1}{2}} E_\nu^2, \quad (3.1.5)$$

where $x = Q + m_e$ with Q being the characteristic energy. The total flux Φ , characteristic energy Q , and integral normalisation A are given in table Table 3.1. The ${}^7\text{Be}$ flux has two monochromatic lines at two different energies, with one at 384 keV making up 10% of the total flux and another at 862 keV contributing the remaining 90% [27], [30]. For a neutrino with energy E_ν , the maximum electron recoil energy possible from scattering is given by:

$$E_r^{\max} = \frac{2E_\nu^2}{m_e + 2E_\nu}. \quad (3.1.6)$$

We can equivalently use this relation to find the minimum neutrino energy we must consider when calculating the differential cross section at some recoil energy E_r :

$$E_\nu^{\min} = \frac{1}{2} \left(E_r + \sqrt{E_r^2 + 2E_r m_e} \right), \quad (3.1.7)$$

which is the lower integration boundary in Eq. (3.1.4) and Q_a is the upper boundary.

JUNO will be sensitive to both pp and ${}^7\text{Be}$ neutrinos and other sources such as pep and CNO neutrinos, though with a lower signal-to-noise ratio. This sensitivity can be used to constrain the parameter space for pseudo-Dirac neutrinos via a solar oscillation analysis which is the objective of this work. Nevertheless, the measurement of solar neutrinos in JUNO will depend on the control of backgrounds that affect the low-energy region. Such backgrounds appear due to the resemblance of the neutrino-electron scattering signal to the weak decay of isotopes present in the detector. Specifically, a neutrino-electron scattering produces isotropic light with no additional signature, making it indistinguishable from a background one[31][32]. In JUNO, the most important background sources are the impurities in the scintillator. Other sources can be reduced by various techniques such as choosing a different fiducial volume [31]. The largest background affecting the solar neutrino measurement is the ${}^{14}\text{C}$ beta decay process, which completely dominates below 156 keV. If this background is under sufficient control, it can be removed by cutting recoil energies at around 200 keV, which sets a minimum neutrino energy of ~ 350 keV. This allows for the measurement of the high energy part of the pp neutrinos. For energies above the ${}^{14}\text{C}$ background cut, ${}^{210}\text{Bi}$, ${}^{85}\text{Kr}$, and ${}^{238}\text{U}$ will be the main sources of scintillation backgrounds. Since it is still unclear if the ${}^{14}\text{C}$ and possible pile-ups would affect recoil energies larger than ~ 400 keV, we consider three different situations for the energy threshold in what follows. First, an optimistic case where the radiopurity of the scintillator is low enough to have the carbon background and possible pile-ups under control for energies above 200 keV. Second, a more conservative approach where the energy threshold is set to be 450 keV, similar to the analysis performed by the JUNO collaboration in Ref. [32]. We anticipate that the final sensitivity of JUNO will lie between these scenarios, so we have also included a third case for a cut at 250 keV to demonstrate how the sensitivity may vary.

3.2 The Three Generation Pseudo-Dirac Scenario

In Section 2.2.2, we introduced the pseudo-Dirac scenario in the case of one generation of neutrinos. However, in the SM we know there are three generations of neutrino as there were three generations of left-handed leptons, which was constructed to align with the observations of three different charged leptons. This is further backed up by observational evidence from cosmology [33] which prefers three active neutrinos in the early Universe. As such, we will briefly review the pseudo-Dirac scenario for three active neutrinos.

Since we are in the pseudo-Dirac limit, we can treat the Majorana mass matrix m as a small perturbation. We thus begin by diagonalising the mass matrix $\tilde{M} = M - m$:

$$\tilde{M} = \begin{pmatrix} 0 & M_D \\ M_D^T & 0 \end{pmatrix}. \quad (3.2.1)$$

We saw in Section 2.1 that M_D can be diagonalised using two 3×3 matrices, which we now refer to as U_D and V_D , such that $\hat{M} = U_D^\dagger \tilde{M} V_D$, where \hat{M} is the diagonal matrix of eigenvalues of \tilde{M} . If we construct the following 6×6 unitary matrix:

$$U \equiv \begin{pmatrix} U_D & 0 \\ 0 & V_D^* \end{pmatrix}, \quad (3.2.2)$$

we can diagonalise the matrix $\tilde{M}^\dagger \tilde{M}$:

$$U^\dagger (\tilde{M}^\dagger \tilde{M}) U = \begin{pmatrix} \hat{M}^2 & 0 \\ 0 & \hat{M}^2 \end{pmatrix}. \quad (3.2.3)$$

This matrix clearly has degenerate eigenvalues, since the matrix \hat{M} is repeated twice. It is also valuable to notice that we have gone from having a Dirac mass term to two Majorana masses. This makes evident that we can represent a Dirac fermion as two different Majorana fermions, in the same way that we can also decompose a

Dirac fermion into two Weyl fermions.

If we now reintroduce the corrections due to the small matrix m , ignoring any terms proportional to m^2 , we find an almost diagonal matrix:

$$U^\dagger(M^\dagger M)U \approx \begin{pmatrix} \hat{M}^2 & \epsilon \hat{M} \\ \epsilon^\dagger \hat{M} & \hat{M}^2 \end{pmatrix}, \quad (3.2.4)$$

where we have parametrised the off diagonal elements, which are proportional to \hat{M} , with the matrix ϵ . We are principally interested in the effect of the perturbation on the eigenvalues of the matrix. This is because, since the scale of the eigenvalues of \hat{M} are large compared to the scale of the perturbation, corrections between non-degenerate eigenvalues will be relatively small and have little effect. On the other hand, the degenerate eigenvalues are identical before the perturbation, so the effects will be more significant. This is also motivated by the outcome of the one-generation analysis in Section 2.2.2. We can manipulate the quasi-diagonal matrix using a series of permutation matrices to produce a block partitioned matrix, where the diagonal blocks are 2×2 matrices with degenerate eigenvalues along the diagonal. Explicitly, we have:

$$\mathcal{O}^T U^\dagger(M^\dagger M)U \mathcal{O} = \begin{pmatrix} \mathfrak{M}_{11} & \mathfrak{M}_{12} & \mathfrak{M}_{13} \\ \mathfrak{M}_{21} & \mathfrak{M}_{22} & \mathfrak{M}_{23} \\ \mathfrak{M}_{31} & \mathfrak{M}_{32} & \mathfrak{M}_{33} \end{pmatrix}, \quad (3.2.5)$$

where

$$\mathfrak{M}_{ii} = \begin{pmatrix} \hat{M}_i^2 & \epsilon_i^* \hat{M}_i \\ \epsilon_i \hat{M}_i & \hat{M}_i^2 \end{pmatrix}. \quad (3.2.6)$$

The effect of diagonalising the quasi-diagonal matrix will be to generate shifts in the original eigenvalues of the Dirac mass matrix, as well as to induce splittings between the degenerate pairs of eigenvalues. We parametrise the shifts by relabelling the

eigenvalues, and the splittings by δm^2 . From matrix perturbation theory, we find that the mixing matrix is chosen such that the block diagonal terms diagonalise the block diagonals of the mass matrix, and we can ignore off diagonal blocks since they are further suppressed by factors of $1/\Delta m_{ij}^2$ [34], where Δm_{ij}^2 are the differences between the original, non-degenerate eigenvalues. Thus, our full unitary diagonalisation matrix is given by

$$\mathcal{V} = U\mathcal{O}U_{\text{PD}}, \quad (3.2.7)$$

where the pseudo-Dirac rotation matrix is

$$U_{\text{PD}} \equiv \begin{pmatrix} U_{14} & 0_2 & 0_2 \\ 0_2 & U_{25} & 0_2 \\ 0_2 & 0_2 & U_{36} \end{pmatrix}. \quad (3.2.8)$$

and by 0_2 we refer to the 2×2 zero matrix. The rotation sub-matrices between mass states i and j are parametrised in the usual way as

$$U_{ij} \equiv \begin{pmatrix} \cos \theta_{ij} & \sin \theta_{ij} \\ -e^{-i\phi_i} \sin \theta_{ij} & e^{-i\phi_i} \cos \theta_{ij} \end{pmatrix}, \quad (3.2.9)$$

with arbitrary real phases ϕ_i . This provides a large simplification over the most general case, where the 6×6 unitary matrix would be parametrised by multiplying 15 complex rotation matrices [35].

We now have six distinct mass states, corresponding to the six distinct eigenvalues, which behave as Majorana fermions in the absence of interactions. This aligns with the previous statements of a free Dirac fermion being equivalent to two Majorana fermions, and the small perturbation in mass breaks the degeneracy between the two Majorana fermions to produce distinct states. The structure of the ordering mass values is pictured in Fig. 3.1.

The matrix \mathcal{V} can be used to relate between the mass eigenstates, and the interaction eigenstates. We will label those neutrinos that participate in weak interactions as *active* states, ν_α with $\alpha \in \{e, \mu, \tau\}$, and those that do not interact as *sterile* states, ν_s . We make no distinction between the sterile states as they have no distinguishing features in experimental observations unlike the active states, but note that they occupy a three-dimensional subspace. Following on from the diagonalisation of the mass matrix, we have that:

$$\nu_i = \mathcal{V} \begin{pmatrix} \nu_\alpha \\ \nu_s \end{pmatrix}, \quad (3.2.10)$$

where we have simply relabelled the original 3-vectors of left-handed states: $\nu_\alpha \equiv \boldsymbol{\nu}$ and $\hat{\boldsymbol{\nu}} \equiv \nu_s$.

In the limit of $\delta m^2 \ll \Delta m^2$, where we can treat the mass matrix in Eq. (3.2.5) as being completely block diagonal, the mixing between the mass eigenstates becomes maximal just as in the one-generation case, such that $\theta_{14} = \theta_{25} = \theta_{36} = \pi/4$, and the mixing matrix \mathcal{V} can be parametrised as[35]

$$\mathcal{V} = \begin{pmatrix} U_{\text{PMNS}} & 0 \\ 0 & U_R \end{pmatrix} \cdot \frac{1}{\sqrt{2}} \begin{pmatrix} 1_3 & i1_3 \\ \varphi & -i\varphi \end{pmatrix}, \quad (3.2.11)$$

where $\varphi = \text{diag}(e^{-i\phi_1}, e^{-i\phi_2}, e^{-i\phi_3})$ is a matrix containing the arbitrary phases, and 1_3 denotes the 3×3 identity matrix. The neutrino fields, in the flavour basis, take a simple form in this limit,

$$\nu_\alpha = \frac{(U_{\text{PMNS}})_{\alpha k}}{\sqrt{2}} (\nu_k + i\nu_{k+3}), \quad (3.2.12)$$

for $k \in \{1, 2, 3\}$. From this, we observe that a flavour eigenstate is a maximally-mixed superposition of two mass eigenstates with almost degenerate masses.

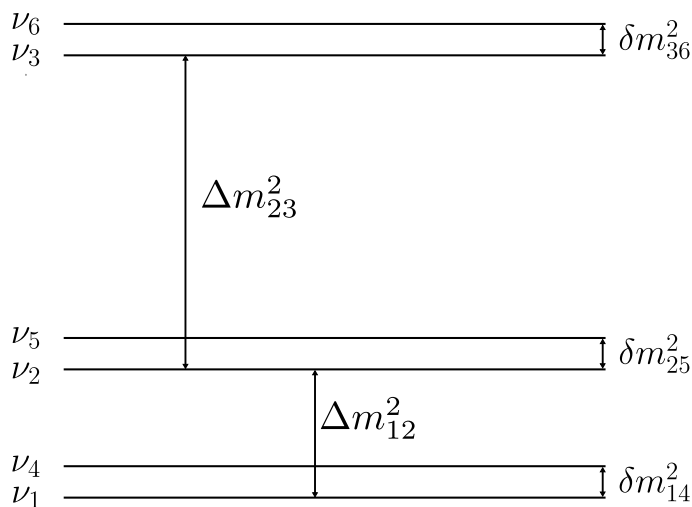


Figure 3.1: The neutrino mass spectrum in the three-generation pseudo-Dirac scenario. We choose, as a matter of convention, to have the standard mass squared differences, Δm_{ij}^2 , to be between the smaller of the mass pairs. These mass pairs are almost degenerate, except for a small mass squared difference δm_{ij}^2 .

3.3 Pseudo-Dirac Neutrino Oscillations

It is fairly trivial to generalise the neutrino oscillation framework introduced in Section 2.4 to the pseudo-Dirac case. The free Hamiltonian in the ultrarelativistic approximation, for a neutrino with energy E_ν , is

$$\mathcal{H}_0 = \frac{1}{2E_\nu} \Delta M_d^2, \quad (3.3.1)$$

where ΔM_d^2 is a matrix with diagonal elements equal to the mass squared values found in the previous section minus an overall constant of m_1^2 , i.e. $\Delta M_d^2 = M_d^2 - m_1^2 I$. In order to take matter effects into account, we must also include the interaction Hamiltonian. As described in Section 2.5, the active neutrino states will experience a potential proportional to the Fermi constant and the background density of fermions. On the other hand, the sterile states will have no potential due to their lack of interactions, so the interaction Hamiltonian in the flavour basis is then

$$\mathcal{H}_I = \sqrt{2}G_F \text{diag}(2N_e - N_n, -N_n, -N_n, 0, 0, 0) \quad (3.3.2)$$

where N_e and N_n are the electron and neutron number density of the background matter field, respectively. Unlike in the standard scenario, we are not able to remove the contribution to the potential from the neutron background by a simple re-phasing due to the addition of the new sterile neutrino states.

In the scenario where the pseudo-Dirac mass splittings are much smaller than the standard ones, $\delta m^2 \ll \Delta m_{ij}^2$, matter effects will only affect the propagation of the pseudo-Dirac pairs. We can thus treat the oscillations between pseudo-Dirac pairs as two flavour oscillations, which provide corrections to the standard oscillation probabilities. This is because we are interested in low and intermediate-energy solar neutrinos, so we can consider analytical approximations to the oscillation probabilities [36]. For pp neutrinos, which have energy $E_\nu \lesssim 420$ keV, the standard matter effects are negligible, and thus we can approximate the mixing as modifying the standard solar oscillation probabilities by including active-sterile oscillation of each pair. At these energies, the standard vacuum oscillations average out the distance-dependent factors due to the large production region leaving only powers of the PMNS matrix elements. This simplifies the form of the oscillation probabilities:

$$\begin{aligned} P_{ee} &= |U_{e1}^{3f}|^4 P_{ee}^{2f}(\theta_{14}, \delta m_1^2) \\ &+ |U_{e2}^{3f}|^4 P_{ee}^{2f}(\theta_{25}, \delta m_2^2) \\ &+ |U_{e3}^{3f}|^4 P_{ee}^{2f}(\theta_{36}, \delta m_3^2), \end{aligned} \quad (3.3.3a)$$

$$\begin{aligned} P_{es} &= |U_{e1}^{3f}|^2 \left(1 - P_{ee}^{2f}(\theta_{14}, \delta m_1^2)\right) \\ &+ |U_{e2}^{3f}|^2 \left(1 - P_{ee}^{2f}(\theta_{25}, \delta m_2^2)\right) \\ &+ |U_{e3}^{3f}|^2 \left(1 - P_{ee}^{2f}(\theta_{36}, \delta m_3^2)\right), \end{aligned} \quad (3.3.3b)$$

$$P_{ea} = 1 - P_{ee} - P_{es}. \quad (3.3.3c)$$

where P_{ee} is the electron neutrino survival probability and P_{es} (P_{ea}) the electron neutrino to sterile (other active flavour) oscillation probability. Separating the muon and tau flavour probabilities is unnecessary as they have identical contributions to the scattering cross section, as was discussed in Section 3.1. We can further approximate the two-neutrino oscillation probabilities by analysing the matter effects on the evolution of each pseudo-Dirac pair, depending on the regime of the mass-squared splitting value.

3.3.1 MSW Regime

When the pseudo-Dirac mass splittings satisfy

$$10^{-10} \text{ eV}^2 \lesssim \delta m^2 \lesssim 10^{-6} \text{ eV}^2 ,$$

we must take into account the effect of non-adiabatic transitions through a resonant region in the Sun, i.e. the MSW effect. However, vacuum oscillations are averaged for mass splittings in this range, so we can remove any dependence on the Earth-Sun distance. To take into account the non-adiabaticity of the Solar density profile in this regime, it is necessary to introduce the crossing probability P_c , which for an exponential density profile is given by [37]–[39]

$$P_c = \frac{e^{-\gamma \sin^2 \theta} - e^{-\gamma}}{1 - e^{-\gamma}} , \quad (3.3.4)$$

where θ is the mixing angle between the two neutrino states, and the non-adiabaticity parameter is given by [38], [39]

$$\gamma = 2\pi r_0^{ij} \frac{\delta m_{ij}^2}{2E_\nu} , \quad (3.3.5)$$

with r_0^{ij} a distance obtained by performing an exponential fit of the matter potential inside the Sun, $N_{ij}(r) = N_0^{ij} \exp(-r/r_0^{ij})$. Such a matter potential will depend on

the specific pseudo-Dirac scenario to be tested [36],

$$N_{ij}(r) = \begin{cases} N_e(r) \cos^2 \theta_{13} \cos^2 \theta_{12} - \frac{1}{2} N_n(r) & ij = 14 \\ N_e(r) \cos^2 \theta_{13} \sin^2 \theta_{12} - \frac{1}{2} N_n(r) & ij = 25 \\ N_e(r) \sin^2 \theta_{13} - \frac{1}{2} N_n(r) & ij = 36 \end{cases} \quad (3.3.6)$$

For our purposes, we consider the electron and neutron number densities predicted by the Solar Model AGSS09 from Ref. [40].

The active-sterile two-neutrino probability, averaged over the production region, will then follow the Parke formula [37]

$$P_{ee}^{2f}(\theta_{ij}, \delta m_{ij}^2) = \frac{1}{2} + \left(\frac{1}{2} - P_c \right) \cos 2\theta_{ij}^m \cos 2\theta_{ij}, \quad (3.3.7)$$

where $ij = \{14, 25, 36\}$, and the usual expression gives the effective mixing angle in the Sun

$$\cos 2\theta_{ij}^m = \frac{\delta m_{ij}^2 - A_0^{ij}}{\sqrt{(\delta m_{ij}^2 \cos 2\theta_{ij} - A_0^{ij})^2 - (\delta m_{ij}^2 \sin 2\theta_{ij})^2}}, \quad (3.3.8)$$

with

$$A_0^{ij} \equiv 2\sqrt{2}E_\nu G_F N_0^{ij}. \quad (3.3.9)$$

3.3.2 Quasi-Vacuum Oscillations

When we are in the regime where

$$10^{-11} \text{ eV}^2 \lesssim \delta m^2 \lesssim 10^{-10} \text{ eV}^2,$$

both the matter effects and the vacuum oscillations play an important role in the pseudo-Dirac oscillations probabilities.

In this intermediate situation, we can recast the analytical approximations obtained for a two-flavour oscillation in Refs [38], [39] to

$$\begin{aligned}
P_{ee}^{2f}(\theta_{ij}, \delta m_{ij}^2) &= P'_c \cos^2 \theta_{ij} + (1 - P'_c) \sin^2 \theta_{ij} \\
&\quad - \sqrt{P'_c(1 - P'_c)} \cos 2\theta_{ij}^m \sin 2\theta_{ij} \cos\left(\frac{\delta m_{ij}^2 L_\odot}{2E_\nu}\right),
\end{aligned} \tag{3.3.10}$$

where

$$P'_c = P_c \sin^2 \theta_{ij}^m + (1 - P_c) \cos^2 \theta_{ij}^m, \tag{3.3.11}$$

and L_\odot is the Sun-Earth distance.

3.3.3 Vacuum Oscillation Regime

For

$$\delta m^2 \lesssim 10^{-11} \text{ eV}^2$$

the oscillation length is of the order of, or larger than, the radius of the Sun. Furthermore, the matter potential completely dominates the Hamiltonian, and so neutrinos will propagate in their flavour states whilst in the Sun. Thus, the two-neutrino probability will have the standard form in vacuum,

$$P_{ee}^{2f}(\theta_{ij}, \delta m_{ij}^2) = 1 - \sin^2(2\theta_{ij}) \sin^2\left(\frac{\delta m_{ij}^2 L_\odot}{4E_\nu}\right). \tag{3.3.12}$$

3.3.4 Higher Energy ${}^7\text{Be}$ Neutrinos

For the higher energy ${}^7\text{Be}$ neutrino line, at 862 keV, the previous analytic approximations would lead to probabilities that do not reproduce the correct values due to matter effects affecting the active neutrinos. Thus, numerical calculations were performed using the *slab approximation* method [17]. This involves the discretisation of the matter density profile of the Sun into slabs of constant density with some length Δx , through which the propagation of the neutrino amplitude can be calculated. Thus, the amplitude of a neutrino after passing through a varying density profile

can be approximated as

$$\mathcal{A} = \prod_{s=0}^N \mathcal{V}_s \exp\left(-i \frac{m_s^2 \Delta x_s}{2E_\nu}\right) \mathcal{V}_s^\dagger \mathcal{A}_0, \quad (3.3.13)$$

where \mathcal{V}_s and m_s^2 are the effective mixing matrix and effective mass squared difference matrix, respectively, in the slab s . These are obtained by diagonalising the Hamiltonian in the medium. The initial amplitude, \mathcal{A}_0 , for solar neutrinos, which are produced as pure ν_e states, is $(1, 0, 0, 0, 0, 0)^T$ in the flavour basis. We can obtain the probability from the amplitude:

$$P_{e\alpha}^{1\nu} = |\mathcal{A}_\alpha|^2. \quad (3.3.14)$$

However, this is only for a single neutrino originating from one position. In reality, the Sun produces many neutrinos over a large region. Since we do not know where a detected neutrino was produced, we must average the probability over the entire production region yielding the Solar probability:

$$P_{e\alpha} = \int_{r_a}^{r_b} dr \rho(r) P_{e\alpha}^{1\nu}(r) \approx \sum_{i=0}^N \rho(r_i) P_{e\alpha}^{1\nu}(r_i), \quad (3.3.15)$$

where ρ is the production probability as a function of the radial position in the Sun, and $P_{e\alpha}^{1\nu}$ now depends on where the neutrino was produced. For this work, we approximate ρ as a window function between $0.02 R_\odot$ and $0.125 R_\odot$ for ${}^7\text{Be}$, which we found to be within a few percent of the probability calculated using theoretical predictions of ρ . This is a reasonable approximation as, qualitatively, the averaged probability depends primarily on the length over which it is averaged rather than the exact distribution of the production. Further, the production region for ${}^7\text{Be}$ is highly concentrated over this region [30] and so should be approximated well by a uniform distribution over this length.

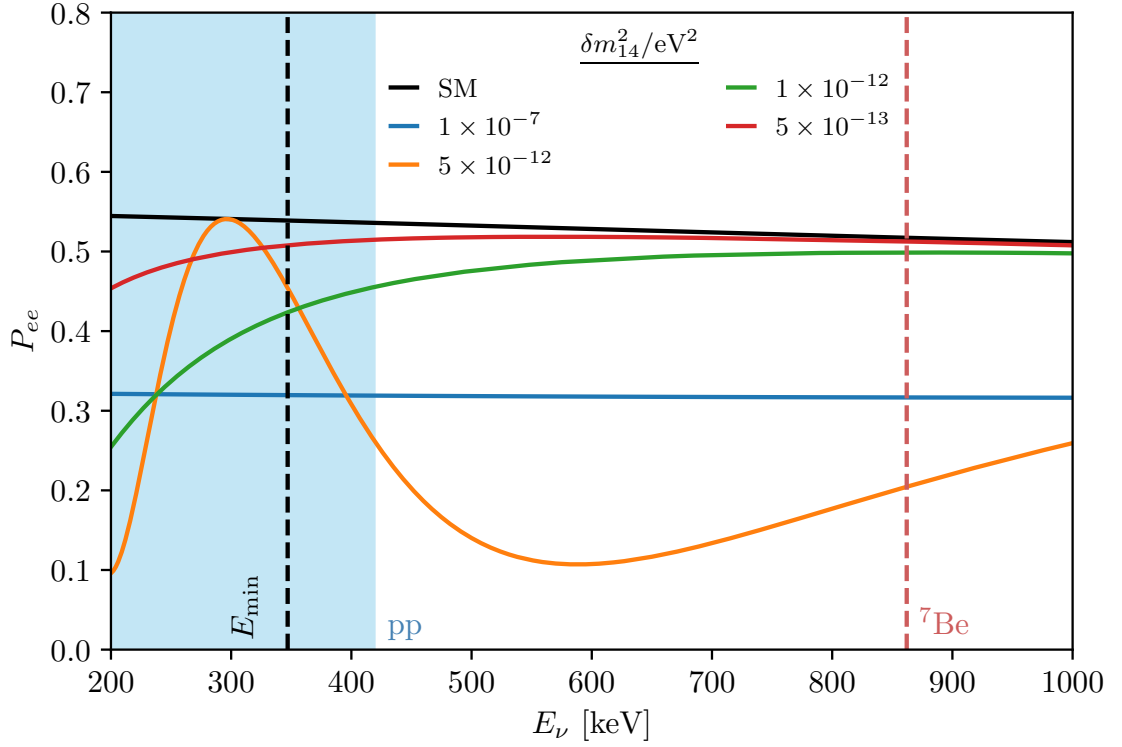


Figure 3.2: Numerical results for solar electron neutrino survival probability, P_{ee} , for the SM scenario (black solid curve) and for the 1-4 pseudo-Dirac pair scenario with maximal mixing ($\theta_{14} = \pi/4$). The coloured curves correspond to different possible values of the mass-squared splitting between the pseudo-Dirac pairs, as indicated in the legend. The light blue shaded region corresponds to the energies of pp neutrinos coming from the Sun, and the vertical red dashed line is the monochromatic energy of the high energy ${}^7\text{Be}$ neutrino line. The vertical black dashed line is the minimum neutrino energy given a cut in the recoil energy of 200 keV.

Equation (3.3.13) can be used to calculate the oscillation probabilities at the surface of the Sun. However, for small enough values of the mass splitting, we must consider the vacuum oscillations between the Sun and the Earth. This is because the production region is smaller than the typical oscillation length, and the decoherence length is larger than the distance between the Earth and the Sun, L_{ES} . On the other hand, Δm_{12}^2 and Δm_{13}^2 are sufficiently large that decoherence between these mass states occurs over distances much smaller than L_{ES} . This results in the neutrino mass states decohering into the three mass pairs, which we denote as 1-4, 2-5, and 3-6. We thus have to modify the amplitude at the edge of the Sun, \mathcal{A}_\odot , with two mass state vacuum oscillations.

$$\begin{aligned}
 (\mathcal{A}_E)_i &= (\mathcal{A}_\odot)_i, \\
 (\mathcal{A}_E)_{i+3} &= \exp\left(-i\frac{\delta m^2 L_{ES}}{2E_\nu}\right) (\mathcal{A}_\odot)_{i+3},
 \end{aligned}$$

where the index $i = 1, 2, 3$ denotes the mass state. From the amplitude at Earth, \mathcal{A}_E , we can determine the appearance probability of some flavour α to be:

$$\begin{aligned}
 P_{e\alpha} &= |U_{\alpha 1} (\mathcal{A}_E)_1 + U_{\alpha 4} (\mathcal{A}_E)_4|^2 \\
 &+ |U_{\alpha 2} (\mathcal{A}_E)_2 + U_{\alpha 5} (\mathcal{A}_E)_5|^2 \\
 &+ |U_{\alpha 3} (\mathcal{A}_E)_3 + U_{\alpha 6} (\mathcal{A}_E)_6|^2.
 \end{aligned} \tag{3.3.16}$$

This modified probability is then the input for the averaged probability used for our analysis. In Fig. 3.2, we show the solar electron neutrino survival probability in the 1-4 pair scenario. We observe that for a mass splitting of $\delta m_{14}^2 = 10^{-7} \text{ eV}^2$, the averaging of the probability results in a flat decrease in the survival probability and that the production region is large enough that there is little energy dependence on the probability. As the mass splitting decreases, this no longer is the case and the energy dependence of the probabilities becomes important, as can be seen for $\delta m_{14}^2 = 5 \times 10^{-12} \text{ eV}^2$. For even smaller mass splitting values, the survival probability slowly approaches the standard oscillations until they are indiscernible. This is

because the vacuum oscillation length becomes larger than the distance between the Earth and the Sun, so the modification to the standard oscillations probability approaches unity as the energy increases. The oscillation length is proportional to the neutrino energy, and so lower energy neutrinos can probe smaller mass splittings. This will set the limit on the lowest mass splitting that JUNO can probe.

3.4 Analysis

We aim to quantify JUNO's sensitivity to the pseudo-Dirac neutrino parameter space. To do this, we will calculate the probabilities of the active neutrinos arriving at the detector using the methods discussed in Section 3.3. Given the input parameters, the probabilities will give us the number of events we expect to see at the detector, N_{theory} , as is shown in Fig. 3.3. The overall effect of pseudo-Dirac oscillations is to reduce the electron neutrino survival probability at Earth since part of the neutrinos would oscillate to invisible sterile states. This is especially clear for the value of $\delta m_{14}^2 = 5 \times 10^{-12} \text{ eV}^2$, where we observe a deficit of $\sim 36\%$ with respect to the total expected events in the standard scenario. As these give the largest contribution to the cross-section, we can test the pseudo-Dirac scenarios by searching for a decrease in the number of detected neutrino scattering events compared to the SM theoretical expectation. The ability of the JUNO experiment to discriminate between the standard and pseudo-Dirac oscillation scenarios is given by the following test statistics,

$$\chi^2 = \sum_i \frac{\left(\sum_a \alpha_a N_{\text{theory}}^{i,a} + \sum_b (\alpha_b - 1) N^{i,b} - N_{\text{bench}}^i \right)^2}{N_{\text{bench}}^i + \sum_b N_b^i} + \sum_a \left(\frac{\alpha_a - 1}{\sigma_a} \right)^2 + \sum_b \left(\frac{\alpha_b - 1}{\sigma_b} \right)^2, \quad (3.4.1)$$

which compares the predicted events from the theory and the standard oscillation case. In Eq. (3.4.1), N^i is the total number of counts in the i th recoil energy bin from some source, given a target mass, M_{target} , and exposure time, t . The bin width is taken to be 25 keV, in accordance with the expected energy resolution of

JUNO of $3\%\sqrt{E_r/\text{MeV}}$ [29]. The index b runs over the backgrounds for the neutrino detection process, and N_{bench}^i is the benchmark neutrino event rate expected for the standard oscillation scenario, i.e. $N_{\text{bench}}^i = \sum_a N_{\text{SM}}^{i,a}$. The pull parameters α_i are free parameters that encode the measured events' statistical deviation from the theoretical expectation. For this analysis, we fix the standard oscillation parameters at their central values, using the NuFIT 5.2 global fit data [41], since JUNO is expected to measure independently the solar parameters θ_{12} and Δm_{12}^2 below the percent level using reactor antineutrinos [29].

The background rates are taken from detector simulations performed by the JUNO collaboration [29]. These simulations provide two possible scenarios for the reduction of backgrounds in the detector, the 'baseline' case and the 'ideal' case. As previously mentioned, the sources of backgrounds for the scintillation signal are from the detector's beta-decay processes of radioactive nuclei. For the ideal case, we consider ^{210}Bi , ^{85}Kr , and ^{238}U as the main backgrounds. These are also very relevant in the baseline case. However, it is also necessary to account for ^{40}K and ^{232}Th decay chains.

The pull parameters are given a weighting assuming a Gaussian prior with an error σ . For the neutrino sources, these errors correspond to the error in the theoretical flux calculations taken from standard solar model (SSM) simulations [40]: $\sigma_{\text{pp}} = 0.6\%$ and $\sigma_{\tau_{\text{Be}}} = 6\%$. We assume that the background counts can be constrained to a value of $\sigma_{\text{bkg}} = 1\%$, which we believe to be appropriate from the simulations of the backgrounds performed by the JUNO collaboration [29]. Minimising the test statistic over the pull parameters will give the projected sensitivity of JUNO to deviations from the standard oscillation scenario.

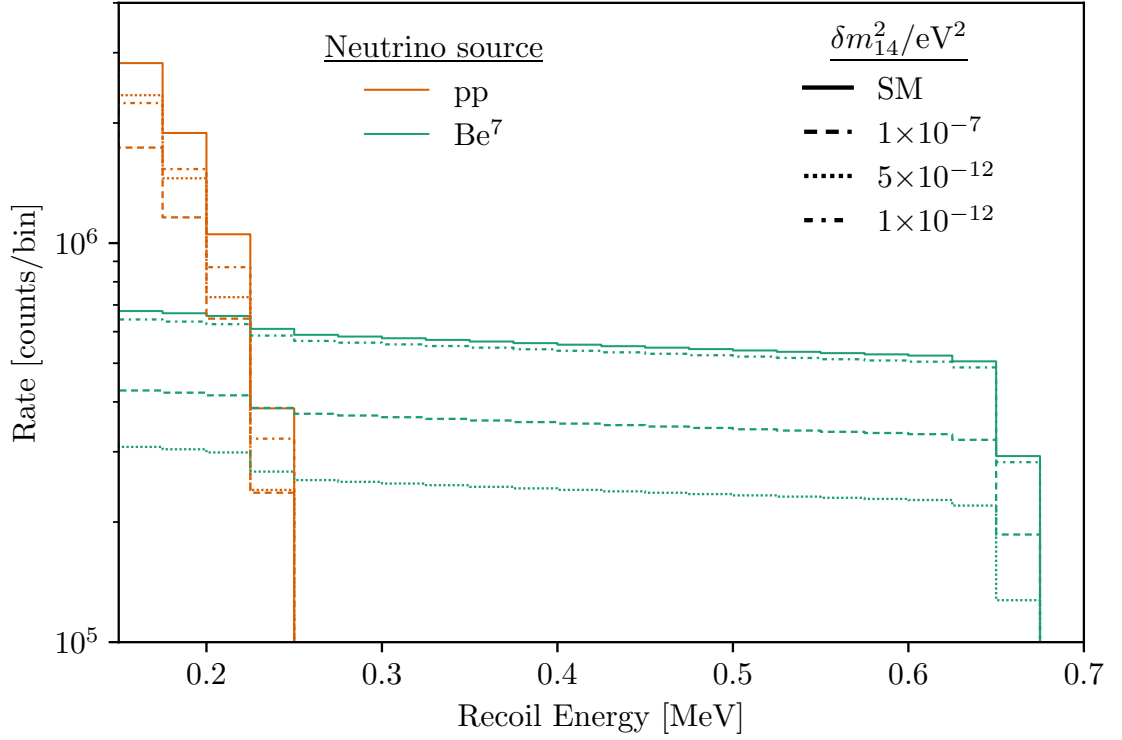


Figure 3.3: Expected event rates at JUNO for pp (orange) and Be^7 (green) solar neutrinos assuming a 6-year exposure time with 20 kilotonne fiducial mass. Here we show how a maximal mixing 1-4 pseudo-Dirac pair affects the event rate that JUNO will measure, for δm_{14}^2 values of 1×10^{-7} eV² (dashed), 5×10^{-12} eV² (dotted), 1×10^{-12} eV² (dash-dotted), and the SM case (solid). The data is shown with bin widths of 25 keV, as was used in our analysis, to demonstrate how JUNO can put limits on these values.

3.5 Constraints on the Possible Pseudo-Dirac

Nature of Neutrinos from JUNO

We simulate 6 years of exposure for JUNO, assuming a 20 kilotonne fiducial mass. All results are taken for the ‘ideal’ background case. However, the calculations were performed for the ‘baseline’ case and were found to be similar.

From Fig. 3.4 we observe that JUNO can place strong limits on the 1-4 mixing scenario, competing with the capability of the future DARWIN Xenon-based detector that was calculated in [36]. This is somewhat surprising since the absence of the ^{14}C background at DARWIN gives it access to much more of the pp neutrino spectrum, which gives stronger bounds on the mixing scenario since pp neutrinos have lower energy and a strongly constrained uncertainty. However, the large fiducial mass of JUNO, 20 kilotonnes as compared to DARWIN’s expected 300 tonnes, means that a large number of pp neutrinos could be detected if the cut at 200 keV in recoil energy is possible. As illustrated in Fig. 3.2, for mass splittings $\delta m_{14}^2 \leq 10^{-12} \text{ eV}^2$ the difference between the pseudo-Dirac and standard oscillations is much more pronounced for pp neutrino energies, compared to ^7Be neutrinos. This results in a significant difference between the detection rate for pp neutrinos. Furthermore, the theoretical constraints on the pp flux are much tighter than on the ^7Be flux, resulting in a stronger statistical significance on any deviation from the expected detection rate of pp neutrinos. This allows JUNO to place strong constraints on this scenario. If JUNO can achieve the intermediate cut (at 250 keV), it will be competitive with the constraints from Borexino. However, if the backgrounds are not sufficiently reduced, and the conservative cut is used, then JUNO would only be competitive with Borexino in the ^7Be neutrino sample, but since Borexino has measured pp neutrinos using a combined sample, it has marginally greater constraining power than JUNO in this scenario. If, on the other hand, JUNO can achieve the optimistic cut, then it would exceed the sensitivity of Borexino and be competitive with DARWIN.

We have also considered a maximal mixing angle $\theta = \pi/4$ and determined the

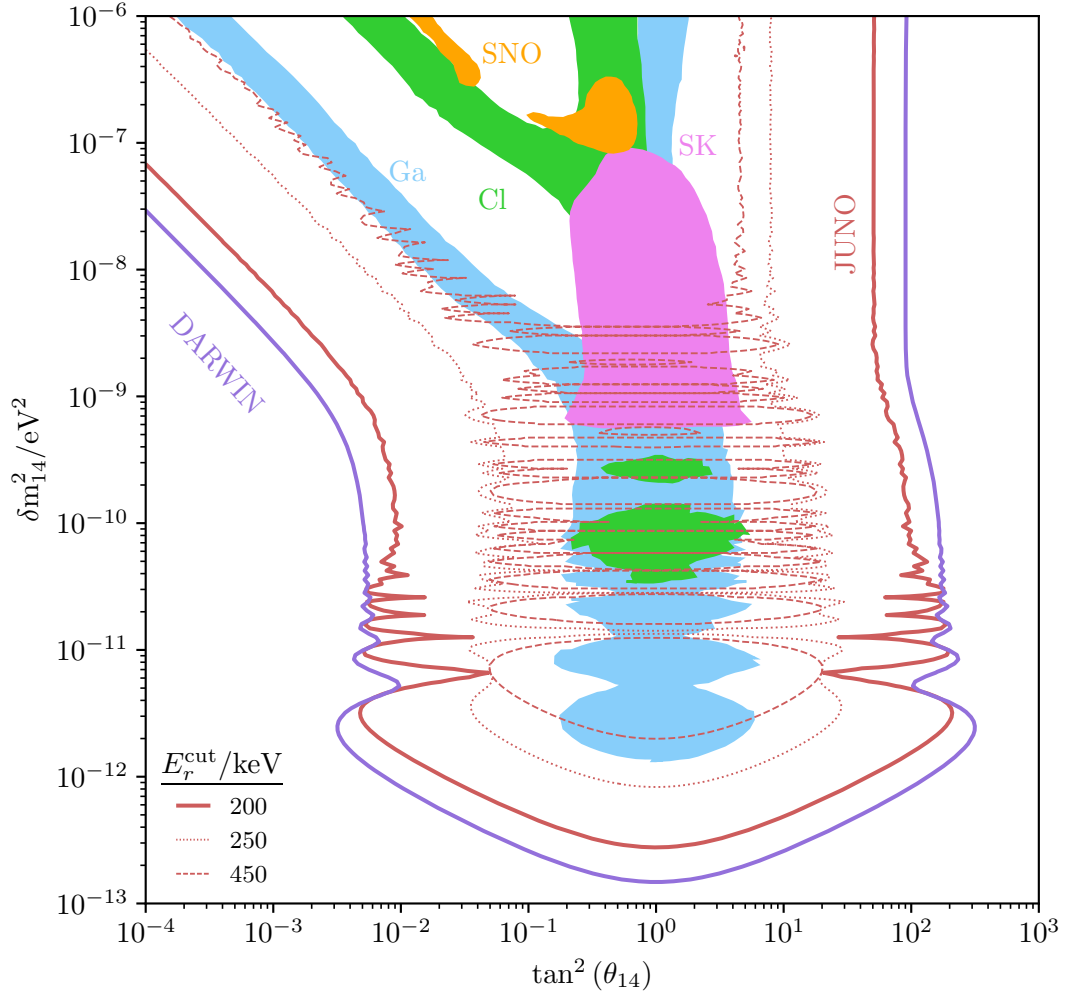


Figure 3.4: The 2σ sensitivity on the parameter space of 1-4 pseudo-Dirac pair oscillations at JUNO (red). These are shown for three values of the recoil energy cut: 200 keV (solid line), 250 keV (dotted line), and 450 keV (dashed line). Also shown are the projected limits that can be set by DARWIN [36] (purple), as well as the current limits (collected in Ref. [42]) from Gadolinium (Gd) [43], Super-Kamiokande [44] (SK), SNO [45] and Cl [46], [47] experiments.

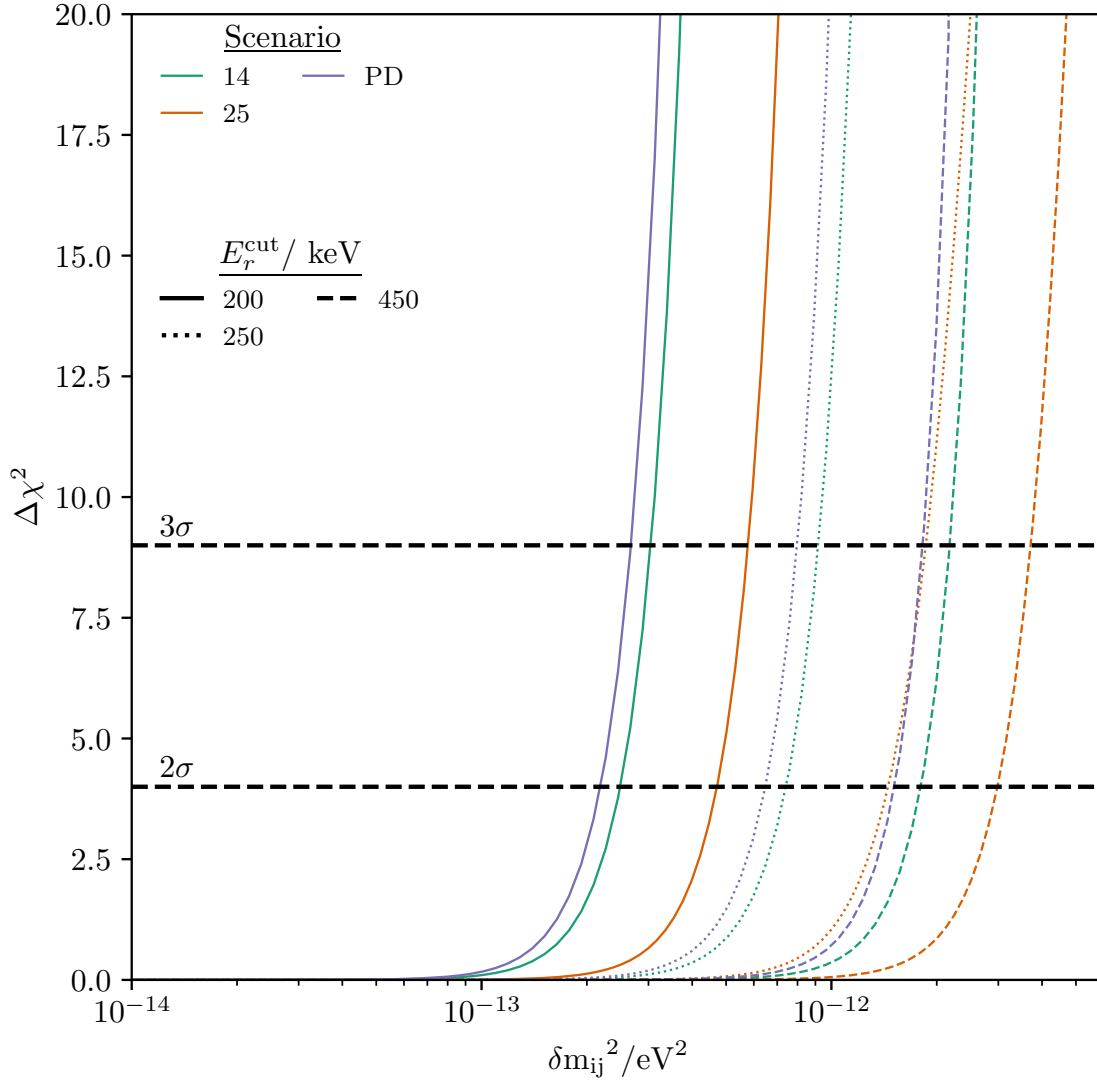


Figure 3.5: Marginalised χ^2 as a function of the mass splitting δm_{ij}^2 for various pseudo-Dirac scenarios at JUNO with maximal mixing $\theta_{ij} = \pi/4$. We consider here the 1-4 pair scenario (green), the 2-5 pair scenario (orange), and the full pseudo-Dirac (PD) scenario (purple) with three mass pairs, each with the same mass squared splitting. The sensitivity for each scenario is also displayed for the three recoil cuts of 200 keV (solid lines), 250 keV (dotted lines), and 450 keV (dashed lines)

constraints JUNO can place on the value of the mass splitting. We computed the sensitivities for the case of 1-4 and 2-5 mixing, as well as for the full pseudo-Dirac scenario assuming that each pair of mass states is split by the same amount, δm^2 . The results of this analysis are shown in Fig. 3.5. In the optimistic scenario we find that JUNO should be capable of excluding a mass splitting above $\sim 3.1 \times 10^{-13} \text{ eV}^2$ for the 1-4 scenario and $\sim 6 \times 10^{-13} \text{ eV}^2$ for the 2-5 scenario with a 3σ C.L. The disparity between the two arises because the electron flavour state has a larger component of the 1 - 4 mass state neutrinos than the 2 - 5, so it is more sensitive to the oscillations of the former pair. For the “full” pseudo-Dirac case, JUNO would be capable of excluding above $\delta m^2 \gtrsim 2.9 \times 10^{-13} \text{ eV}^2$, which is lower than either of the two individual cases. This occurs because all of the components of the electron neutrino can oscillate into sterile states, removing the limiting factor of the PMNS mixing and thus increasing the probability of a sterile state being at the detector.

JUNO will also be able to probe the δm_{25}^2 parameter space, which is important since there have been indications of a preference for a non-zero value of this parameter as in [48]. In particular, the preferred value of $\delta m^2 \sim 10^{-11} \text{ eV}^2$ is testable by JUNO; however, this assumes that the cut at 200 keV in recoil energy is feasible, as for higher cuts there is a dip in sensitivity at around this value. This is due to oscillation effects, where P_{ee} becomes the same as the SM for the higher energy ${}^7\text{Be}$ neutrinos. When pp neutrinos are included, these dips are removed since the measured flux is integrated over energy, and the minima are smeared out. The monochromatic nature of the ${}^7\text{Be}$ flux could be utilised in a seasonal variation analysis, as was done in [48] to search for pseudo-Dirac neutrinos. Due to the large number of these neutrinos that will be detected at JUNO, this could improve on the analysis already done and would be an interesting possibility to explore. We leave this for future work.

Future detectors such as DUNE or HK might improve the sensitivity due to their larger size in comparison to JUNO. However, their energy thresholds make them sensitive only to ${}^8\text{B}$ neutrinos, which have larger energies, and smaller fluxes, in comparison to pp and ${}^7\text{Be}$ as mentioned before. DUNE, for instance, has a 6 MeV

threshold for detecting neutrinos [49], while Hyper-K is limited due to the minimal energy that an electron needs to possess in order to emit Cherenkov radiation [50]. The mass splittings which can be tested with DUNE or Hyper-K are larger than the ones in JUNO and are of order $\delta m_{14}^2 = 10^{-7} \text{ eV}^2$. Thus, DUNE and HK could only improve the current SK sensitivity (pink region of Fig. 3.4). However, we can observe in the same figure that JUNO will be able to cover that region of the parameters, even in the conservative scenario.

Chapter 4

Constraining Neutrino

Self-Interactions with Point-Source

Fluxes at IceCube

Astrophysical processes can produce neutrinos across a broad range of energies. Whilst Solar neutrinos are produced with energies of $\mathcal{O}(100 \text{ keV})$ to $\mathcal{O}(10 \text{ MeV})$, neutrinos have been detected with energies well above the TeV range[51]. A significant contribution to the fluxes at these energies is believed to originate from high energy processes in galaxies. High energy neutrinos can be produced from the interactions of high energy protons with background matter, such as protons or photons. These interactions produce hadronic showers, including charged pions which subsequently decay into neutrinos[52]. Possible candidates of so called Cosmic accelerators which could produce protons with such extreme energies are Gamma Ray Bursts (GRB) and Active Galactic Nuclei (AGN).

However, the fluxes of these high energy neutrinos are very low in comparison to e.g. Solar neutrinos[53], so extremely large detectors are required to be able to detect them with statistical significance. The IceCube experiment[54], located at the South Pole, consists of photo-multiplier tubes (PMTs) instrumented throughout a cubic kilometre of Antarctic ice which is used as a detection medium. The interaction

between incoming high energy neutrinos and the ice produces charged leptons, as well as hadronic showers from the transfer of energy to the particle content of the ice. These charged particles will propagate through the ice and produce Cherenkov radiation, due to their high energies, which can be detected by the PMTs.

When the charged lepton produced from a CC interaction is a muon it is able to travel through the detector with minimal momentum transfer. At sufficiently high energies, the muon will travel over a distance greater than the separation of the PMTs. Its Cherenkov radiation can then be detected by multiple PMTs along its path of travel, which makes it possible to reconstruct the path and thus direction of the momentum of the muon. These are referred to as track events, due to their signature event topology in the detector. The direction of the produced muon will be correlated with the direction of the incident neutrino due to momentum conservation. This motivates the possibility of performing statistical inference to find locations in the sky which are associated with an increased neutrino flux.

Point-sources of neutrinos are galaxies which are known to produce gamma-ray fluxes, and whose location in the sky coincides with excesses in the neutrino flux[55]. They are point-like in the sense that the extent of the galaxy in the sky is smaller than the error in the reconstruction of the direction of the incident neutrino. A large experimental effort in searching for these sources of astrophysical neutrinos has led to the identification of a number of significant potential candidates. In particular, the IceCube collaboration recently made the announcement of the galaxy NGC 1068 being a point-like source of neutrinos at the 4.3σ confidence level[56].

The goal of this work is to investigate the possibility of exploiting point sources of astrophysical neutrinos to probe the behaviour and fundamental properties of neutrinos. We will focus on two possible BSM scenarios, firstly an overabundance of relic neutrinos assuming only SM interactions, and then additional interactions between neutrinos mediated by a new, light scalar particle. These scenarios can be probed by understanding that the neutrinos emitted by point sources are not travelling through a vacuum, but instead a background of neutrino relics from the

early Universe.

4.1 Cosmic Neutrino Background

Neutrinos in the early Universe were kept in thermal equilibrium, when the SM plasma temperature was $1 \text{ MeV} \lesssim T \lesssim 100 \text{ MeV}$, by the weak interactions with electrons, positrons, and the other neutrinos that existed in the SM plasma. The interaction rate can be expressed as

$$\Gamma = n \langle \sigma v \rangle , \quad (4.1.1)$$

where n is the number density of target particles, σ is the cross-section, and v is the neutrino velocity which was ≈ 1 (in natural units). As the SM plasma cooled due to the expansion of the Universe, the interaction rate decreased due to the reduction in the average centre-of-mass energy. In particular, thermally averaged cross section is of the order [17]

$$\langle \sigma v \rangle \sim G_F^2 T^2 \quad (4.1.2)$$

as the temperature is a measure of the average kinetic energy of particles in the thermal bath.

Eventually, the interaction rate became smaller than the Hubble expansion rate of the Universe, i.e. $\Gamma < H$. The temperature at which the neutrinos leave thermal equilibrium, known as the *freeze-out* temperature, is $T_{\text{fo}} \sim 1 \text{ MeV}$. After this point the evolution of their temperature became dominated by the redshift from expansion of the Universe[57]

$$T_\nu(z) = \frac{1+z}{1+z_{\text{fo}}} T_{\text{fo}} , \quad (4.1.3)$$

where z_{fp} is the redshift at freeze-out. The current temperature of the relic neutrinos can be calculated and is found to be[17]

$$T_\nu^0 = 1.676 \times 10^{-4} \text{ eV} . \quad (4.1.4)$$

These neutrinos, which we call relic neutrinos, have a current day number density which is found to be

$$n_0 \approx 56 \text{ cm}^{-3}, \quad (4.1.5)$$

per degree of freedom, giving a total of $\approx 360 \text{ cm}^{-3}$ after summing over all chiralities and flavours. At some earlier redshift, the number density is related to the current day value by

$$n_\nu(z) = n_0(1+z)^3, \quad (4.1.6)$$

as would be expected from the conservation of particle number.

The relic neutrinos have long since decohered from the superposition of mass states they were produced in [57]. Due to this, we will work in the mass basis when looking at the effect of interactions on neutrino fluxes from point sources.

4.1.1 Neutrino Degrees of Freedom

As the neutrinos are kept in thermal equilibrium with the SM plasma by weak interactions, we can assume that only left-chiral neutrinos existed in the early Universe. If neutrinos are Dirac in nature then we have four chiral degrees of freedom, but at z_{fo}

$$n[\nu](z_{\text{fo}}) = n_\nu(z_{\text{fo}}), \quad (4.1.7)$$

$$n[\nu^\dagger](z_{\text{fo}}) = n_\nu(z_{\text{fo}}), \quad (4.1.8)$$

$$n[\bar{\nu}](z_{\text{fo}}) = 0, \quad (4.1.9)$$

$$n[\hat{\nu}](z_{\text{fo}}) = 0. \quad (4.1.10)$$

However, the chirality of a particle is not conserved over time, as can be seen from the Dirac equation which couples left- and right- chiralities:

$$i\bar{\sigma}^\mu \partial_\mu \nu - m\bar{\nu} = 0, \quad (4.1.11)$$

$$i\bar{\sigma}^\mu \partial_\mu \bar{\nu} - m\nu = 0. \quad (4.1.12)$$

Assuming that there are three non-zero masses for the neutrinos (oscillation experiments tell us there must be at least two), we would expect to be able to find any of the neutrino mass states in either chirality. If the neutrinos are all relativistic, which will be the case for the two heaviest mass states, the time averaged densities are given by [58]

$$\bar{n}[\nu](0) = \frac{n_0}{2}, \quad (4.1.13)$$

$$\bar{n}[\nu^\dagger](0) = \frac{n_0}{2}, \quad (4.1.14)$$

$$\bar{n}[\bar{\nu}](0) = \frac{n_0}{2}, \quad (4.1.15)$$

$$\bar{n}[\hat{\nu}](0) = \frac{n_0}{2}. \quad (4.1.16)$$

On the other hand if neutrinos are given their mass via the dimension-5 Weinberg operator, as described in Section 2.3, and are thus Majorana in nature at low energies, they have only two chiral degrees of freedom. These are populated in the early Universe as

$$n[\nu](z_{\text{fo}}) = n_\nu(z_{\text{fo}}), \quad (4.1.17)$$

$$n[\nu^\dagger](z_{\text{fo}}) = n_\nu(z_{\text{fo}}), \quad (4.1.18)$$

and at present day

$$n[\nu](0) = n_0, \quad (4.1.19)$$

$$n[\nu^\dagger](0) = n_0, \quad (4.1.20)$$

i.e. they have twice the detectable relic density today than in the Dirac case. We will specify our assumptions on the nature of the neutrino mass when relevant in later sections.

4.2 Propagation of Neutrino Fluxes

To take into account the effect of scattering with relic neutrinos on the neutrino flux propagating to the Earth, it is necessary to solve a transport equation for the flux of neutrinos with mass state i [59], [60],

$$\begin{aligned} \frac{\partial \Phi_i(t, E)}{\partial t} = & \frac{d}{dE_\nu} [H(t) E_\nu \Phi(t, E)] - \Phi_i(t, E) \sum_j n_j \sigma_{ij}(E) \\ & + \sum_{j,k,l} n_k \int_E^\infty dE' \Phi_j(t, E') \frac{d\sigma_{jk \rightarrow il}(E', E)}{dE}, \end{aligned} \quad (4.2.1)$$

where Φ_i denotes the combined flux of neutrinos and anti-neutrinos with mass state i , and t is the time since the neutrinos were emitted. The first term, containing the Hubble expansion rate $H(t)$, accounts for the energy loss of neutrinos due to the redshift from the expansion of the Universe. The second term is the loss term, which reduces the flux at a particular value of energy according to the interaction rate with the C ν B, given by the product of n_j , the number density of mass states j , and σ , the neutrino-neutrino cross-section. In the third term of Eq. (4.2.1), the j state is the incoming neutrino with energy E' , the k state is the relic neutrino, i is the outgoing neutrino with the mass state of interest, and l is the other neutrino state produced in the interaction. This term distributes the flux from down-scattering (energy loss of the neutrinos) and up-scattering of the relic neutrino. We solve this differential equation numerically, using a similar method to that in [59].

The centre-of-mass energy of the interaction of the astrophysical neutrino, with energy E , with the relic neutrino of mass m_j , assumed to be at rest¹, is

$$\sqrt{s_j} = \sqrt{2m_j E} \sim 1.41 \text{ MeV} \left(\frac{m_j}{0.1 \text{ eV}} \right)^{1/2} \left(\frac{E}{10 \text{ TeV}} \right)^{1/2}.$$

We parametrise the initial fluxes of neutrinos from the point sources with a power-law (PL) flux, where the flux is parameterised in terms of a normalisation Φ_0 , at

¹Note that large overdensities due to some BSM interactions might also imply that the relic neutrinos could be relativistic today, enhancing the centre-of-mass energy. However, we refrain from considering such a scenario to keep our discussion as model-independent as possible.

reference energy E_0 , and a spectral index γ such that

$$\Phi(t = 0, E_\nu) = \Phi_0 \left(\frac{E_\nu}{E_0} \right)^{-\gamma}. \quad (4.2.2)$$

We take $E_0 = 1$ TeV throughout this work. For each source, we assume the fluxes are independent and uncorrelated. We also assume that the neutrinos are produced from the decay of charged pions,

$$\pi^+ \rightarrow \mu^+ + \nu_\mu^\dagger \rightarrow e^+ + \nu_e^\dagger + \nu_\mu + \nu_\mu^\dagger$$

which results in the initial flavour ratio of 1:2:0 for $\nu_e:\nu_\mu:\nu_\tau$.

4.3 Numerically Solving The Neutrino Transport Equation

We are able to solve Eq. (4.2.1) numerically, which allows us to find the neutrino flux at Earth taking into account both the scattering with the CνB and redshift due to the expansion of the Universe. For galaxies that are close enough to our own, we ignore the negligible redshift effects and solve the propagation as a function of distance. The method outlined in this section is generic in the specific model of interactions, so detailed descriptions of e.g. cross sections will be left until later.

4.3.1 Upper And Lower Bounds On Neutrino Energy

Before describing the details of the numerical method, we will explain the bounds of the neutrino energy integral in the third term of Eq. (4.2.1). The lower bound, somewhat trivially, is the lowest energy of neutrinos that can be detected by IceCube, which we take to be $E_{\min} = 100$ GeV. We can do this because, as seen from the integral in Eq. (4.2.1), the flux at a specific energy depends only on the flux at higher energies. This results in the neutrinos “flowing down” in energy. As such, there is

no dependence on undetectable neutrinos.

The upper bound on the neutrino energy is infinity (as we are assuming a power-law flux); however, when solving this integral numerically, we need a finite upper bound which will approximate the integral well. To find a value for the finite upper bound, it is useful to look at the integral of the initial power-law flux from this lower bound up to some energy cutoff E :

$$I(E) = \int_{100 \text{ GeV}}^E \Phi(0, E') dE' = \frac{\Phi_0}{1 - \gamma} \frac{1}{E_0^{-\gamma}} \left(E^{-\gamma+1} - (100 \text{ GeV})^{-\gamma+1} \right), \quad (4.3.1)$$

where the initial flux is a power law:

$$\Phi(0, E) = \Phi_0 \left(\frac{E}{E_0} \right)^{-\gamma}, \quad (4.3.2)$$

and we have assumed that $\gamma > 1$ to ensure that the integral converges when $E \rightarrow \infty$.

The fraction of the total flux above the cutoff is then given by:

$$f(E) = 1 - \frac{I(E)}{I(\infty)} = \left(\frac{E}{10^2 \text{ GeV}} \right)^{-\gamma+1}. \quad (4.3.3)$$

Since the total flux above our cutoff energy is always greater than or equal to the scattered flux above the cutoff energy, this fraction is then an upper bound on the error in the approximation of the integral in Eq. (4.2.1). If we want the fraction of the total flux above our cutoff to be smaller than some ϵ , we can find the corresponding cutoff E_{max} from rearranging Eq. (4.3.3). This gives the relation:

$$\log_{10} \left(\frac{E_{\text{max}}}{1 \text{ GeV}} \right) = 2 + \frac{\log_{10}(\epsilon)}{\gamma - 1}. \quad (4.3.4)$$

For example, if we want to limit the flux ignored to $\epsilon = 10^{-6}$ we require $E_{\text{max}} = 10^8$ GeV assuming $\gamma = 2$. In practice, we take a fixed value of $E_{\text{max}} = 10^{10}$ GeV, which

satisfies $\epsilon \leq 10^{-6}$ for $\gamma \geq 1.5$.

4.3.2 Solving The Transport Equation Without Redshift

There are two cases in which we need to solve the transport equation; for closer sources where redshift effects can be ignored, and for further sources where the redshift effects need to be accounted for. The former of these is a simpler case, and so we will first describe the discretisation and solving of the equation before adapting the algorithm for the latter case.

To ignore the effect of redshift, we can set the energy loss term in Eq. (4.2.1) to zero. We can also use the fact that the neutrinos are relativistic and change variables from time t to distance r . We then get:

$$\frac{\partial \Phi_i(r, E)}{\partial r} = -\Phi_i(r, E) \sum_j n_j \sigma_{ij}(E) + \sum_{j,k,l} n_k \int_E^\infty dE' \Phi_j(r, E') \frac{d\sigma_{jk \rightarrow il}(E', E)}{dE} \quad (4.3.5)$$

This can be written more efficiently by assuming that all neutrino mass states have the same relic density, i.e. $n_i = n_\nu \forall i \in \{1, 2, 3\}$, and repackaging the sums over integrated and differential cross-sections.

$$\frac{1}{n} \frac{\partial \Phi_i(r, E)}{\partial r} = -\Phi_i(r, E) K_i(E) + \sum_j \int_E^\infty dE' \Phi_j(r, E') J_{ji}(E, E') \quad (4.3.6)$$

where the function K_i contains the cross-sections for incoming neutrino with mass m_i , and the kernel function J_{ji} contains the differential cross-sections for the incoming neutrino with mass j and outgoing neutrino with mass state i . The sum over k and l has been moved inside of J_{ji} . To discretise the flux over energy, we project the differential equation onto a set of basis functions given by

$$\left\{ \Theta(E - E_{n-1/2}) \Theta(E_{n+1/2} - E) \mid n < N, n, N \in \mathbb{N} \right\},$$

where $\Theta(x)$ is the Heaviside step function and N is the number of basis functions.

This improves the numerical stability of the solution when there are discontinuities, such as those in the cross-sections which arise from e^+e^- production, compared to a finite-difference based discretisation. We also approximate the flux as a linear combination of these basis functions. In our implementation, we space the bins logarithmically and take the total number of bins N as 300. We then integrate the differential equation over energy to obtain N coupled equations:

$$\frac{\Delta E_n}{n_\nu} \frac{\partial \Phi_i^n(r)}{\partial r} = -\Phi_i^n(r) K_i^n + \sum_j \sum_m \Phi_j^m J_{ji}^{mn}, \quad (4.3.7)$$

where we have defined:

$$\Phi_i^n(r) = \frac{1}{\Delta E_n} \int_{E_{n-1/2}}^{E_{n+1/2}} dE \Phi(r, E) \quad (4.3.8)$$

$$K_i^n = \int_{E_{n-1/2}}^{E_{n+1/2}} dE K_i(r, E) \quad (4.3.9)$$

$$J_{ji}^{mn} = \begin{cases} \int_{E_{n-1/2}}^{E_{n+1/2}} dE \int_{E_{m-1/2}}^{E_{m+1/2}} dE' J_{ji}(E, E') & \text{if } m > n, \\ \int_{E_{n-1/2}}^{E_{n+1/2}} dE \int_E^{E_{m+1/2}} dE' J_{ji}(E, E') & \text{if } m = n, \\ 0 & \text{if } m < n, \end{cases} \quad (4.3.10)$$

$$\Delta E_m = E_{m+1/2} - E_{m-1/2}. \quad (4.3.11)$$

There are three possible values of J_{ji}^{mn} , each corresponding to different cases. First, we have that the m th energy bin is higher than the n th (or equivalently $m > n$). In this case we can integrate over both energy limits independently. In the second case however, we have $m = n$ which implies that the energy bins are the same. Since the initial energy E' must be greater than the final energy E , the lower energy limit in the second integral is E rather than $E_{m-1/2}$. Finally, we have the case of $m < n$ which is not possible as the energy must decrease, resulting in a value of zero. We calculate the integrals of K_i^n and J_{ji}^{mn} analytically, which reduces the time needed

to solve the equation.

We now discretise the distance r , following an implicit finite-difference scheme. This amounts to the substitutions:

$$\frac{\partial \Phi_i^n(r)}{\partial r} \rightarrow \frac{\Phi_i^n(r_{a+1}) - \Phi_i^n(r_a)}{\Delta r} \quad (4.3.12)$$

$$\Phi_i^n(r) \rightarrow \Phi_i^n(r_{a+1}) \quad (4.3.13)$$

Since K and J are not functions of r , this discretisation does not affect them. Performing these substitutions in Eq. (4.3.7) gives:

$$\frac{\Delta E_n}{n_\nu} \frac{\Phi_i^n(r_{a+1}) - \Phi_i^n(r_a)}{\Delta r} = -\Phi_i^n(r_{a+1}) K_i^n + \sum_j \sum_m \Phi_i^m(r_{a+1}) J_{ji}^{mn}. \quad (4.3.14)$$

We now have a fully discretised form of Eq. (4.2.1), which we need to solve starting from our initial power-law flux.

To solve these equations, we follow a similar method to that used in [59]. We rewrite Eq. (4.3.14) as a matrix equation over the i and j indices:

$$M_{ji} x_j = \frac{x'_i}{\Delta r} - \frac{n_\nu y_i}{\Delta E_n}, \quad (4.3.15)$$

where

$$x_i = \Phi_i^n(r_{a+1}) \quad (4.3.16)$$

$$x'_i = \Phi_i^n(r_a) \quad (4.3.17)$$

$$y_i = \sum_{m>n} \sum_j \Phi_i^m(r_{a+1}) J_{ji}^{mn} \quad (4.3.18)$$

$$M_{ji} = \left(\frac{1}{\Delta r} + \frac{n_\nu}{\Delta E_n} K_i^n \right) \delta_{ij} - n_\nu J_{ji}^{nn} \quad (4.3.19)$$

Since each equation for n depends only on the solutions of equations $m > n$, we can solve the whole system by starting at $n = N$ and propagate the solutions down to $n = 0$. This way, the only unknowns are the values x_j , which can be solved for using standard linear algebra techniques.

One final step is to introduce a lower bound value for the flux in a bin, below which it is set to zero. Doing so reduces noise and improves the stability of the solution dramatically. The cutoff value was found by trial and error not to lose any useful information about the flux. We found that a value of $\Phi_{\min} = 10^{-30} \Phi_0$ was sufficient, as it provided a stable solution without removing a significant amount of flux. Since the output of the numerical solver will be used to calculate a probability density function (pdf), the normalisation Φ_0 does not matter, so we set it to be 1.

4.3.3 Solving The Transport Equation With Redshift

Solving the transport equation whilst taking into account redshift can be done in a similar method to the one previously described, with some modifications.

Firstly, we wish to solve the flux as a function of the redshift z , using the substitution $\partial_t = H(z)(1+z)\partial_z$. Note that the definition of energy in the interaction is in the local frame of reference, i.e. $E_{\text{local}} = (1+z)E_{\text{observed}}$. In Eq. (4.2.1), this fact is taken into account by the first term, however in our discretised equation we can instead choose the energy bins such that we can make the substitution

$$\Phi_i^n(z_a) \rightarrow \left(\frac{1+z_a}{1+z_{a+1}} \right)^{-3} \Phi_i^{n+1}(z_a). \quad (4.3.20)$$

This means that the effect of redshift on the energy will shift the bins down by one for each step in redshift, and to also dilute the flux due to the expansion of the Universe. In order for the former to be the case, we have the following relation:

$$-\log_{10} \left(\frac{1+z_{a+1}}{1+z_a} \right) = \Delta \log_{10} E, \quad (4.3.21)$$

where the minus sign is needed due to the value of z starting at some $z_{\max} > 0$ and decreasing monotonically to $z = 0$ as the neutrinos propagate, i.e. $z_{a+1} < z_a$. The values of z for which we solve can then be defined iteratively:

$$z_{a+1} = \frac{1 + z_a}{\exp(\Delta \log_{10} E)} - 1. \quad (4.3.22)$$

To find the number of steps in z needed, we use the fact that

$$1 + z_{\max} = \prod_{a=0}^{N_z-1} \frac{1 + z_a}{1 + z_{a+1}}, \quad (4.3.23)$$

which gives

$$N_z = \frac{\log_{10}(1 + z_{\max})}{\Delta \log_{10} E}. \quad (4.3.24)$$

Following this procedure will properly account for the effect of redshift on the flux as it propagates through the expanding Universe to Earth [61].

There is one additional effect which differs when taking redshift into account, which is the fact that the relic density of neutrinos will also decrease as the redshift decreases. This is easily included by promoting n_ν to a function of z , writing it in terms of the current neutrino density:

$$n_\nu(z) = (1 + z_{a+1})^3 n_\nu(1). \quad (4.3.25)$$

Combining all these effects with the energy discretisation outlined in the previous section, leaves us with the following matrix equation:

$$\mathbf{M}_{ji} \Phi_j^n(z_{a+1}) = \frac{H(z)(1 + z_{a+1})}{z_a - z_{a+1}} \left(\frac{1 + z_a}{1 + z_{a+1}} \right)^{-3} \Phi_i^{n+1}(z_a) - \frac{n_\nu(z)}{\Delta E_n} y_i, \quad (4.3.26)$$

where

$$y_i = \sum_{m>n} \sum_j \Phi_j^m(z_{a+1}) J_{ji}^{mn}, \quad (4.3.27)$$

and

$$M_{ji} = \left(\frac{H(z)(1 + z_{a+1})}{z_a - z_{a+1}} + \frac{n_\nu(z)}{\Delta E_n} K_i^n \right) \delta_{ij} - n_\nu(z) J_{ji}^{nm}. \quad (4.3.28)$$

This system of equations can be solved using the same method as previously described.

4.4 Analysis Methodology

To search for signals of neutrino self-interactions - from both overdensities and non-standard interactions (NSI) - within the IceCube data, we perform an unbinned maximum likelihood test using the SkyLLH python package [62]–[64]. The likelihood function for N events, with a source flux determined by a set of model parameters $\boldsymbol{\theta}$, is

$$\mathcal{L}(n_s, \boldsymbol{\theta} | \mathbf{x}, N) = \prod_{i=1}^N \left(\frac{n_s}{N} f_S(\mathbf{x}_i | \boldsymbol{\theta}) + \left(1 - \frac{n_s}{N} \right) f_B(\mathbf{x}_i) \right), \quad (4.4.1)$$

where \mathbf{x}_i are the observables of the event i , n_s is the number of events associated with the signal, and f_S and f_B are the signal and background pdfs, respectively. When performing the analysis, we consider the events from 2012-2018 taken from the public release [65], and select those within a 15° radius from each source.

To perform a statistical test for a choice of parameters in a given model, we compare the likelihood to that of the null hypothesis, which we take to be the best fit power law flux for the chosen source. We use a log-likelihood ratio as our test-statistic:

$$TS = -2\Delta \log \mathcal{L} = -2 \log \left(\frac{\mathcal{L}(n_s, \boldsymbol{\theta} | \mathbf{x}_i, N)}{\mathcal{L}_0} \right), \quad (4.4.2)$$

where we denote the likelihood of the best-fit power law flux hypothesis as \mathcal{L}_0 . The

Source	Number of events (n_s)	Spectral index (γ)
NGC 1068	56.5	3.15
PKS 1424+24	48.7	3.86
TXS 0506+056	14.5	2.17

Table 4.1: The best-fit values of the signal event normalisation (n_s) and the spectral index (γ) for each of the three sources included in the analysis, assuming SM interactions and no overdensity in the relic neutrino flux.

relevant model parameters for the power-law hypothesis are the spectral index γ , and the location of the source in the sky θ_s . We take fixed values of θ_s according to the source under consideration. For the overdensity hypothesis we also have the parameter η , which is the ratio compared to the SM relic neutrino density. When modeling the NSI flux, we fix $\eta = 1$ and instead have the mass of the scalar mediator M_ϕ and the coupling between tau neutrinos $g_{\tau\tau}$ as the free model parameters. For the two latter cases, we may also allow the mass of the lightest neutrino to vary - the other two masses are derived from this value using measured mass splitting values from NuFIT 2022 [41].

For each realisation of the BSM model parameters (η or $(M_\phi, g_{\tau\tau})$), we minimise the test statistic (TS) over the spectral index of the initial flux, γ , and the number of signal events n_s . The likelihood of the null hypothesis (\mathcal{L}_0) corresponds to the absence of observable signals of neutrino interactions - the scenario where the $C\nu B$ density follows the prediction of the Λ CDM model or where there are no BSM self-interactions - and the neutrino flux is described by the best-fit parameters given in Table 4.1.

These values are obtained through a TS analysis comparing the likelihoods between the power-law model and the scenario where all the data corresponds to the background.

To perform this analysis, it is necessary to solve Eq. (4.2.1) for the given model parameters. This results in the flux of neutrinos at IceCube, which can then be used to calculate the signal pdf.

4.4.1 Future Sensitivities

In order to estimate the sensitivity of the analysis technique in the light of future data, it is necessary to produce mock data on which the analysis can be performed. We do this on a per source basis, on account of the sources being sufficiently separated in the sky that there is minimal probability that an event originating from one source will be within the angular cut taken for the analysis of another source. We also assume that all of the systematics of the IceCube detector will remain the same, which is a decision driven by necessity rather than realism. The creation of mock data can be performed by SkyLLH, using the constructed pdf of the background and a given source pdf. For the latter, we assume the source follows the best-fit power law flux. Once a set of mock data is generated, it is combined with the current data set and the analysis is performed. This process is repeated over a number of different instances, and the expectation value of the test-statistic is approximated as the mean value of TS over all instances of mock data. We found, through a process of trial-and-error, that a set of 500 instances produced reliable values.

4.5 Relic Overdensity

Any deviation from the expected average number density of relic neutrinos, $n_0 \approx 56 \text{ cm}^{-3}$, can be parameterised by $\eta = n/n_0$, where n is the actual number density.

The final flux at Earth can be found by solving the transport equation of Eq. (4.2.1) numerically over the distance that the neutrinos travel through the overdense region, which we take to be the entire distance of their propagation between their source and Earth, assuming a given overdensity η .

The effect of neutrino self-interactions over the astrophysical neutrino flux can be seen in Fig. 4.2. Taking NGC 1068 as an example, the initial flux is plotted alongside the final flux for several different relic neutrino densities. The main effect is a suppression of the flux at high energies. Regeneration processes lead to an increased flux at lower

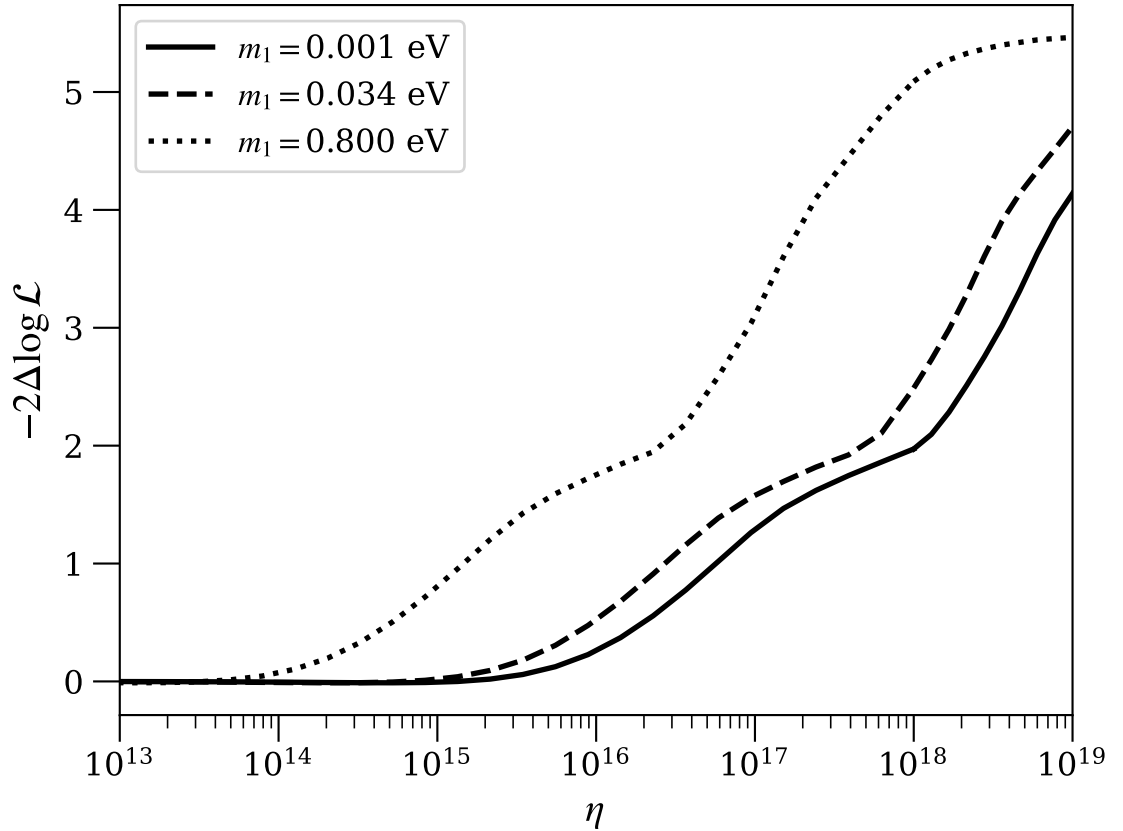


Figure 4.1: The t-statistic $-2\Delta\log\mathcal{L}$ for NGC 1068 as a function of the relic neutrino overabundance. The effect of the value of m_1 is also demonstrated by taking different limits for the mass scale, as explained in the text. Here we take $d_{\text{eff}} = 14$ Mpc for the radius of the overdense region.

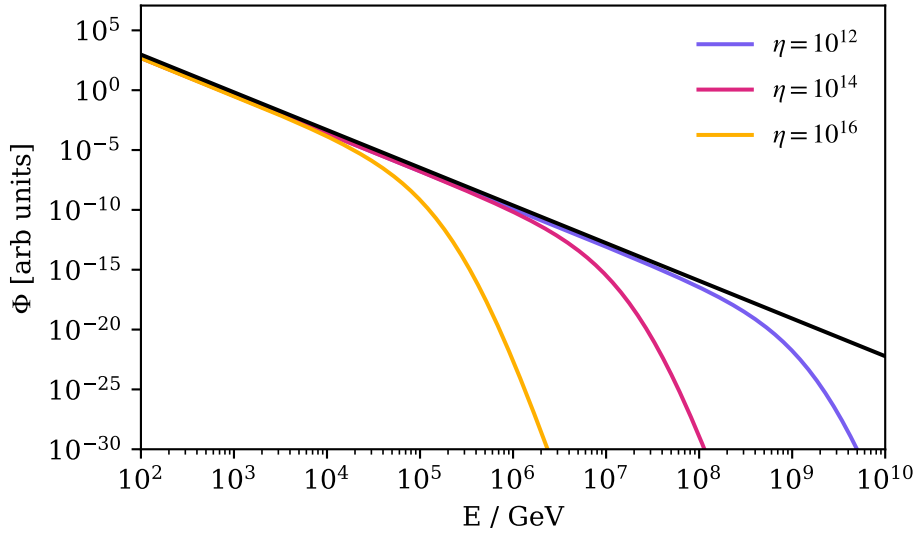


Figure 4.2: Normalised muon neutrino fluxes from NGC 1068 at IceCube under different scenarios. The black line is the initial flux, taken to be a power law. The spectral index of the initial flux is the best-fit values from our TS analysis, $\gamma = 3.15$. Given this initial flux, the other lines are the solutions to the transport equation, with the relevant neutrino number density ratios indicated. The number density is assumed to be constant over the distance between NGC 1068 and Earth, and m_1 (the lightest neutrino mass) is 0.034 eV . Flux given in arbitrary units as the normalisation is a priori unknown.

energies; however, the influence at lower energies remains minimal due to the rapid decrease of the flux with energy.

We begin our discussion by considering only SM neutrino interactions, and assume that the number density is the same for all mass states and neutrinos/antineutrinos. We require both total and differential SM cross-sections to solve the transport equations in Eq. (4.2.1), which we will briefly outline next. For the observable neutrinos under consideration, which have energy $\lesssim 100 \text{ TeV}$, the centre of mass energy of the interactions (see Section 4.2) are always sufficiently small that the only important processes are $\nu\nu \rightarrow \nu\nu$, $\nu\bar{\nu} \rightarrow \nu\bar{\nu}$, and $\nu\bar{\nu} \rightarrow e^+e^-$.

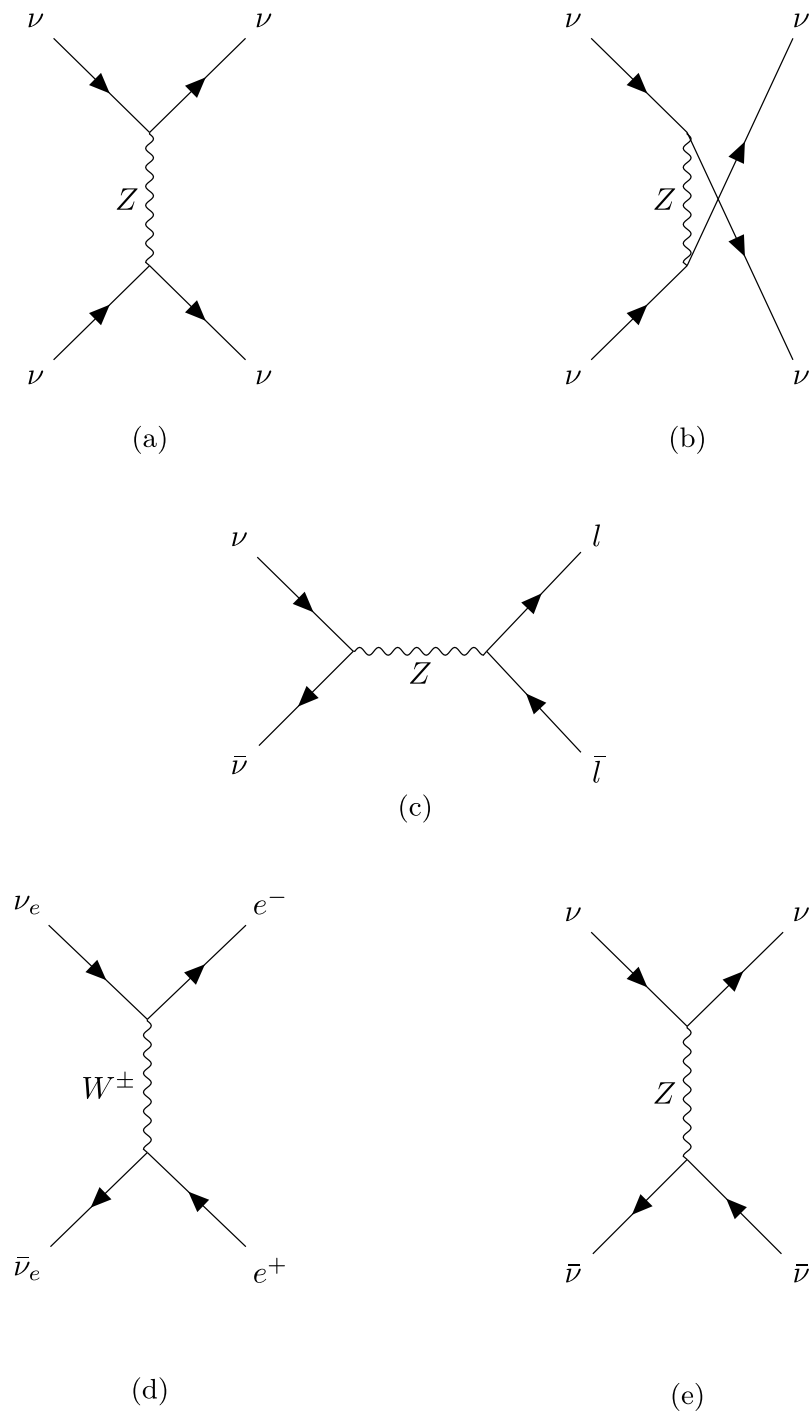


Figure 4.3: Feynman diagrams for the relevant interactions between neutrinos and relic neutrinos. (a) and (b) are the t - and u -channel diagrams, respectively, for elastic scattering of incident neutrinos off of relic neutrinos. (c) is for lepton pair production where $l = \nu$ or $l = e^-$. (d) is the t -channel e^+e^- pair production diagram. (e) is the t -channel elastic scattering of neutrinos on relic anti-neutrinos.

4.5.1 Total cross-sections

We assume that all particles in the incoming flux are neutrinos rather than antineutrinos. This is valid as the flux observed at IceCube is a combination of ν_μ and $\bar{\nu}_\mu$ fluxes, and the total cross-section is invariant under swapping $\nu \leftrightarrow \bar{\nu}$.

We start with the $\nu\nu \rightarrow \nu\nu$ scattering. Since the Z -boson mediates this process, it is convenient to work in the neutrino mass basis. The total cross-section is:

$$\sigma_{ij} = \frac{G_F^2 s_j (3\delta_{ij} + 1)}{2\pi}, \quad (4.5.1)$$

where G_F is Fermi's constant and the $3\delta_{ij}$ occurs because of the interference between t and u -channel diagrams, as shown in Fig. 4.3a and Fig. 4.3b respectively, which occurs when $i = j$. In the case of $\nu\bar{\nu}$ scattering, we separate the cross-section calculation into two categories - $\nu\bar{\nu}$ and e^+e^- production. The first of these follows similarly to the previous case, in particular when $i \neq j$:

$$\sigma_{ij} = \frac{G_F^2 s_i}{6\pi}, \quad (4.5.2)$$

while for $i = j$, we have to account for the annihilation and production of new neutrino pairs. Combined, this gives:

$$\sigma_{ii} = \frac{G_F^2 s_j}{\pi} \left(\frac{2}{3} + 2 \times \frac{1}{6} \right) = \frac{G_F^2 s_j}{\pi}, \quad (4.5.3)$$

where the first term arises from production of a $\nu_i\bar{\nu}_i$ pair, which receives an enhancement from the additional t -channel diagram as shown in Fig. 4.3e. The second term is from the production of a k state mass pair, where $i \neq k$, of which there are two possibilities.

For the electron pair production process, the cross-section must be calculated on

a weak basis. We write the mass-basis cross-section in terms of the weak basis cross-section using the PMNS matrix:

$$\sigma_{ij} = \sum_{\alpha,\beta} |U_{i\alpha}|^2 |U_{j\beta}|^2 \sigma_{\alpha\beta}. \quad (4.5.4)$$

$$\sigma_{\alpha\alpha} = \frac{G_F^2}{3\pi} \sqrt{1 - \frac{4m_e^2}{s}} \left(2m_e^2 (g_{V,\alpha}^2 - 2g_{A,\alpha}^2) + s (g_{A,\alpha}^2 + g_{V,\alpha}^2) \right) \quad (4.5.5)$$

where the flavour dependent axial and vector couplings are $g_{A,\alpha} = \delta_{\alpha e} - \frac{1}{2}$ and $g_{V,\alpha} = \delta_{\alpha e} - \frac{1}{2} + 2 \sin^2 \theta_W$ respectively.

The total cross-section for the SM interactions between the high-energy neutrinos flux from astrophysical sources and relic neutrinos can be split into two contributions: one from the production of neutrino final states only and one from the production of electron-positron pairs:

$$\sigma_{ij} = \sigma_{ij}^\nu + \sigma_{ij}^e, \quad (4.5.6)$$

where i is the incoming neutrino mass state, and j is the relic neutrino mass state, as before. From this, we find that

$$\sigma_{ij}^\nu = \frac{G_F^2 (7\delta_{ij} + 2) s_j}{3\pi}, \quad (4.5.7)$$

where G_F is the Fermi constant. This cross-section has been summed over the contributions from relic neutrinos and antineutrinos. For the cross-section with e^+e^- final states, the interaction must be calculated in the mass basis, such that

$$\sigma_{ij}^e = \sum_{\alpha} |U_{ei}|^2 |U_{ej}|^2 \sigma_{\alpha}^e, \quad (4.5.8)$$

where α is the flavour of the initial state neutrinos in the interaction. The production of e^+e^- only occurs with neutrino-antineutrino annihilation, so we can consider the initial flavours to be identical. The total cross-sections for this process are

$$\sigma_\alpha^e = \frac{G_F^2}{3\pi} [s(g_A^2 + g_V^2) + 2m_e^2(g_V^2 - 2g_A^2)] \sqrt{1 - \frac{4m_e^2}{s}}, \quad (4.5.9)$$

where $g_A = \delta_{\alpha e} + g_A^\alpha$ and $g_V = \delta_{\alpha e} + g_V^\alpha$ where $g_A^\alpha = -\frac{1}{2}$ and $g_V^\alpha = -\frac{1}{2} + 2\sin^2\theta_W$, with θ_W being the weak mixing angle and m_e the electron mass.

4.5.2 Differential cross-sections

For the process $\nu_j\nu_k \rightarrow \nu_i\nu_l$ we find that:

$$\frac{d\sigma_{jk \rightarrow il}}{dt} = \frac{G_F^2}{4\pi} (\delta_{ij}\delta_{kl} + \delta_{ik}\delta_{jl})^2, \quad (4.5.10)$$

where the Mandelstam variables are $t = -2m_k(E' - E)$ and $u = -2m_k E$. The process $\nu_j\bar{\nu}_k \rightarrow \nu_i\bar{\nu}_l$ follows similarly, with the Mandelstam variables remaining the same:

$$\frac{d\sigma_{jk \rightarrow il}}{dt} = \frac{G_F^2}{4\pi} \frac{u^2}{s_k^2} (\delta_{jk}\delta_{il} + \delta_{ij}\delta_{kl})^2. \quad (4.5.11)$$

Finally, we also need to account for up-scattered relic antineutrinos, i.e. the process $\nu_j\bar{\nu}_k \rightarrow \bar{\nu}_i\nu_l$. This differs from the previous two cases as the Mandelstam variables u and t are swapped. The differential cross-section for this process is then:

$$\frac{d\sigma_{jk \rightarrow il}}{dt} = \frac{G_F^2}{4\pi} \frac{t^2}{s_k^2} (\delta_{jk}\delta_{il} + \delta_{ij}\delta_{kl})^2. \quad (4.5.12)$$

Combining these different processes gives the final differential cross-section:

$$\frac{d\sigma_{jk \rightarrow il}(E', E)}{dE} = \frac{G_F^2 m_k}{2\pi} \left((\delta_{ij}\delta_{kl} + \delta_{ik}\delta_{jl})^2 + (\delta_{jk}\delta_{il} + \delta_{ij}\delta_{kl})^2 \left(\frac{E}{E'}\right)^2 \right), \quad (4.5.13)$$

Unlike in the case of the total cross-sections, when calculating the differential cross-section in the second term on the RHS of Eq. (4.2.1), we are interested in the kinematics of the final state of the interaction. In particular, we wish to obtain the differential cross-section in terms of the energy of the outgoing i mass state (anti)neutrino. We find that the differential cross-section for neutrino pair production, taking all processes into account, is

$$\frac{d\sigma_{jk \rightarrow il}(E', E)}{dE} = \frac{G_F^2 m_k}{2\pi} \left(A_{ijkl} + B_{ijkl} \left(\frac{E}{E'}\right)^2 \right), \quad (4.5.14)$$

where we have defined

$$A_{ijkl} = (\delta_{ij}\delta_{kl} + \delta_{ik}\delta_{jl})^2, \quad (4.5.15)$$

$$B_{ijkl} = (\delta_{jk}\delta_{il} + \delta_{ij}\delta_{kl})^2. \quad (4.5.16)$$

From the kinematics of the interactions, we find that the opening angle of the neutrinos produced in these interactions is $O(10^{-6})$ radians over the energy range of interest at IceCube. Whilst this opening angle may produce substantial effects over the large distance between the point sources and Earth, the average opening angle from the production of neutrinos from pions is larger by at least three orders of magnitude. Thus, we can assume that the decrease in flux due to the angular diffusion is counteracted by the same effect occurring in adjacent patches of space.

4.5.3 Results

In Fig. 4.1, we show the test statistic as a function of the $C\nu B$ overabundance parameter η . Since the SM cross-sections are proportional to the centre-of-mass energy s , and because we assume the relic neutrinos to be at rest, the values of η

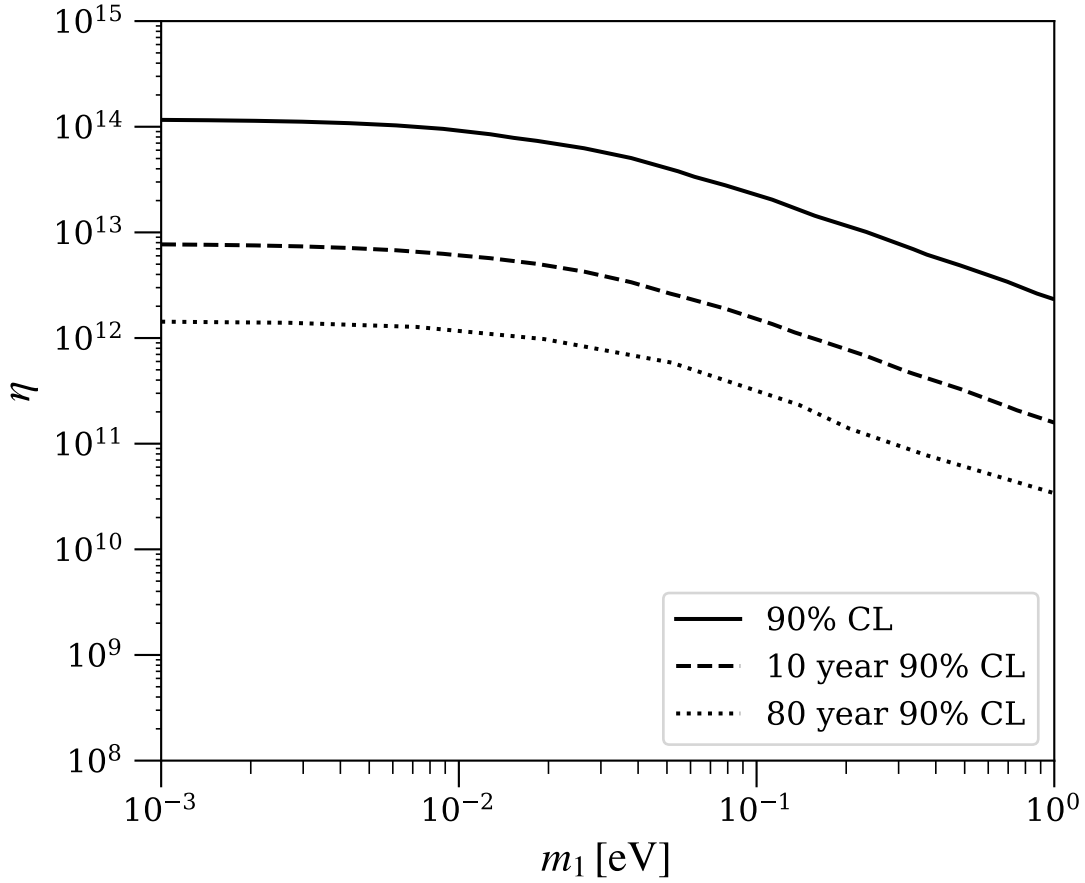


Figure 4.4: The combined 90% confidence limits from all three sources on a global relic overabundance as a function of the mass of the lightest neutrino. The solid line is the constraint using current data, and the dashed(dotted) line shows the expectation of the limit with an extra 10(80) years of data taking. We assume normal ordering and take the mass splittings from NuFIT 2022 [41].

that are probed will depend on the neutrino masses. As the absolute scale of the neutrino masses is not known, this analysis was repeated with different assumptions on the mass of the lightest neutrino, assuming normal ordering (NO) and using the mixing best-fit parameters from the NuFIT global analysis [41].

We consider three scenarios for the value of the lightest neutrino mass. First, we employ the constraints on the sum of the neutrino masses coming from cosmological measurements, i.e. $\sum_i m_i < 0.13$ eV [66], and the best-fit values of the mass splittings from neutrino oscillation experiments to obtain a mass for the lightest neutrino of $m_1 = 0.0342$ eV. Direct searches for neutrino masses, such as the one carried away by KATRIN experiment, set bound on the effective electron neutrino mass of $|U_{ei}|^2 m_i^2 < 0.8$ eV² [67], which is then translated to the value of the lightest neutrino mass of $m_1 = 0.8$ eV. Finally, we also consider a case where the lightest neutrino mass is small, but ν_1 is still non-relativistic today, i.e. $m_1 = 0.001$ eV.

The strongest constraints on η come from the larger values of m_1 , resulting from the increased centre-of-mass energy of the scattering processes, which leads to stronger interactions between the neutrinos. The limiting factor on the strength of the constraint, i.e. the plateau observed at higher values of η , is due to the limited strength of our analysis of NGC 1068 as a point source. At these values, the signal pdf of the scattered neutrino model goes to zero for all events as no signal events are predicted to be detected; this, in turn, means that the model likelihood tends towards a pure background. To push the exclusion bounds to higher confidence levels (C.L.), we would require a larger likelihood value for the PL point-source analysis of NGC 1068.

Extending this analysis to a range of values of m_1 gives the results shown in Fig. 4.4, where the 90% confidence limits are plotted for current data, and the expected sensitivity for an extra 10 and 80 years of data taking using the methods explained previously. We choose 80 years as a proxy for the IceCube Gen 2 experiment. Our constraints improve as m_1 increases due to the increase in the centre-of-mass energy. On the other hand, for small m_1 , the mass squared differences dominate in setting

the mass scale, which results in an asymptotic limit.

4.6 Scalar mediated neutrino self-interactions

In this section, we will consider new interactions between neutrinos, mediated by a new light scalar. This scenario is motivated by the potential alleviation of the H_0 and σ_8 tensions in cosmology by adding BSM neutrino self-interactions [59], [68]. These observables are sensitive to the low energy interactions between neutrinos, which affect their thermal history in the early Universe. At sufficiently low energies, these interactions have the same four-Fermi structure as low energy Z-boson interactions, but with an effective interaction strength $G_{\text{eff}} \equiv |g_{\alpha\beta}|^2 / m_\phi^2$. Here $g_{\alpha\beta}$ is the high energy coupling between flavours α and β , and m_ϕ is the mass of the new scalar mediator. The coupling between τ neutrinos is of particular interest for alleviating the H_0 and σ_8 tensions in cosmology, as the preferred regions of parameter space have been ruled out for all other lepton flavours [59]. For $g_{\tau\tau}$, the region of parameter space which results in "moderately interacting neutrinos" ($\text{MI}\nu$), is still viable. This scenario is characterised by effective interaction strengths $\log(G_{\text{eff}} \text{ MeV}^2) = -3.90^{+1.00}_{-0.93}$ [68]. Hence, this coupling will be the focus of our analysis.

There are several scenarios in which such interactions have been investigated. For example, in cosmology, these interactions can alter the number of relativistic degrees of freedom (N_{eff}) by heating the neutrino population. Constraints on N_{eff} from BBN [69] impose an upper limit on the mediator mass $m_\phi > 1.3 \text{ MeV}$ for couplings $g > 10^{-4}$. Experiments involving meson and lepton decays also probe these interactions by searching for decay modes involving neutrinos. In this work, we focus specifically on couplings involving tau neutrinos, as their detection is more challenging, leading to weaker coupling strength bounds. Current constraints from measurements of τ decay rates limit the coupling to $g_{\tau\tau}^2 < 0.1$ [70].

Treating the SM as a low-energy effective field theory, we can explore the inclusion of a higher-dimensional operator. At dimension five, the Weinberg operator [16]

can explain the smallness of the neutrino masses. At higher dimensions, additional BSM processes can emerge. For example, at dimension six, a coupling between neutrinos and a leptonic scalar with a lepton number charge of -2 can arise through the operator [71]:

$$\mathcal{L} \supset \frac{C_{ij}}{\Lambda} (\hat{H}^\dagger L_i) (\hat{H}^\dagger L_j) \phi \quad (4.6.1)$$

After the electroweak (EW) symmetry breaking, this operator contributes to the Lagrangian as

$$\mathcal{L} \supset \frac{1}{2} g_{\alpha\beta} \phi \nu_\alpha \nu_\beta, \quad (4.6.2)$$

where Greek letters denote flavor indices, ν_α are the left-handed neutrinos, and ϕ is a real scalar. While this interaction could induce flavour-changing processes, we focus exclusively on flavour-preserving interactions in this work. We follow the approach outlined in [59] to incorporate this new interaction into the cross-section calculations. We will consider the relic neutrino number density to be the same as the standard calculation, and as such can ignore the contributions from SM interactions as negligible as shown in the previous section.

The effect of these new interactions is demonstrated in Fig. 4.5, where we compare the initial power-law flux from the source to the fluxes at Earth from two sources. The first of these sources is located at a distance from Earth equal to that of NGC 1068, 14 Mpc, where we can safely ignore the effect of redshift. The second source is located at a redshift value equal to that of TXS 0506+056. By direct comparison, we can see firstly that the overall effect of the redshift is to logarithmically shift the energy of the neutrinos to lower values. However, this is not an observable effect, at least for a featureless power-law flux, since we have no fixed normalisation for the flux and so the effect can be removed by increasing the initial flux. When the scalar mediated interactions are included, new features appear in the flux which make the distinction clearer.

The two clear dips in flux occur when the centre of mass energy of the interactions between relic and astrophysical neutrinos is the same as the mass of the mediating scalar particle, producing a resonance in the cross-section. There are in fact three dips, coinciding with the three masses of the neutrinos, which are separated according to the mass differences which can be found from the experimentally measured oscillation parameters. The smallness of the 1-2 mass difference leads to the two dips being too close to distinguish successfully. The width of the dips is, at tree level, proportional to the decay-rate of the scalar mediator [59]

$$\Gamma \sim m_\phi g_{\tau\tau}^2. \quad (4.6.3)$$

Comparing Fig. 4.5b to Fig. 4.5d, we can see how increasing the coupling widens the "necks" of the dips.

We can also see the effect of redshift in these plots. On the one hand, the larger distance travelled by the neutrinos leads to more significant changes in the flux, due simply to the increase in the numbers of interactions that will occur. However the redshift also shifts to flux to lower energy values, thereby "filling in" the dip with the fluxes from higher energies. This is demonstrated in Fig. 4.6, where the normalised flux is compared between three sources with different redshifts.

4.6.1 Results

The results of our analysis of NSI are presented in Fig. 4.8. We compare our bounds to those from BBN, Z to invisible decays, and High Energy Starting Events (HESE) at IceCube which originate from the diffuse astrophysical flux [59]. The HESE dataset contains all events with an interaction vertex fully contained by the fiducial volume of the detector [72]. As such, it contains a larger superset of the data considered in our analysis, since we look only at events which can be reconstructed as tracks. We find that the combined bound from all three sources considered in this work is generally outperformed in the relevant parameter space by the diffuse source

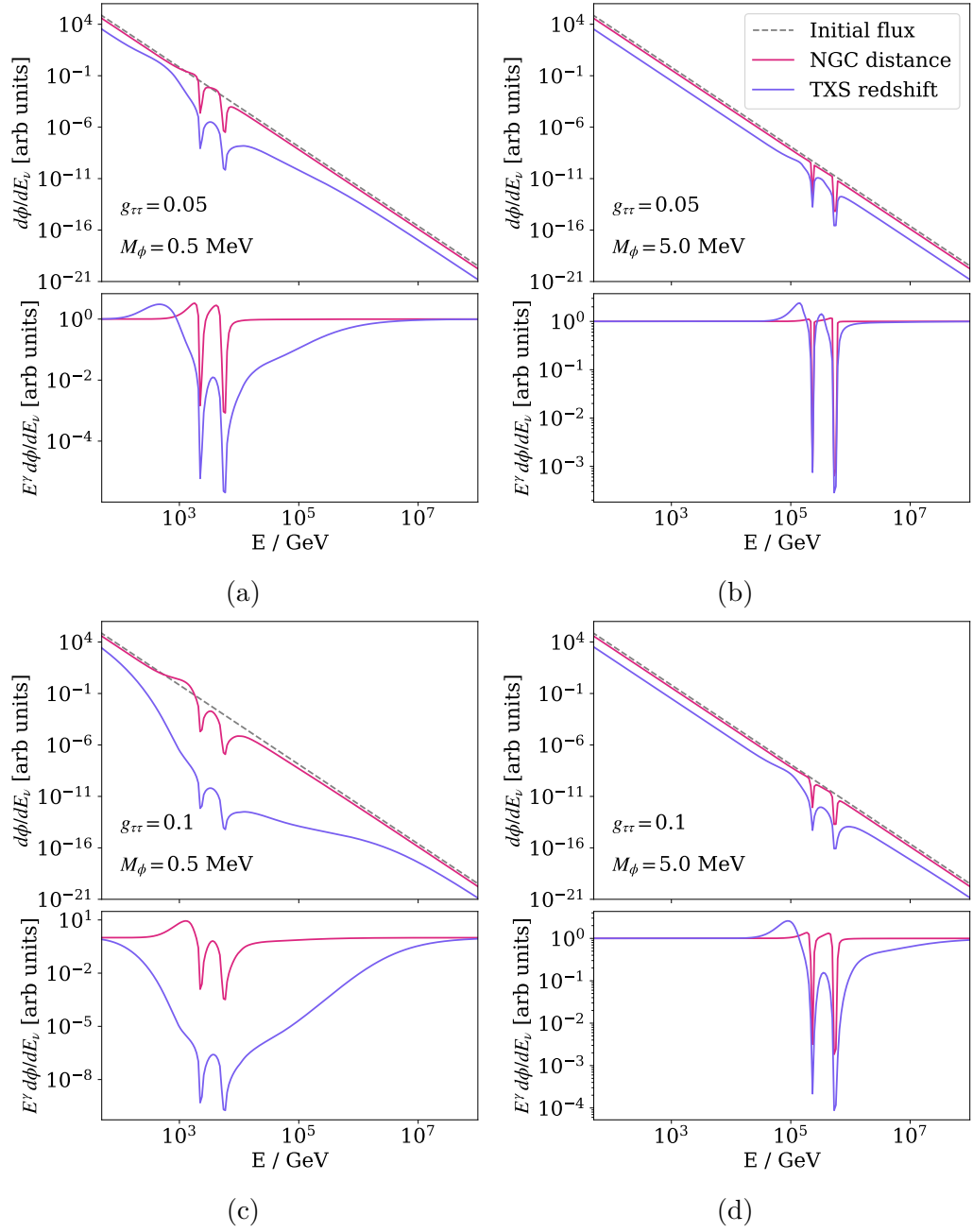


Figure 4.5: Effects of NSI on the neutrino flux propagating through the $C\nu B$. We take an initial power-law flux with spectral index $\gamma = 3.86$, which matches that of PKS. The final flux at Earth is calculated for a source at the same distance as NGC 1068 - 14 Mpc - and for a source at the same redshift as TXS 0506+056 - $z = 0.45$. This highlights the difference in final flux caused by both the increased propagation distance and the redshift from the expansion of the Universe. The value of the coupling between tau-flavoured neutrinos and the scalar particle, $g_{\tau\tau}$, as well as the mass of the scalar particle, M_ϕ , are varied between figures (a)-(d) to demonstrate their effect on the final fluxes. Flux values are given in arbitrary units as the normalisation of the flux is a priori unknown.

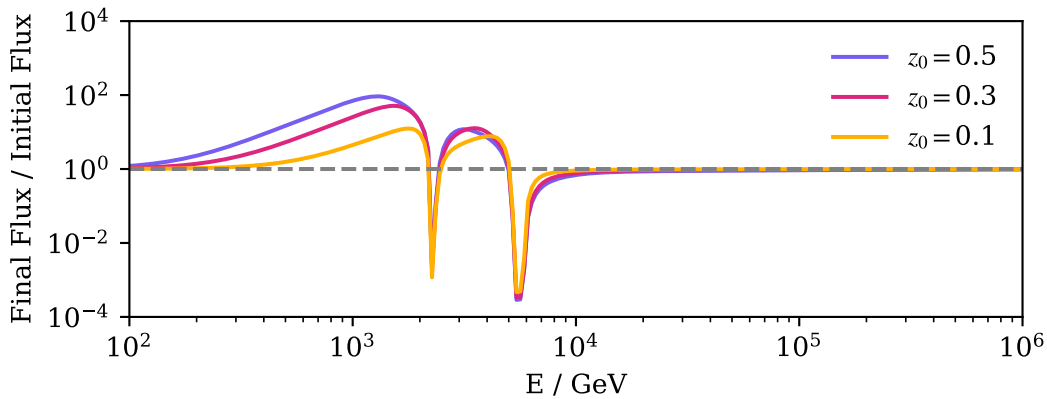


Figure 4.6: Ratio of the final to initial muon neutrino fluxes from three toy sources at redshifts $z_0 \in \{0.5, 0.3, 0.1\}$. The lowering of the flux energy, thereby preserving the bump in flux at lower energies, can be clearly seen. To produce these fluxes an initial power-law flux was used with spectral index $\gamma = 2.7$. The scalar coupling was chosen to be $g_{\tau\tau} = 0.02$ and the scalar mediator mass was $m_\phi = 0.5$ MeV. Finally, the lightest neutrino mass m_1 was given a value such that the cosmological bound on the sum of the neutrino masses was saturated.

analysis, which we attribute to the smaller number of source events for point-sources. However, the bounds are comparable, and point sources provide better constraints for mediator masses, m_ϕ , below 1 MeV, though BBN already constrains this. These bounds are both complementary since calculating the flux of diffuse sources in the NSI scenario requires assumptions about the z -dependence of neutrino production in the early Universe [59], which is not the case for point sources where the redshift is known to within some uncertainty.

We have also estimated the future sensitivity for 80 years of extra data, as a proxy for 10 years of IceCube Gen-2 (dashed line in Fig. 4.8). The increase in observed events expected at IceCube Gen-2 will be able to push the exclusion region to cover much of the $MI\nu$ solution, which will have important consequences for both neutrino physics and cosmology. However the improvement in sensitivity is not uniform across the values of the mass. This can be understood by considering the limiting factors of the sensitivity of the analysis. For higher values of mass, the sensitivity is limited by the flux of neutrinos at energies which are high enough to coincide with the dips in

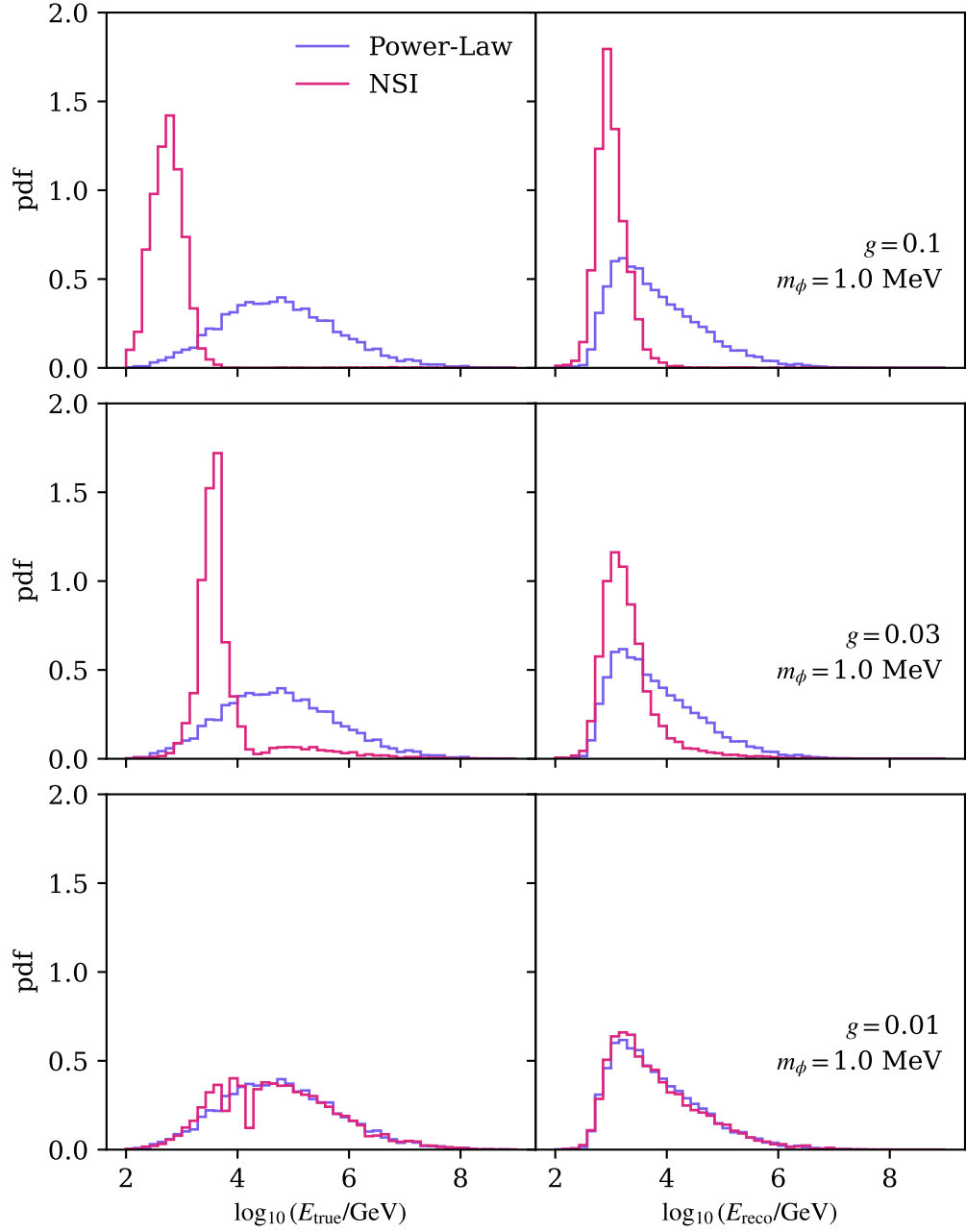


Figure 4.7: Pdfs of logarithms of the true neutrino energy E_{true} (left panels), and the reconstructed muon energy E_{reco} (right panels), for varying values of the coupling $g_{\tau\tau}$. For each set of NSI parameters, the full analysis was performed assuming the source was TXS 0506+056, and the best fit initial power law parameters were used. The pdfs were constructed from event samples created using SkyLLH.

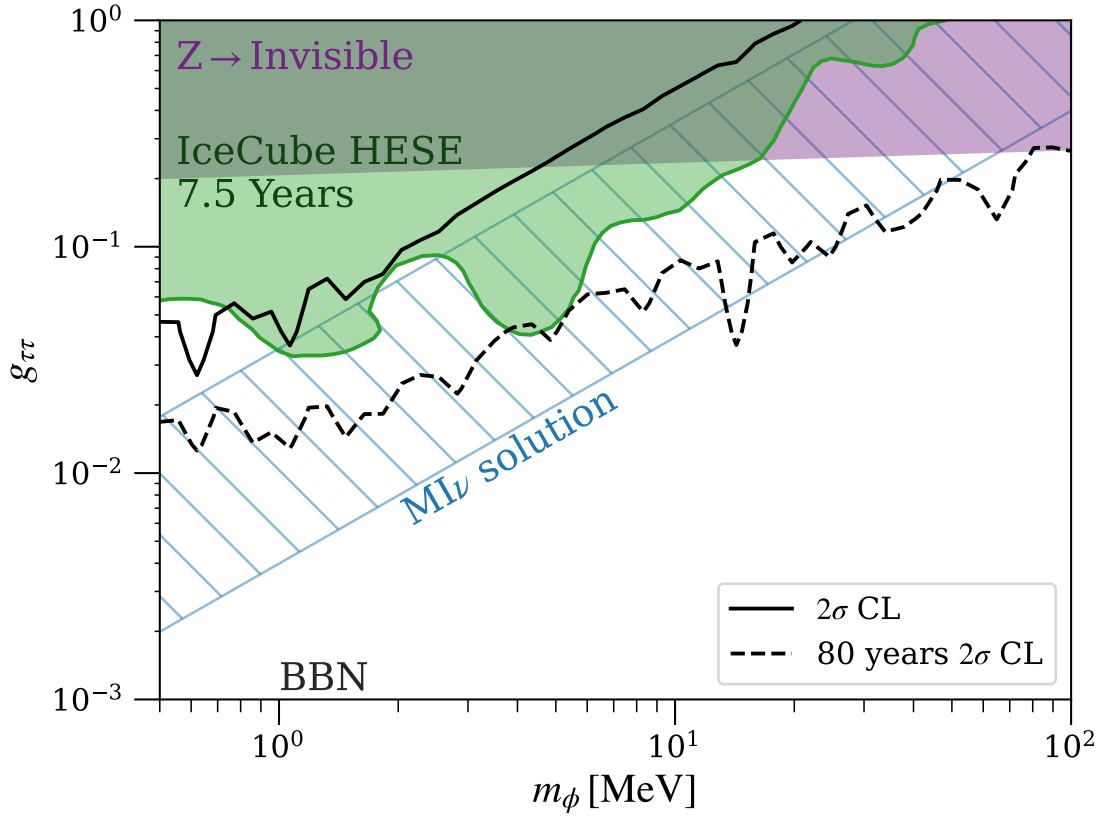


Figure 4.8: **Scalar mediated neutrino self-interaction.** The 2σ exclusion region determined by IceCube is shown based on astrophysical sources NGC 1068, TXS 0506+056 and PKS 1424+240, and their combined result (black solid line). To produce these, we assumed normal ordering of the neutrino masses and took $\sum_i m_i = 0.1\text{eV}$ with mass splittings from [41]. Additionally, we include the projected exclusion region for an additional 80 years of operation (black dash line), equivalent to 10 years of data collection with IceCube-Gen2. We compare our results to those from [59], which includes exclusion regions from BBN (grey), Z to invisibles decay (purple), and IceCube HESE (green).

the flux. On the other hand, as $g_{\tau\tau}$ gets smaller the widths of the dips are reduced, as can be seen in Fig. 4.5. If the energy pdf is broader than the width of the dip, it is not possible to resolve the effect of the dip at the statistical level, i.e. the analysis is systematics limited. This means that there will be some value of $g_{\tau\tau}$ at which the sensitivity of the analysis saturates and additional data provides negligible benefits. We can see this happening in Fig. 4.8, where the additional 80 years of data lowers the contour at higher masses more than at lower masses, even though the statistics relevant to the latter regime will increase much more than the former. Looking at Fig. 4.7 we can see how, as $g_{\tau\tau}$ decreases, the pdf of the reconstructed muon energy for NSIs becomes less distinguishable from the pdf for the power-law flux; this is the case even though the pdf of the true neutrino energy retains features of the dip. This limit can only be overcome by improved analysis and reconstruction techniques, such as those used in [56].

4.7 Conclusion

Point sources of neutrinos offer a unique perspective into neutrino physics, both within and beyond the Standard Model. It is also possible that additional BSM scenarios beyond those discussed in this work could be constrained using a similar analysis. We performed a log-likelihood analysis on neutrino decays arising from a coupling to a massless scalar. However, we found that current public data cannot constrain this scenario to a statistically significant degree as $|TS| < 0.2$ for all coupling values.

As more data is collected, and improvements are made to analysis and reconstruction techniques, these sources will be able to push our understanding of the neutrino to new limits. They are particularly complimentary to diffuse neutrinos sources, as the distance of propagation can be found using astronomical observations of their source galaxy. This allows for a reduction in the assumptions made in any analysis, which will provide more robust results. Furthermore, the addition of new data may make

possible the identification of additional point-source candidates beyond the three discussed in this analysis, which will potentially allow for further improvement on the results presented here. This will almost certainly be the case with the future IceCube Gen2 experiment, which will increase the rate of data taking by almost an order of magnitude.

Chapter 5

Summary

In this thesis, we have investigated how two different sources of neutrinos, both produced in astrophysical processes, can be used as experimental windows into the fundamental nature and properties of neutrinos. The variety of these fluxes allows for a wide range of potential realities to be scrutinised. The phenomena of neutrino oscillations forces us to consider models of physics beyond the Standard Model as we know it today. As such, neutrinos offer a pathway of discovery if we can find ways to uncover their secrets.

In Chapter 3, we looked at the pseudo-Dirac scenario for neutrino masses. We found that Solar neutrinos offer fertile ground for exploring the oscillations that occur in this scenario. This was due to their low energies, and the large propagation distance between the Sun and Earth. In particular the JUNO experiment, which aims to begin data taking in the very near future, could provide large improvements in the sensitivity to small values of δm^2 . If it is possible to control the large ^{14}C background, the sensitivity may even compete with the future DARWIN (now XLZD) xenon detector.

On the other end of the energy scale, the possibility of harnessing high energy neutrinos for new physics searches was detailed in Chapter 4. Point sources at IceCube offer unique fluxes of neutrinos with energies of 100 GeV and beyond, from galaxies with well constrained distances or redshifts. This offers complementarity

to the diffuse fluxes at IceCube which have no known origin. We focussed our efforts on two scenarios in particular, using public experimental data to perform our analysis. The first of these was to search for deviations in the density of relic neutrinos, however we found that the energies of the neutrino fluxes were too low to probe this well. The second scenario investigated was that of additional interactions between neutrinos, mediated by a light scalar particle. Our point source analysis was able to produce similar constraints to those from diffuse fluxes, even though the mean number of signal events was orders of magnitude smaller. Improvements on these constraints will come from two directions. Firstly, advancements in analysis and reconstruction techniques will be able to strengthen the discriminative power of point source analyses. These improvements have already been developed by the IceCube collaboration for their point source searches, and hopefully will become public in the near future. The second direction of progress will be the construction of future high energy neutrino observatories, such as KM3NeT and in particular IceCube Gen2. These next generation experiments will be able to drastically increase the number of neutrinos detected from point sources. We showed that such an increase in data would lead to large improvements on the sensitivity to new interactions.

To conclude, we have covered neutrino fluxes that spread over gargantuan scales in energy. In particular, the neutrinos observed at IceCube have energies beyond those achievable even for protons at the LHC. Combined with the large distances over which all astrophysical neutrino fluxes must travel before reaching Earth, they allow us to investigate their behaviour under conditions that could never be replicated by terrestrial experiments. They are thus a vital tool in our ongoing journey to explore what may lay beyond the horizon of our understanding of the Universe. When the next generation of neutrino experiments and observatories come online, our understanding of both the neutrino and the Universe will be pushed to new heights.

Bibliography

- [1] H. K. Dreiner, H. E. Haber and S. P. Martin, “Two-component spinor techniques and Feynman rules for quantum field theory and supersymmetry,” *Physics Reports*, vol. 494, no. 1-2, pp. 1–196, Sep. 2010, ISSN: 03701573. DOI: 10.1016/j.physrep.2010.05.002. arXiv: 0812.1594 [hep-ph].
- [2] L. Infeld and B. L. van der Waerden, “THE WAVE EQUATION OF THE ELECTRON IN THE GENERAL RELATIVITY THEORY,” *Sitzungsber. Preuss. Akad. Wiss. Berlin (Math. Phys.)*, vol. 1933, pp. 380–401, 1933.
- [3] M. Srednicki, *Quantum field theory*. Cambridge University Press, Jan. 2007, ISBN: 978-0-521-86449-7, 978-0-511-26720-8. DOI: 10.1017/CB09780511813917.
- [4] S. Navas *et al.*, “Review of particle physics,” *Phys. Rev. D*, vol. 110, no. 3, p. 030 001, 2024. DOI: 10.1103/PhysRevD.110.030001.
- [5] M. E. Peskin and D. V. Schroeder, *An Introduction to quantum field theory*. Reading, USA: Addison-Wesley, 1995, ISBN: 978-0-201-50397-5, 978-0-429-50355-9, 978-0-429-49417-8. DOI: 10.1201/9780429503559.
- [6] P. Ramond, *Journeys beyond the standard model*. 1999, vol. 101, ISBN: 978-0-8133-4131-6, 978-0-7382-0116-0.
- [7] R. N. Mohapatra and P. B. Pal, *Massive Neutrinos in Physics and Astrophysics (Third Edition)*. 2004. DOI: 10.1142/5024.

- [8] T. Takagi, “On an Algebraic Problem Related to an Analytic Theorem of Carathéodory and Fejér and on an Allied Theorem of Landau,” *Japanese journal of mathematics :transactions and abstracts*, vol. 1, pp. 83–93, 1924. DOI: 10.4099/jjm1924.1.0_83.
- [9] S. M. Bilenky and S. T. Petcov, “Massive neutrinos and neutrino oscillations,” *Reviews of Modern Physics*, vol. 59, no. 3, pp. 671–754, Jul. 1987, ISSN: 0034-6861. DOI: 10.1103/RevModPhys.59.671. (visited on 15/03/2025).
- [10] L. Wolfenstein, “Different Varieties of Massive Dirac Neutrinos,” *Nucl. Phys. B*, vol. 186, pp. 147–152, 1981. DOI: 10.1016/0550-3213(81)90096-1.
- [11] S. T. Petcov, “On Pseudodirac Neutrinos, Neutrino Oscillations and Neutrinoless Double beta Decay,” *Phys. Lett. B*, vol. 110, pp. 245–249, 1982. DOI: 10.1016/0370-2693(82)91246-1.
- [12] S. M. Bilenky and B. Pontecorvo, “Neutrino Oscillations With Large Oscillation Length in Spite of Large (Majorana) Neutrino Masses?” *Sov. J. Nucl. Phys.*, vol. 38, p. 248, 1983.
- [13] R. Foot and R. R. Volkas, “Neutrino physics and the mirror world: How exact parity symmetry explains the solar neutrino deficit, the atmospheric neutrino anomaly and the LSND experiment,” *Phys. Rev. D*, vol. 52, pp. 6595–6606, 1995. DOI: 10.1103/PhysRevD.52.6595. arXiv: hep-ph/9505359.
- [14] D. Chang and O. C. W. Kong, “Pseudo-Dirac neutrinos,” *Phys. Lett. B*, vol. 477, pp. 416–423, 2000. DOI: 10.1016/S0370-2693(00)00228-8. arXiv: hep-ph/9912268.
- [15] A. de Gouvea, W.-C. Huang and J. Jenkins, “Pseudo-Dirac Neutrinos in the New Standard Model,” *Phys. Rev. D*, vol. 80, p. 073007, 2009. DOI: 10.1103/PhysRevD.80.073007. arXiv: 0906.1611 [hep-ph].
- [16] S. Weinberg, “Baryon and Lepton Nonconserving Processes,” *Phys. Rev. Lett.*, vol. 43, pp. 1566–1570, 1979. DOI: 10.1103/PhysRevLett.43.1566.

- [17] C. Giunti and C. W. Kim, *Fundamentals of Neutrino Physics and Astrophysics*. 2007, ISBN: 978-0-19-850871-7. DOI: 10.1093/acprof:oso/9780198508717.001.0001.
- [18] J. J. Gómez-Cadenas, J. Martín-Albo, J. Menéndez, M. Mezzetto, F. Monrabal and M. Sorel, “The search for neutrinoless double-beta decay,” *La Rivista del Nuovo Cimento*, vol. 46, no. 10, pp. 619–692, 1st Oct. 2023, ISSN: 1826-9850. DOI: 10.1007/s40766-023-00049-2.
- [19] A. Gando *et al.*, “Search for Majorana Neutrinos near the Inverted Mass Hierarchy Region with KamLAND-Zen,” *Phys. Rev. Lett.*, vol. 117, no. 8, p. 082503, 2016, [Addendum: *Phys.Rev.Lett.* 117, 109903 (2016)]. DOI: 10.1103/PhysRevLett.117.082503. arXiv: 1605.02889 [hep-ex].
- [20] CUORE Collaboration, D. Q. Adams, C. Alduino *et al.*, “Improved Limit on Neutrinoless Double-Beta Decay in ^{130}Te with CUORE,” *Physical Review Letters*, vol. 124, no. 12, p. 122501, 26th Mar. 2020. DOI: 10.1103/PhysRevLett.124.122501.
- [21] EXO-200 Collaboration, G. Anton, I. Badhrees *et al.*, “Search for Neutrinoless Double- β Decay with the Complete EXO-200 Dataset,” *Physical Review Letters*, vol. 123, no. 16, p. 161802, 18th Oct. 2019. DOI: 10.1103/PhysRevLett.123.161802.
- [22] GERDA Collaboration, M. Agostini, G. R. Araujo *et al.*, “Final Results of GERDA on the Search for Neutrinoless Double- β Decay,” *Physical Review Letters*, vol. 125, no. 25, p. 252502, 17th Dec. 2020. DOI: 10.1103/PhysRevLett.125.252502.
- [23] J. Schechter and J. W. F. Valle, “Neutrinoless Double beta Decay in SU(2) x U(1) Theories,” *Phys. Rev. D*, vol. 25, p. 2951, 1982. DOI: 10.1103/PhysRevD.25.2951.

- [24] Y. Fukuda *et al.*, “Evidence for oscillation of atmospheric neutrinos,” *Phys. Rev. Lett.*, vol. 81, pp. 1562–1567, 1998. DOI: 10.1103/PhysRevLett.81.1562. arXiv: hep-ex/9807003.
- [25] M. Beuthe, “Oscillations of neutrinos and mesons in quantum field theory,” *Phys. Rept.*, vol. 375, pp. 105–218, 2003. DOI: 10.1016/S0370-1573(02)00538-0. arXiv: hep-ph/0109119.
- [26] M. Fukugita and T. Yanagida, *Physics of neutrinos and applications to astrophysics* (Theoretical and Mathematical Physics). Berlin, Germany: Springer-Verlag, 2003, ISBN: 978-3-662-05119-1, 978-3-540-43800-7, 978-3-642-07851-4. DOI: 10.1007/978-3-662-05119-1.
- [27] J. Aalbers *et al.*, “Solar neutrino detection sensitivity in darwin via electron scattering,” *The European Physical Journal C*, vol. 80, no. 1133, 2020. DOI: 10.1140/epjc/s10052-020-08602-7.
- [28] E. K. Akhmedov, R. Johansson, M. Lindner, T. Ohlsson and T. Schwetz, “Series expansions for three-flavor neutrino oscillation probabilities in matter,” *Journal of High Energy Physics*, vol. 2004, no. 04, p. 078, May 2004, ISSN: 1126-6708. DOI: 10.1088/1126-6708/2004/04/078.
- [29] F. An *et al.*, “Neutrino Physics with JUNO,” *J. Phys. G*, vol. 43, no. 3, p. 030401, 2016. DOI: 10.1088/0954-3899/43/3/030401. arXiv: 1507.05613 [physics.ins-det].
- [30] I. Lopes and S. Turck-Chièze, “Solar neutrino physics oscillations: Sensitivity to the electronic density in the sun’s core,” *The Astrophysical Journal*, vol. 765, no. 1, p. 14, Feb. 2013. DOI: 10.1088/0004-637X/765/1/14.
- [31] A. Abusleme *et al.*, “Radioactivity control strategy for the JUNO detector,” *JHEP*, vol. 11, p. 102, 2021. DOI: 10.1007/JHEP11(2021)102. arXiv: 2107.03669 [physics.ins-det].
- [32] A. Abusleme *et al.*, “JUNO sensitivity to ^7Be , *pep*, and CNO solar neutrinos,” Mar. 2023. arXiv: 2303.03910 [hep-ex].

- [33] N. Aghanim *et al.*, “Planck 2018 results. VI. Cosmological parameters,” *Astron. Astrophys.*, vol. 641, A6, 2020, [Erratum: *Astron. Astrophys.* 652, C4 (2021)]. DOI: 10.1051/0004-6361/201833910. arXiv: 1807.06209 [astro-ph.CO].
- [34] B. Bamieh. “A Tutorial on Matrix Perturbation Theory (using compact matrix notation).” arXiv: 2002.05001 [math]. (24th Apr. 2022), pre-published.
- [35] M. Kobayashi and C. S. Lim, “Pseudo-Dirac Scenario for Neutrino Oscillations,” *Physical Review D*, vol. 64, no. 1, p. 013003, 21st May 2001, ISSN: 0556-2821, 1089-4918. DOI: 10.1103/PhysRevD.64.013003. arXiv: hep-ph/0012266.
- [36] A. de Gouvêa, E. McGinness, I. Martinez-Soler and Y. F. Perez-Gonzalez, “pp solar neutrinos at DARWIN,” *Phys. Rev. D*, vol. 106, no. 9, p. 096017, 2022. DOI: 10.1103/PhysRevD.106.096017. arXiv: 2111.02421 [hep-ph].
- [37] S. J. Parke, “Nonadiabatic Level Crossing in Resonant Neutrino Oscillations,” *Phys. Rev. Lett.*, vol. 57, S. C. Loken, Ed., pp. 1275–1278, 1986. DOI: 10.1103/PhysRevLett.57.1275. arXiv: 2212.06978 [hep-ph].
- [38] A. de Gouvea, A. Friedland and H. Murayama, “Seasonal variations of the Be-7 solar neutrino flux,” *Phys. Rev. D*, vol. 60, p. 093011, 1999. DOI: 10.1103/PhysRevD.60.093011. arXiv: hep-ph/9904399.
- [39] A. Friedland, “MSW effects in vacuum oscillations,” *Phys. Rev. Lett.*, vol. 85, pp. 936–939, 2000. DOI: 10.1103/PhysRevLett.85.936. arXiv: hep-ph/0002063.
- [40] N. Vinyoles, A. M. Serenelli, F. L. Villante *et al.*, “A new generation of standard solar models,” *The Astrophysical Journal*, vol. 835, no. 2, p. 202, 2017. DOI: 10.3847/1538-4357/835/2/202.
- [41] I. Esteban, M. Gonzalez-Garcia, M. Maltoni, T. Schwetz and A. Zhou, “The fate of hints: Updated global analysis of three-flavor neutrino oscillations,” *Journal of High Energy Physics*, vol. 2020, no. 9, p. 178, 28th Sep. 2020, ISSN: 1029-8479. DOI: 10.1007/JHEP09(2020)178.

- [42] H. Murayama, “Impact of neutrino oscillation measurements on theory,” *AIP Conf. Proc.*, vol. 721, no. 1, A. Para, Ed., pp. 122–129, 2004. DOI: 10.1063/1.1818385. arXiv: hep-ph/0312008.
- [43] G. L. Fogli, E. Lisi, A. Marrone and A. Palazzo, “Global analysis of three-flavor neutrino masses and mixings,” *Prog. Part. Nucl. Phys.*, vol. 57, pp. 742–795, 2006. DOI: 10.1016/j.pnpnp.2005.08.002. arXiv: hep-ph/0506083.
- [44] J. P. Cravens *et al.*, “Solar neutrino measurements in Super-Kamiokande-II,” *Phys. Rev. D*, vol. 78, p. 032002, 2008. DOI: 10.1103/PhysRevD.78.032002. arXiv: 0803.4312 [hep-ex].
- [45] B. Aharmim *et al.*, “An Independent Measurement of the Total Active B-8 Solar Neutrino Flux Using an Array of He-3 Proportional Counters at the Sudbury Neutrino Observatory,” *Phys. Rev. Lett.*, vol. 101, p. 111301, 2008. DOI: 10.1103/PhysRevLett.101.111301. arXiv: 0806.0989 [nucl-ex].
- [46] M. B. Smy, “Solar neutrino precision measurements using all 1496 days of Super-Kamiokande I data,” *Nucl. Phys. B Proc. Suppl.*, vol. 118, F. von Feilitzsch and N. Schmitz, Eds., pp. 25–32, 2003. DOI: 10.1016/S0920-5632(03)01300-8. arXiv: hep-ex/0208004.
- [47] B. T. Cleveland, T. Daily, R. Davis Jr. *et al.*, “Measurement of the solar electron neutrino flux with the Homestake chlorine detector,” *Astrophys. J.*, vol. 496, pp. 505–526, 1998. DOI: 10.1086/305343.
- [48] S. Ansarifard and Y. Farzan, “Revisiting pseudo-dirac neutrino scenario after recent solar neutrino data,” 2023. arXiv: 2211.09105 [hep-ph].
- [49] F. Capozzi, S. W. Li, G. Zhu and J. F. Beacom, “DUNE as the Next-Generation Solar Neutrino Experiment,” *Phys. Rev. Lett.*, vol. 123, no. 13, p. 131803, 2019. DOI: 10.1103/PhysRevLett.123.131803. arXiv: 1808.08232 [hep-ph].
- [50] J. Bian *et al.*, “Hyper-Kamiokande Experiment: A Snowmass White Paper,” in *Snowmass 2021*, Mar. 2022. arXiv: 2203.02029 [hep-ex].

- [51] M. G. Aartsen *et al.*, “Evidence for High-Energy Extraterrestrial Neutrinos at the IceCube Detector,” *Science*, vol. 342, p. 1242856, 2013. DOI: 10.1126/science.1242856. arXiv: 1311.5238 [astro-ph.HE].
- [52] F. W. Stecker, C. Done, M. H. Salamon and P. Sommers, “High-energy neutrinos from active galactic nuclei,” *Physical Review Letters*, vol. 66, no. 21, pp. 2697–2700, 27th May 1991. DOI: 10.1103/PhysRevLett.66.2697.
- [53] E. Vitagliano, I. Tamborra and G. Raffelt, “Grand unified neutrino spectrum at Earth: Sources and spectral components,” *Reviews of Modern Physics*, vol. 92, no. 4, p. 045006, 9th Dec. 2020. DOI: 10.1103/RevModPhys.92.045006.
- [54] A. Achterberg, M. Ackermann, J. Adams *et al.*, “First year performance of the IceCube neutrino telescope,” *Astroparticle Physics*, vol. 26, no. 3, pp. 155–173, 1st Oct. 2006, ISSN: 0927-6505. DOI: 10.1016/j.astropartphys.2006.06.007.
- [55] M. G. Aartsen, M. Ackermann, J. Adams *et al.*, “Time-Integrated Neutrino Source Searches with 10 Years of IceCube Data,” *Physical Review Letters*, vol. 124, no. 5, p. 051103, 6th Feb. 2020. DOI: 10.1103/PhysRevLett.124.051103.
- [56] ICECUBE COLLABORATION, R. Abbasi, M. Ackermann *et al.*, “Evidence for neutrino emission from the nearby active galaxy NGC 1068,” *Science*, vol. 378, no. 6619, pp. 538–543, 4th Nov. 2022. DOI: 10.1126/science.abg3395.
- [57] A. J. Long, C. Lunardini and E. Sabancilar, “Detecting non-relativistic cosmic neutrinos by capture on tritium: Phenomenology and physics potential,” *Journal of Cosmology and Astroparticle Physics*, vol. 2014, no. 08, p. 038, Aug. 2014, ISSN: 1475-7516. DOI: 10.1088/1475-7516/2014/08/038.
- [58] S.-F. Ge and P. Pasquini, “Parity violation and chiral oscillation of cosmological relic neutrinos,” *Physics Letters B*, vol. 811, p. 135961, 10th Dec. 2020, ISSN: 0370-2693. DOI: 10.1016/j.physletb.2020.135961.

- [59] I. Esteban, S. Pandey, V. Brdar and J. F. Beacom, “Probing secret interactions of astrophysical neutrinos in the high-statistics era,” *Phys. Rev. D*, vol. 104, p. 123014, 12 Dec. 2021. DOI: 10.1103/PhysRevD.104.123014. [Online]. Available: <https://link.aps.org/doi/10.1103/PhysRevD.104.123014>.
- [60] P. Bhattacharjee and G. Sigl, “Origin and propagation of extremely high-energy cosmic rays,” *Phys. Rept.*, vol. 327, pp. 109–247, 2000. DOI: 10.1016/S0370-1573(99)00101-5. arXiv: astro-ph/9811011.
- [61] S. Lee, “On the propagation of extragalactic high-energy cosmic and gamma-rays,” *Phys. Rev. D*, vol. 58, p. 043004, 1998. DOI: 10.1103/PhysRevD.58.043004. arXiv: astro-ph/9604098.
- [62] M. Wolf, “SkyLLH - A generalized Python-based tool for log-likelihood analyses in multi-messenger astronomy,” *PoS*, vol. ICRC2019, p. 1035, 2021. DOI: 10.22323/1.358.1035. arXiv: 1908.05181 [astro-ph.IM].
- [63] C. Bellenghi *et al.*, “Extending SkyLLH software for neutrino point source analyses with 10 years of IceCube public data,” *PoS*, vol. ICRC2023, p. 1061, 2023. DOI: 10.22323/1.444.1061. arXiv: 2308.12733 [astro-ph.HE].
- [64] R. Abbasi *et al.*, “The SkyLLH framework for IceCube point-source search,” *PoS*, vol. ICRC2021, p. 1073, 2021. DOI: 10.22323/1.395.1073. arXiv: 2107.08934 [astro-ph.IM].
- [65] IceCube Collaboration, *Icecube data for neutrino point-source searches years 2008-2018*, 2021. DOI: 10.21234/CPKQ-K003. [Online]. Available: <https://arxiv.org/abs/2101.09836>.
- [66] DES Collaboration, T. M. C. Abbott, M. Aguena *et al.*, “Dark Energy Survey Year 3 results: Cosmological constraints from galaxy clustering and weak lensing,” *Physical Review D*, vol. 105, no. 2, p. 023520, 13th Jan. 2022. DOI: 10.1103/PhysRevD.105.023520.

- [67] M. Aker, A. Beglarian, J. Behrens *et al.*, “Direct neutrino-mass measurement with sub-electronvolt sensitivity,” *Nature Physics*, vol. 18, no. 2, pp. 160–166, Feb. 2022, ISSN: 1745-2481. DOI: 10.1038/s41567-021-01463-1.
- [68] C. D. Kreisch, F.-Y. Cyr-Racine and O. Doré, “Neutrino puzzle: Anomalies, interactions, and cosmological tensions,” *Phys. Rev. D*, vol. 101, no. 12, p. 123 505, 2020. DOI: 10.1103/PhysRevD.101.123505. arXiv: 1902.00534 [astro-ph.CO].
- [69] N. Blinov, K. J. Kelly, G. Z. Krnjaic and S. D. McDermott, “Constraining the Self-Interacting Neutrino Interpretation of the Hubble Tension,” *Phys. Rev. Lett.*, vol. 123, no. 19, p. 191 102, 2019. DOI: 10.1103/PhysRevLett.123.191102. arXiv: 1905.02727 [astro-ph.CO].
- [70] A. P. Lessa and O. L. G. Peres, “Revising limits on neutrino-Majoron couplings,” *Phys. Rev. D*, vol. 75, p. 094 001, 2007. DOI: 10.1103/PhysRevD.75.094001. arXiv: hep-ph/0701068.
- [71] A. de Gouvêa, P. S. B. Dev, B. Dutta, T. Ghosh, T. Han and Y. Zhang, “Leptonic Scalars at the LHC,” *JHEP*, vol. 07, p. 142, 2020. DOI: 10.1007/JHEP07(2020)142. arXiv: 1910.01132 [hep-ph].
- [72] IceCube Collaboration, R. Abbasi, M. Ackermann *et al.*, “IceCube high-energy starting event sample: Description and flux characterization with 7.5 years of data,” *Physical Review D*, vol. 104, no. 2, p. 022 002, 8th Jul. 2021. DOI: 10.1103/PhysRevD.104.022002.